Available online at www.sciencedirect.com
SCIENCE DIRECT®
Progress in Particle and Nuclear Physics
52 (2004) 1–83
Progress in Particle and Nuclear Physics
www.elsevier.com/locate/ppnp

Review

The 47 years of muon $g-2$

F.J.M. Farley[a,*], Y.K. Semertzidis[b]

[a] *Yale University, New Haven, CT 06520, USA*
[b] *Brookhaven National Laboratory, Upton, NY 11973, USA*

Received 30 October 2003

Abstract

After a brief introduction to the theory of the muon anomalous moment $a \equiv (g-2)/2$, all the experimental measurements of this quantity are reviewed in some detail. This includes the CERN cyclotron experiment, the first muon storage rings at CERN, the Berkeley experiment, the invention of the "magic energy" and the latest measurement with the third muon storage ring at Brookhaven. The current comparison with theory is discussed.

Keywords: Muon; Magnetic moment; $g-2$

Contents

* Corresponding address: 8 Chemin de Saint Pierre, 06620 le Bar sur Loup, France.

0146-6410/$ - see front matter © 2003 Elsevier B.V. All rights reserved.
doi:10.1016/j.ppnp.2003.09.004

1. Introduction

The gyromagnetic ratio g is the ratio of the magnetic moment of a system to the value obtained by multiplying its angular momentum by the Larmor ratio $(e/2mc)$. For an orbiting electron $g = 1$. When Goudschmit and Uhlenbeck [1] postulated the spinning electron with angular momentum $(h/4\pi)$ to explain the anomalous Zeeman effect, it was surprising that its magnetic moment, one Bohr magneton, was twice the expected value: the

gyromagnetic ratio for the electron was apparently 2. Later Dirac [2] found that this value came out as a natural consequence of his relativistic equation for the electron. Kramers [3] obtained the same result by a purely classical argument; he developed Lorentz covariant equations for the spin motion in a moving system: comparing with the expression for acceleration led to $g = 2$.

Another surprise was to come. Experimentally [4] the magnetic moment of the electron was in fact slightly larger, so $g = 2(1 + a)$ with a being defined as the "anomalous moment". In its turn the anomaly was understood [5] as arising from the quantum fluctuations of the electromagnetic field around the particle. The calculation of this quantity [6], in parallel with measurements of increasing accuracy, has been the main stimulus to the development of quantum electrodynamics. Astonishingly, the electron theory and experiment agree for this pure quantum effect to 0.02 ppm (parts per million) in a, the limit being set by our independent knowledge of the fine structure constant α.

For the muon, the $(g - 2)$ value has played a central role in establishing that it behaves like a heavy electron and obeys the rules of quantum electrodynamics (QED). The experimental value of $(g - 2)$ has been determined by three progressively more precise measurements at CERN and a recent experiment at Brookhaven, now achieving a precision of 0.7 ppm in the anomaly $a \equiv (g - 2)/2$. In parallel, the theoretical value for $(g - 2)$ has improved steadily as higher order QED contributions have been evaluated, and as knowledge of the virtual hadronic contributions to $(g - 2)$ has been refined.

The story starts in 1956 when the magnetic anomaly $a \equiv (g - 2)/2$ of the electron was already well measured by Crane et al. [7]. Berestetskii et al. [8] pointed out that the postulated Feynman cut-off in QED at 4-momentum transfer $q^2 = \Lambda^2$ would reduce the anomaly for a particle of mass m by

$$\delta a/a = (2m^2/3\Lambda^2). \tag{1}$$

Therefore a corresponding measurement for the muon with its 206 times larger mass would be a far better test of the theory at short distances (large momentum transfers). (At present the comparison with theory for the electron is 35 times better than for the muon; but to be competitive it needs to be 40 000 times better! The muon is by far the better probe for new physics).

In 1956 parity was conserved and muons were unpolarized, so there was no possibility of doing the experiment proposed by Berestetskii. But in 1957 parity was violated in the weak interaction and it was immediately realized that muons coming from pion decay should be longitudinally polarized. Garwin, Lederman and Weinrich [9], in a footnote to their classic first paper confirming this prediction, used the $(g-2)$ precession principle (see below) to establish that its gyromagnetic ratio g must be equal to 2.00 to an accuracy of 10%. This was the first observation of muon $(g-2)$ just 47 years ago. In 1958 the Rochester conference took place at CERN; Panofsky [10] reviewing electromagnetic effects said that three independent laboratories, two in the USA and one in Russia, were planning to measure $(g - 2)$ for the muon. In the subsequent discussion it was clear that leading theorists expected a major departure from the predicted QED value, either due to a natural cut-off (needed to avoid the well known infinities in the theory) or to a new interaction which would explain the mass of the muon. At about this time a small group in CERN started to study the problem, and in 1961 published their first result.

The g-factor relates the magnetic dipole moment to the intrinsic angular momentum of a charged system. Classically, the dipole moments can arise from either charges or currents. For example, the circulating particle with electric charge e, mass m and angular momentum $\vec{L}$ has associated with it a magnetic dipole moment

$$\vec{\mu}_L = \frac{e}{2mc}\vec{L}. \tag{2}$$

On the other hand, the electric dipole moment of some polar molecules is due to the relative displacement of the centres of the positive and negative charge. Thus we have examples of a magnetic dipole moment and an electric dipole moment both having their origins in electric charge, and it is interesting to note that all electromagnetic phenomena are explained in terms of electric charges and their currents; there is no place, as yet, for magnetic poles. In particular, the intrinsic magnetic dipole moments of all particles can be considered, in the classical picture, to be made up of circulating electric currents and not of distributed magnetic charges [11]. This is just one aspect of the basic asymmetry between electricity and magnetism, which is apparent in Maxwell's equations. The argument of Dirac [12], that the existence of a magnetic pole would lead naturally to the quantization of both magnetic and electric charge, still stands as a challenge to physicists, both theoretical and experimental, to find a proper place for the magnetic monopole in the electromagnetic theory and to establish its physical reality. The Dirac equation permits any value of g for the electron or muon, through the possible presence of the Pauli term, but the simplest version without Pauli term implies $g = 2$. To this must be added the corrections due to quantum electrodynamics which it is the purpose of the experiment to measure. For a particle with both magnetic and electric dipole moments, the electromagnetic interaction Hamiltonian contains a part

$$H = -\vec{\mu} \cdot \vec{B} - \vec{d} \cdot \vec{E} \tag{3}$$

where $\vec{B}$ and $\vec{E}$ are the magnetic and electric field strengths, and $\vec{\mu}$ and $\vec{d}$ are the magnetic and electric dipole moments. Following the general form of (2), we can write

$$\vec{\mu} = g\frac{e}{2mc}\frac{1}{2}\left(\frac{h}{2\pi}\right)\vec{\sigma} = (g/2)\mu_0\vec{\sigma} \tag{4}$$

$$\vec{d} = \eta\frac{e}{2mc}\frac{1}{2}\left(\frac{h}{2\pi}\right)\vec{\sigma} = (\eta/2)\mu_0\vec{\sigma} \tag{5}$$

where the components of $\vec{\sigma}$ are the three Pauli spin matrices and $\mu_0 = eh/4\pi mc$ (the Bohr magneton). Note that this quantity is proportional to an electric charge e times the Compton wavelength, so curiously the same unit is appropriate for both the magnetic moment and the electric dipole moment (EDM). The expectation value d of the EDM must be zero for a particle described by a state of well-defined parity. (The polar molecules referred to above are in a mixture of degenerate states with opposite parities and are not covered by this symmetry condition). Invariance under time reversal also requires the EDM to vanish as a consequence of the different symmetry properties of the magnetic and electric fields. Whilst $\vec{B}$ is an axial vector, $\vec{E}$ is a polar vector. Thus if the Hamiltonian equation (3) is to remain invariant with respect to parity inversion P and time reversal T, then μ must transform like an axial vector and d must transform like a polar vector. From Eqs. (4) and (5)

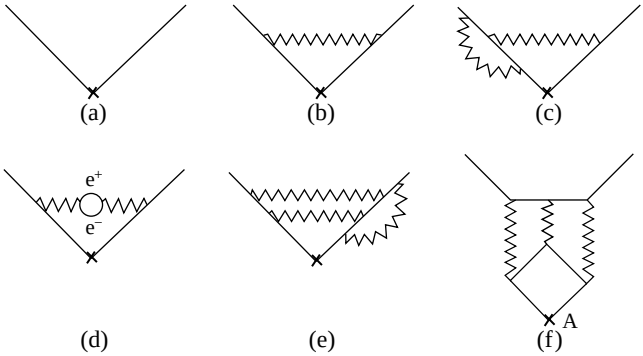

Fig. 1. Some of the Feynman diagrams used in calculating a. The solid line represents the muon, which interacts with the laboratory magnetic field at X. The zigzag line represents a virtual photon, which is emitted and later reabsorbed. In (d) and (f) a virtual e^+e^- pair is created and then annihilates, making the closed loop (solid line). In the "scattering of light by light" diagram (f) the electron loop interacts with the magnetic field at A and three virtual gammas connect to the muon line.

we see that the dipole moment operators should transform like the spin operator σ. Since this latter behaves like an axial vector, all is consistent for μ; but in the case of d, either of the operations P or T changes the relative sign of the two sides of the equation. In order to have a satisfactory situation, η must be zero. These arguments can be generalized to show that for a system of definite parity, the odd electric (dipole, sextupole, etc.) and even magnetic (quadrupole, octupole, etc.) moments must be zero. Since the discovery that Nature does not respect parity invariance, however, the invariance of interactions with respect to symmetry operations must always be underpinned by experiments.

2. Survey of the theory

2.1. Quantum electrodynamics

If the muon obeys the simple Dirac equation for a particle of its mass (206 times heavier than an electron), then $g = 2$ exactly; but this is modified by the quantum fluctuations in the electromagnetic field around the muon, specified by the rules of QED, making g larger by about 1 part in 800. The gyromagnetic ratio is thus increased to $g = 2(1 + a)$ where a is the anomalous magnetic moment or anomaly. The quantum effects include the rare fluctuations, which involve virtual pion states, strongly interacting vector mesons, bosons of the weak interaction and perhaps other particles as yet unknown. The main motivation for measuring the $(g - 2)$ of the muon is to see whether the known particles play their predicted roles or whether there is something more to be discovered. For some recent reviews of the theory see [13]. In quantum electrodynamics the lepton g-factor is expressed as a perturbation series in powers of α/π:

$$a^{\mathrm{QED}} = A(\alpha/\pi) + B(\alpha/\pi)^2 + C(\alpha/\pi)^3 + \cdots. \tag{6}$$

Typical Feynman diagrams, which contribute to the calculation of the theoretical value of a for the electron and the muon, are shown in Fig. 1, whilst a complete set of diagrams

Table 1
Values of the coefficients in the QED expansion (6) for the muon. (Errors in the final digits are shown in brackets)

A	0.5	
B	0.765 857 376	(27)
C	24.050 508 98	(44)
D	126.07	(41)
E	930	(170)

up to order $(\alpha/\pi)^4$ is given by Kinoshita et al. [14]. The calculations of the coefficients in (6) have taken over 40 years and been extended gradually to higher and higher orders, long computer runs being required to evaluate some of the integrals: and the work continues. Details are given in [15–17], and the results, summarized in [18], are given in Table 1. Note that the values of B and higher coefficients include small contributions from loops involving the τ lepton. Fig. 1(f) involves an electron loop connecting four virtual photons, which can in principle lead to the scattering of light by light, an effect too small to be observed experimentally. It contributes to the $(\alpha/\pi)^3$ term in the muon $(g-2)$ with a large coefficient; see below. The most accurate value of the fine structure constant α is obtained from the $(g-2)$ measurement for the electron [16]

$$\alpha^{-1} = 137.035\,999\,58\ (52)\ (0.004\ \text{ppm}).$$

Substituting in (6) the result for the muon is

$$a^{\text{QED}} = 116\,584\,705.7\ (2.9) \times 10^{-11} \tag{7}$$

with an error of 0.025 ppm.

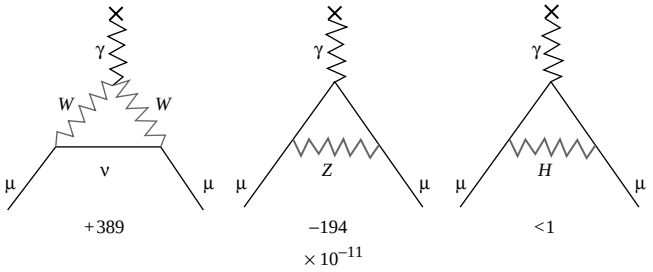

Fig. 2. One-loop electroweak radiative corrections to a.

2.2. Electroweak

In the standard model further additions to a come from the emission and reabsorption of virtual W- and Z-bosons plus a small contribution from the Higgs, as indicated in the diagrams of Fig. 2. These have been evaluated by many authors [19] with the result

$$a^{\text{EW1}} = 195 \times 10^{-11} \tag{8}$$

with negligible error. The higher order electroweak diagrams are however important and a full two loop calculation [20] gives

$$a^{\mathrm{EW2}} = -43\ (4) \times 10^{-11} \tag{9}$$

so the net result is

$$a^{\mathrm{EW}} = 152\ (4) \times 10^{-11} \tag{10}$$

with an error of 0.04 ppm in a.

2.3. First order hadronic

Strongly interacting particles do not interact directly with the muon, but if they are charged, they couple to the photon. Thus they can appear in the inner loops, such as Fig. 1(d), for example, with a pion pair replacing the e^+e^- pair. Because of the high mass of the pion, one would initially expect such amplitudes to be small, but there are strong resonances (such as ρ, ω, ϕ) in the $\pi^+\pi^-$-system that enhance the effect. Only a vector resonance can contribute, because it alone can transform directly into the virtual photon which must have $J^{PC} = 1^{--}$ (one unit of angular momentum, negative parity, and negative charge conjugation).

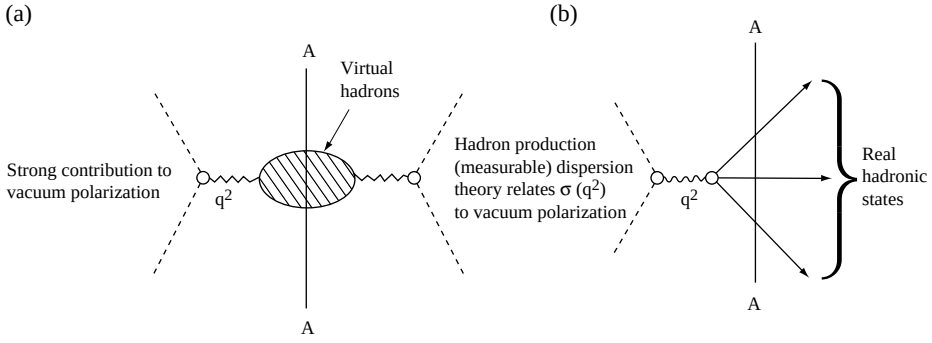

Fig. 3. The photon propagator is modified by the creation of virtual hadrons (a). This is related by dispersion theory to real hadron production in e^+e^- collisions (b).

This contribution is large, ∼59 ppm in a. To calculate it one must to specify the overall probability amplitude for a photon of a given q^2 to connect the two muon vertices shown in Fig. 1(b), with the effect of virtual hadron loops fully included; that is, one requires the propagator function of Fig. 3(a). This cannot be calculated from theory, because not enough is known about hadrons. In the region of low q^2 which applies here, quantum chromodynamics (QCD) has a strong coupling constant and perturbative expansions are hardly valid. However attempts are now made to calculate a by solving the QCD equations by successive approximation on a lattice of space–time points [21]. Fortunately, by appealing to analyticity and unitarity, the propagator in Fig. 3(a) can, in principle, be cut in half to obtain that of Fig. 3(b), which shows an e^+e^- pair annihilating to give real

hadronic states. By using dispersion theory, the cross-section for Fig. 3(b) as a function of $s =$ (centre of mass energy)^2 can be related to the propagator shown in Fig. 3(a), and so to the anomalous moment arising from Fig. 1(d) with hadron loops:

$$a^{\mathrm{HAD1}} = \frac{1}{4\pi^3}\int_{4m_\pi^2}^{\infty} \sigma(s)(\mathrm{e^+e^-} \to \text{hadrons})K(s)\,\mathrm{d}s \tag{11}$$

where $\sigma(s)(\mathrm{e^+e^-} \to \text{hadrons})$ is the measured cross-section for hadron production by one photon exchange in $\mathrm{e^+e^-}$ collisions, corrected for vacuum polarization and initial state radiation. (These corrections can be quite large (∼20%) and are not easy to determine.) s is the square of the centre of mass energy and $K(s)$ is an algebraic function given by

$$K(s) = x^2\left(1 - \frac{x^2}{2}\right) + (1+x)^2\left(1 + \frac{1}{x^2}\right)\left[\ln(1+x) - x + \frac{xc^2}{2}\right] + \frac{1+x}{1-x}x^2\ln x \tag{12}$$

with $x = (1-\beta)/(1+\beta)$ and $\beta = (1 - 4m_\mu^2/s)^{1/2}$. $\sigma(s)(\mathrm{e^+e^-} \to \text{hadrons})$ can be obtained by measuring the ratio $R(s)$ of hadron to muon production in the same colliding beam,

$$R(s) = \frac{\sigma(\mathrm{e^+e^-} \to \text{hadrons})}{\sigma(\mathrm{e^+e^-} \to \mu^+\mu^-)}, \tag{13}$$

the denominator being known from QED. Alternatively the luminosity (number of collisions per second) may be calibrated by observing Bhabha scattering in the $\mathrm{e^+e^-}$ interactions. The calibration must be done independently for each centre of mass energy.

$R(s)$ has been measured over many years by varying the energy of the colliding $\mathrm{e^+e^-}$ beams, typical results being shown in Fig. 4. Accurate data from the two pion threshold up to 1.4 GeV centre of mass energy, have been obtained at Novosibirsk [22]: because of the ρ resonance at 770 MeV and the factor $K(s)$ which favors low energies, 72% of a^{HAD1} comes from this region. Beijing [23] has covered the range 2.0–5 GeV.

More recently data has been recorded at Frascati [24] with $\mathrm{e^+e^-}$ colliding at a fixed energy, 1.02 GeV in the centre of mass, to coincide with the Φ resonance. If one of the incoming leptons radiates a hard gamma, the energy available for the pion pair is reduced. The group measure the cross-section as a function of the energy of the pion pair (the radiated gamma is not detected), and using QED they calculate $R(s)$. In this case the normalization is automatically the same for all values of s, so the method gives a good independent check on the shape of the curve of R versus s. It is particularly good for low values of s which are difficult to reach with the normal colliding beams (low luminosity). The value of $R(s)$ at threshold is known independently from the pion form factor [25].

One of the main difficulties in analyzing the data is to make the correct allowance for vacuum polarization and radiation by the incoming leptons; the computation depends on the resolution of the detectors in energy and angle, and so tends to be specific to a particular apparatus. (Final state radiation is comparatively small because of the higher pion mass.) It is difficult to get a^{HAD1} to better than 1%. Recent very careful evaluations are in reasonable agreement as shown in Table 2 below.

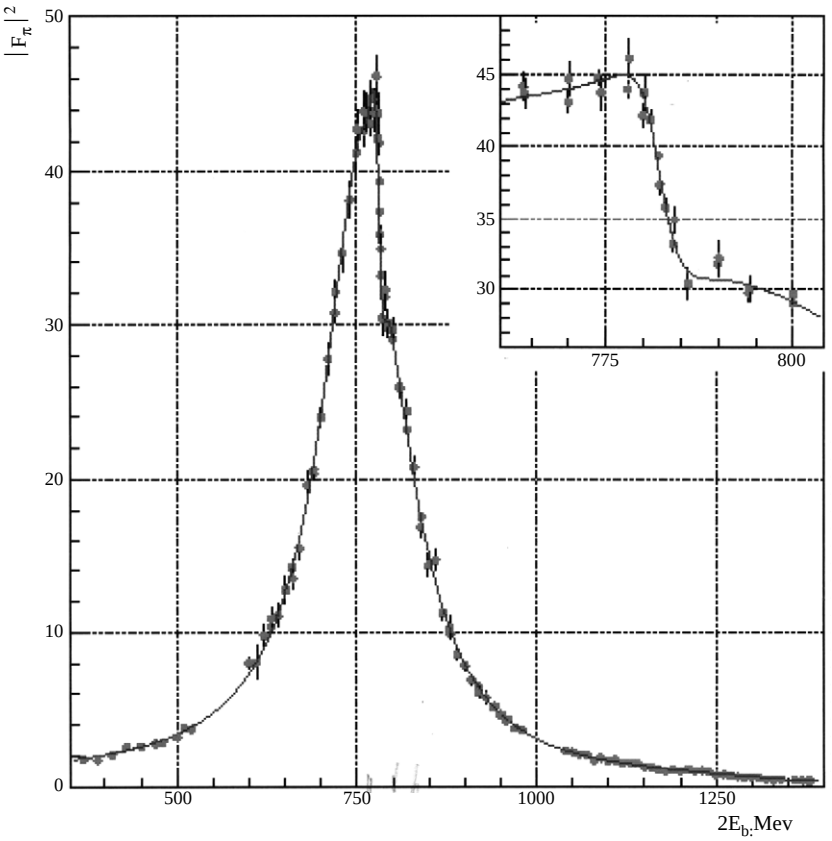

Fig. 4. The cross-section for hadron production in e^+e^- collisions as a function of centre of mass energy.

However, the Novosibirsk data have now been corrected [126] for an error in the luminosity measurement, leading to revised results for a^{HADI}, also given in Table 2.

If one believes the standard model the same information is available from the branching ratios in $\tau^{\pm}$ decay which is mediated by virtual $W^{\pm}$ intermediate bosons. For example, the W^- couples to $(\mu^-, \bar{\nu_\mu})$, the normal weak interaction, but also to a multiplicity of hadronic states with total electric charge -1. The conserved vector current hypothesis [26] relates this "charged current" interaction to the "neutral current" coupling of a virtual gamma to the same hadronic states. From the τ branching ratios one can derive the amplitude for the charged "spectral function" (up to an energy of 1.8 GeV) and thus compute the corresponding quantity for the coupling of the virtual gamma to hadrons at the same q^2: just what is needed in formula (11) to calculate a^{HAD1}. The miracle is that this works. The disappointment is that it does not work perfectly: the two results differ by about 1%.

Of course CVC is not perfect and the hadronic states produced are not identical: τ^- decays to $\pi^-\pi^0$ (isovector), while e^+e^- produces $\pi^+\pi^-$ (a mixture of isoscalar and isovector), and the π^- and π^0 have different masses. The spectral function is dominated

Table 2
Values of the lowest order hadronic contribution to $a^{\mathrm{HAD1}} \times 10^{11}$

Using 2001 data			
Jegerlehner	e^+e^-	6836 (86)	[28]
Davier et al.	e^+e^-	6847 (70)	[27]
Hagiwara et al.	e^+e^-	6831 (62)	[29]
Davier et al.	τ decay	7019 (62)	[27]
Using 2003 data			
Davier et al.	e^+e^-	6963 (72)	[127]
Ghozzi and Jegerlehner	e^+e^-	6948 (86)	[128]

by the ρ resonance; but ρ^0 and ρ^- have different masses. The ω should not couple to the two pion final state; but it shows up in the cross-section as ρ/ω interference, which gives the sharp drop at the right of the ρ peak in Fig. 4. It does not appear in τ decay because the ω is neutral. Davier and his colleagues [27] make sophisticated corrections for all these CVC breaking effects. The long-standing discrepancy between the e^+e^- data and the τ data has recently been ascribed [128] to the different resonance parameters for the $\rho^\pm$ and the ρ^0. The $\rho^\pm$ (seen in τ-decay) is about 4.6 MeV heavier and is wider than the ρ^0 (seen in e^+e^- collisions) and this makes the integral (11) larger. Correcting for this effect appears to resolve the discrepancy. It is now generally agreed that the e^+e^- results should be used to confront the experimental value of a, while the τ data are useful for testing CVC.

This is not the end of the story: there are higher order hadronic effects which are small but significant, to be discussed next.

2.4. Higher order hadronic

The higher order hadronic diagrams shown in Fig. 5 have a loop of virtual hadrons, as in the first order hadronic, plus additional gammas, or extra loops of electrons or hadrons. These have been evaluated by several authors [30, 31] with the consensus result

$$a^{\mathrm{HAD2}} = -100\ (6) \times 10^{-11}. \tag{14}$$

More controversial have been the "hadronic light-by-light scattering" diagrams, Fig. 5(d), so called because the four virtual photons are connected by a hadron loop, which could in principle lead to the scattering of light by light in vacuum, an effect which is too small to be observed. The analogous diagram with four photons connected by an electron loop is more important and is the main contributor to the coefficient C in Eq. (6) mentioned above; see Fig. 1(f).

For many years there was a consensus that this term $a^{\mathrm{HAD},L\times L}$ was negative, $-85\ (25)\times 10^{-11}$, that is about -0.8 ppm in a. Intuitively this was surprising because one would expect the main effect to be due a quark loop and the corresponding contribution with an electron loop is strongly positive. But the experts assured us that hadrons are more complicated.

In 2001, with an apparent discrepancy between experiment and theory emerging rather clearly (see Section 8.11), the Marseille group [32] decided to re-evaluate this term and they discovered a mistake in sign, common to all previous authors! The new calculation

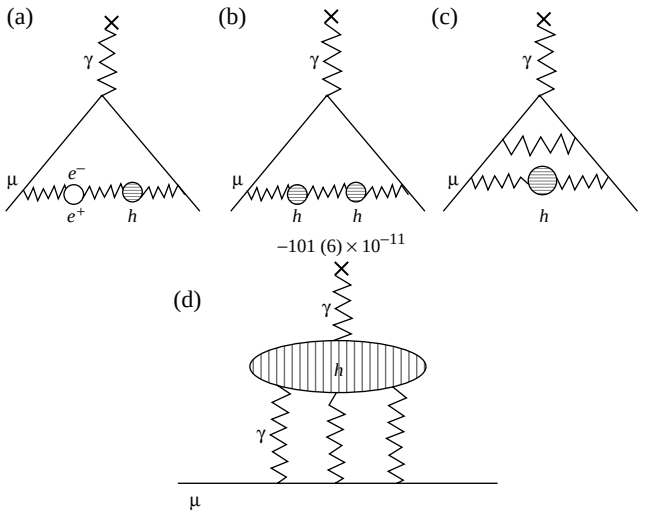

Fig. 5. Second order hadronic diagrams.

assumes that the effect is dominated by a virtual π^0 and uses approximations based on chiral perturbation theory. To allow for the difficulties a fairly large error is assigned. The change of sign was eventually confirmed by the experts [33] and the currently agreed value is

$$a^{\mathrm{HAD},L\times L} = +86\,(35) \times 10^{-11}. \tag{15}$$

The overall effect of this change was to increase the theoretical prediction for a by 1.5 ppm bringing the theory closer to the experimental value (see Section 8.11).

2.5. Standard model prediction

The current values of the various theoretical contributions to the muon anomalous moment are summarized in Table 3 together with the total prediction. One sees that the error is dominated by the uncertainty in the first order hadronic effect, for which we have adopted the mean of the latest e^+e^- values from Table 2.

2.6. New physics

It was realized from the beginning [34, 35] that any new field coupled to the muon would, like the electromagnetic field, add its own cloud of evanescent particles and give an additional contribution to the muon $(g-2)$. A search for such fields, which could perhaps explain the μ–e mass difference [10], was one of the main motives for measuring this quantity. Berestetskii's formula (1) is broadly valid for any new effect involving an energy of order Λ, with the proportionality constant adjusted according to the strength of the coupling. For example a field of mass $\Lambda = 100$ GeV and coupling constant α would change a by 0.7 ppm.

Table 3
Summary of theoretical predictions for $a \times 10^{11}$

QED	116 584 706	(3)
Electroweak first order	195	
Electroweak second order	−43	(4)
Hadronic first order	6956	(70)
Hadronic second order	−100	(6)
Hadronic $L \times L$	86	(35)
Total theory	116 591 800	(88)

There are many speculative extensions of the standard model and new papers are published almost weekly discussing the current discrepancy between experiment and theory (see Section 8.11). We cannot summarize them here but refer instead to some of the more useful reviews [13, 18]. In particular Supersymmetry (SUSY) with its multiplicity of undiscovered particles can account for a higher muon $(g-2)$ value. In the minimal SUSY model, the effect on a is dominated by the mass M of the lightest supersymmetric particle (in units of 100 GeV/c^2) and $\tan\beta$, the ratio of the Higgs masses. Approximately

$$a^{\mathrm{SUSY}} = 1.2 \text{ ppm} \times (\tan\beta / M^2). \tag{16}$$

To get a positive contribution the supersymmetry parameter μ must be positive and there must be more than one Higgs particle. There are solutions which explain the current muon $(g-2)$ value and are compatible with limits on SUSY from LEP and dark matter in the universe [36].

Ending this review of the theory, note that minor adjustments to the calculations are still being made, as theorists review their work and better experimental data on the R-value in (13) become available. This applies in particular to the hadronic first order contribution which depends entirely on the measurements with colliding beams which are steadily being improved.

3. Spin motion

3.1. Precession at rest

If a positive muon is brought to rest in a magnetic field; the spin rotates at angular frequency

$$\omega_s = (g/2)(eB/mc) \tag{17}$$

and the angular distribution of decay electrons must rotate at the same frequency. If decays are counted in a particular direction, the counting rate $N(t)$ will be modulated by the precession frequency ω_s,

$$N(t) = N_0 \exp(-t/\tau)[1 + A\cos(\omega_s t + \phi)]. \tag{18}$$

This precession frequency has been measured many times in fields calibrated in terms of the proton spin frequency ω_p. The ratio $\lambda = \omega_s/\omega_p = \mu_\mu/\mu_p$, where μ_μ and μ_p are

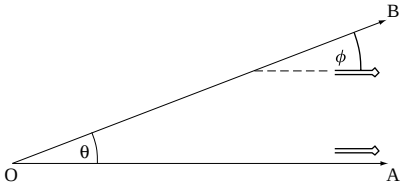

Fig. 6. Thomas precession. Initial motion along OA becomes motion along OB because of transverse acceleration. The arrow represents a gyroscope pointing in a fixed direction. At low speeds we expect $\phi = \theta$, but this is modified at velocities near c.

the magnetic moments of the muon and proton, has been determined in this way, as also from measurements of the hyperfine splitting in muonium. The current best result from muonium is [37],

$$\lambda = 3.183\,345\,39\ (10). \tag{19}$$

From Eq. (17) the g-factor of the muon could be deduced to a similar accuracy if the mass m of the muon was known. However the only independent measurement of m, from X-ray transitions in μ-phosphorus is accurate only to one part in 10^4 [38] and this confirms the theoretical value of a to about 15%. By studying the spin motion of muons in flight it proves possible to measure a frequency that is proportional not to g, but to $(g-2)$. Combined with the precession at rest this gives a precise value of g as well as the muon mass.

3.2. Precession in flight

3.2.1. Magnetic field only

Professor Crane at Ann Arbor [7] was the first to note that at low velocities the orbit frequency $\omega_c = eB/mc$ of an electron (or muon) in a magnetic field B is almost the same as its spin frequency ω_s Eq. (17). At low velocities the spin frequency is not affected by the motion and the difference frequency is a measure of the magnetic anomaly,

$$\omega_a \equiv \omega_s - \omega_c = (g/2)(eB/mc) - (eB/mc) = a(eB/mc) \tag{20}$$

so the small quantity $a \equiv (g-2)/2$ can be measured by observing the spin angle relative to the momentum vector. Thus the quantum correction to g can be determined directly and this is much more accurate than comparing the value of g with the Dirac value 2.

To calculate the spin motion for a particle rotating at relativistic speeds, it is necessary to consider the influence of the transverse acceleration, which gives rise to an effect known as the Thomas precession [39]. To explain this effect, we follow an argument developed by one of us in the Cargèse Lectures in Physics, 1968 [40].

In Fig. 6, consider a gyroscope moving parallel to the x-axis OA and pointing initially along OA. It is assumed that the gyroscope is non-magnetic and is not subject to any couple: it just has the property of pointing always in the same direction. Suppose, further, that the gyroscope is accelerated transversely so that it now moves along OB at an angle θ to the original direction. The angle between the gyroscope axis and its new direction of motion is called ϕ. As the gyroscope keeps its direction, the result expected is $\phi = \theta$.

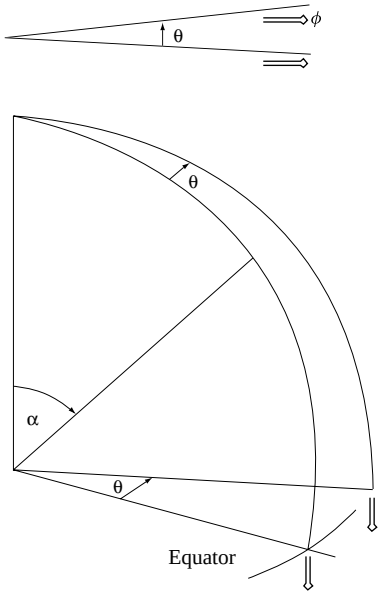

Fig. 7. Spherical trigonometry. When an arrow near the pole is displaced parallel to itself its angle relative to the lines of longitude changes. But at the equator this angle remains fixed.

But unfortunately this is not true at relativistic speeds; the direction is modified by the Thomas precession. The result can be derived in a simple way by considering rotations in Minkowski space. This involves some spherical trigonometry, so we first consider a simple geometrical problem in which no velocities are involved.

Fig. 7 shows a section of the globe with two lines of longitude separated by the small angle θ. There is an arrow near the pole, pointing due south along the meridian. Let the arrow be displaced parallel to itself until it lies on the line of longitude θ. The angle between the arrow and the new line of longitude is called ϕ. Near the pole, $\phi = \theta$. However, if the experiment is repeated at the equator the arrow will always point south: $\phi = 0$. At an intermediate latitude, designated by the angle α shown in the figure, the result will be between these two extremes. As only sine and cosine functions are involved in spherical trigonometry, it is not surprising to find that the general law is

$$\phi = \theta \cos\alpha. \tag{21}$$

Returning now to Minkowski space (Fig. 8) for a gyroscope moving at velocity v in the x-direction, the time-axis t is rotated to t' through the angle given by $\cos\alpha = \gamma = (1 - \beta^2)^{-1/2}$, with $\sin\alpha = i\beta\gamma$ where $\beta = v/c$. An acceleration in the y-direction then implies a rotation of coordinates about the axis Ox', bringing the time-axis to t''. Suppose that the gyroscope is now moving at an angle θ to the x-axis; the angle between the gyroscope and the new direction of motion is, according to Eq. (21),

$$\phi = \theta \cos\alpha = \gamma\theta. \tag{22}$$

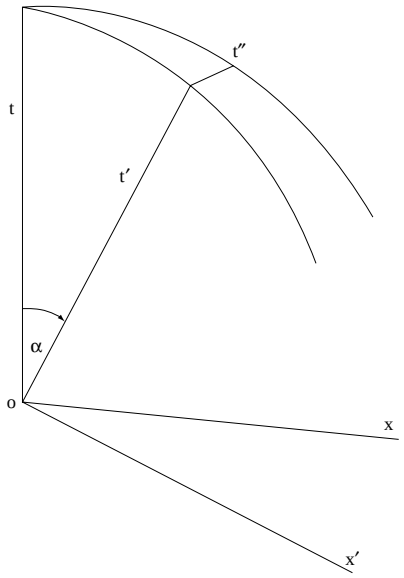

Fig. 8. Derivation of Thomas precession using Minkowski space.

The angle ϕ is greater than the classical value, because Minkowski space is not really spherical, but involves imaginary angles. In effect, when the direction of the motion is changed by θ, the gyroscope apparently rotates through an angle $(\gamma - 1)\theta$ in the opposite direction. This is called the Thomas precession and is usually thought of as a rotation of the rest-frame axes associated with the transverse acceleration [39]. A derivation of the Thomas precession using spherical trigonometry in 4-space, broadly similar to the above, was published by Sommerfeld [41]. What happens if the gyroscope is a muon and the deflection is due to a magnetic field B? Suppose that in time t the momentum vector is deflected through an angle θ_p. Allowing for the relativistic mass γm,

$$\theta_c = (e/\gamma mc)Bt. \tag{23}$$

The rest-frame axes then turn in the opposite direction through the Thomas angle:

$$\theta_t^* = (\gamma - 1)\theta_c. \tag{24}$$

(Starred quantities correspond to the rest frame, unstarred quantities to the laboratory.) In the rest frame the magnetic field $B^* = \gamma B$ acts on the spin for the time $t^* = t/\gamma$, so the spin turns relative to the axes through

$$\theta_s^* = g(e/2mc)B^*t^* = g(e/2mc)Bt = (1 + a)(e/mc)Bt. \tag{25}$$

The overall angle between the spin and the momentum vector is therefore

$$\theta = \theta_s^* - \theta_t^* - \theta_c^* = a(e/mc)Bt. \tag{26}$$

The frequency at which the spin turns relative to the momentum vector is

$$\omega_a = a(eB/mc) \tag{27}$$

which is the same as the result (20) derived for very low energies.

Combining with Eq. (17) gives

$$a = \omega_a/(\omega_s - \omega_a) = R/(\lambda - R) \tag{28}$$

where $R = \omega_a/\omega_p$ and $\lambda = \omega_s/\omega_p$. When the magnetic field in which the muons are stored is calibrated in terms of the proton resonance frequency ω_p, the experiment becomes a measurement of the ratio $R = \omega_a/\omega_p$. The muon spin frequency ω_s in the same field is then obtained from the known ratio λ (see Eq. (19) above), and this leads to Eq. (28).

Eq. (20) is thus seen to be valid for all particle velocities, and a measurement of ω_a, the rate at which the spin turns relative to the momentum vector, determines $a = (g-2)/2$ directly; the only auxiliary constant required is λ.

More formal derivations of Eq. (27) for relativistic particles were given by Mendlowitz and Case and by Carrassi using the Dirac equation [42], and by Bargmann, Michel and Telegdi using a covariant classical formulation of the spin motion [43].

It must be stressed again that the result (27) for the anomalous precession frequency ω_a does not contain the relativistic factor γ, essentially because in going to the rest frame, time is shortened by $1/\gamma$, but the magnetic field is increased by γ so the product Bt remains the same. This is why at high energies the decay lifetime for relativistic muons is lengthened, but the precession frequency remains the same as before: so more precession cycles can be measured, leading to increased precision.

3.2.2. Magnetic and electric field

If an electric field is used to focus the particles vertically as in the third CERN experiment, it may upset the spin motion. In general it does, and in fact stray radial electric fields caused considerable difficulty in the electron $(g-2)$ experiments performed by Crane et al. at the University of Michigan [44]. It turns out that these difficulties can be avoided by using muons of a carefully chosen "magic" energy. The radial component E_r of the electric field bends the particle orbit; it also induces a vertical magnetic field $B_z^* = \beta\gamma E_r$ in the rest frame and this changes the spin precession frequency. To study this in detail, we must repeat the analysis of the relativistic spin precession in the presence of the radial electric field. The deflection of the momentum vector in time t becomes

$$\theta_c = (e/\gamma mc)(B + E_r/\beta)t. \tag{29}$$

The Thomas angle is again $\theta_t^* = (\gamma - 1)\theta_c$ and $B^* = \gamma B + \beta\gamma E_r$, so

$$\theta_s^* = (1 + a)(e/mc)(B + \beta E_r)t \tag{30}$$

giving

$$\theta = \theta_s^* - \theta_t^* - \theta_c^* = a(e/mc)Bt[1 + (1 - 1/a\beta^2\gamma^2)(\beta E_r/B)]. \tag{31}$$

So the new $(g-2)$ precession frequency is

$$\omega_a' = \omega_a[1 + (1 - 1/a\beta^2\gamma^2)(\beta E_r/B)]. \tag{32}$$

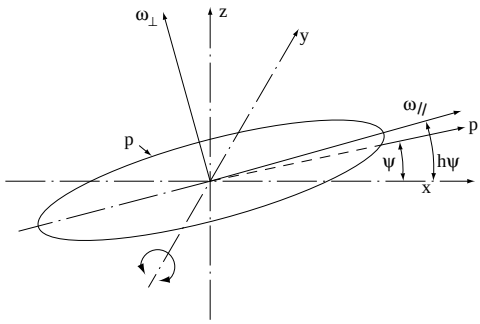

Fig. 9. Axes xyz rotating about z so that the momentum vector p lies always in the x–z plane. Owing to pitch oscillations the pitch angle ψ between p and the x-axis is varying. The spin angle is determined in the plane P (inclined at angle $h\psi$ to the x-axis) because a spin in this plane moves into the x–y plane when ψ passes through zero.

With particle mass m and momentum p, if $(p/mc)^2 = \beta^2\gamma^2 = 1/a$ the second term in Eq. (32) is zero and radial electric fields do not affect the $(g-2)$ precession frequency [45]. This corresponds to a momentum of 3.094 GeV/c which was used in the third $(g-2)$ experiment at CERN and the more recent measurement at Brookhaven (see Sections 7 and 8).

3.3. Pitch correction

The formulae for the $(g-2)$ precession frequency ω_a derived above assume that the particle orbit lies in a plane exactly perpendicular to B. If the velocity has a small angle ψ relative to this plane, the particle follows a spiral path with pitch angle ψ, and the $(g-2)$ frequency is altered. In a real storage system, the pitch angle is corrected by the vertical focusing forces, which prevent the particles being lost; the pitch angle changes periodically between positive and negative values, and the correction to the $(g-2)$ frequency becomes more complex. All the $(g-2)$ experiments for electrons and muons are in principle subject to a pitch correction. Early evaluations of the pitch correction by Wilkinson and Crane [44], Henry and Silver [46], and Fierz and Telegdi [47] were superseded by the analysis of Granger and Ford [48] which, for the first time, took proper account of the changes in pitch angle. Farley [49] obtained the same results with a different approach, and extended the analysis to include both electric and magnetic focusing. This analysis was further pursued by Field and Fiorentini [50].

Suppose the main magnetic field B_z is along the z-axis so on average the particles rotate in the x–y plane. Consider a particle at a small pitch angle ψ with respect to the x–y plane. Suppose further that the pitch angle varies harmonically at the pitching frequency ω_v owing to axial focusing forces (radial component of the magnetic field or axial electric field)

$$\psi = \psi_0 \sin(\omega_v t). \tag{33}$$

Choose a right-handed Cartesian coordinate frame (see Fig. 9) rotating about the z-axis

with the momentum vectors at the angular frequency

$$\omega_c = eB_z/\gamma mc. \tag{34}$$

The momentum vector lies always in the x–z plane but makes an angle ψ to the x-axis. The spin motion is calculated relative to this frame, and from this the frequency of spin precession relative to the momentum vector, the $(g-2)$ frequency, follows immediately. Note that B_z need not be constant; if it varies with particle position the analysis is still valid but the time average of B_z must be inserted in the final equations.

Telegdi and Fierz [47] give a general recipe for computing the spin motion. First find the frame rotating with the momentum vector. Relative to this frame the spin rotates in laboratory time around the rest frame magnetic field $\vec{B}^*$ at angular frequency

$$\omega = a(e/\gamma mc)B^*. \tag{35}$$

We distinguish two components of the spin motion: (i) due to the main field B_z, and (ii) due to the axial focusing forces. For (i), the angular velocity of the spin relative to the rotating frame P is given by (35). Resolving B_z parallel and perpendicular to the momentum, transforming to the rest frame, and recombining, one finds the x- and z-components of ω.

$$\omega_x = -\omega_0 \frac{\gamma - 1}{\gamma}\psi \tag{36}$$

$$\omega_z = \omega_0 \left(1 - \frac{\gamma - 1}{\gamma}\psi^2\right) \tag{37}$$

where $\omega_0 = a(eB_z/mc)$ is the $(g-2)$ angular frequency when $\psi = 0$ and ψ is assumed to be small.

When the axial focusing forces deflect the momentum vector vertically through the angle ψ in the x–z plane, the spin follows the momentum vector with an additional angle due to $(g-2)$ precession in the vertical plane, so it rotates in the x–z plane through the angle $h\psi$, where

$$h = 1 + \gamma a \qquad \text{for magnetic focusing} \tag{38}$$

and

$$h = 1 + \beta^2\gamma a - 1/\gamma \qquad \text{for electric focusing.} \tag{39}$$

Therefore the harmonic pitch oscillation (33) of amplitude ψ_0 produces a corresponding vertical oscillation of the spin with amplitude $h\psi_0$ giving it an instantaneous angular velocity:

$$\omega_y = h\omega_v\psi_0 \cos(\omega_v t). \tag{40}$$

The detailed equations for the spin motion in this situation were derived by Farley [49] and the argument is reproduced in [51].

The main results may be derived directly by means of a simple physical argument using Eqs. (36)–(40). We are interested in the average rotation of the spin about the z-axis, i.e. the projection of the spin on the x–y plane. Therefore consider the spin rotation in this plane at instants when the pitch angle is zero, neglecting for the average motion the small

non-cumulative nutations that occur during the pitch oscillations. The essential step is to recognize that when the pitch angle is ψ, we must determine the progress of the spin in the plane P which makes an angle $h\psi$ with the x-axis, as indicated in Fig. 9. Any spin direction lying in this plane will be turned into the x–y plane when the pitch angle again becomes zero.

The plane P also rolls sideways, to and fro, under the action of the longitudinal component B_x of the field; see (36). Integrating (36) with ψ given by (33), the maximum roll angle is $\psi_0(\omega_0/\omega_v)(\gamma-1)/\gamma$. As $\omega_0 < \omega_v/10$ in all the experiments reported here, the roll angle can be neglected in this simplified treatment.

To compute the spin motion in the plane P, resolve the angular velocities (or magnetic fields) parallel ($\omega_\parallel$) and perpendicular ($\omega_\perp$) to the plane P. From Eqs. (36) and (37),

$$\omega_\perp = \omega_z \cos(h\psi) - \omega_x \sin(h\psi) = \omega_0\{1 - \tfrac{1}{2}\psi^2[1 + (h-1)(h-1+2/\gamma)]\}. \tag{41}$$

When the pitch frequency ω_v is much greater than the $(g-2)$ frequency, $\omega_\parallel$ changes rapidly in sign and contributes nothing to the net spin precession. So, in this case, the observed spin motion will be determined by $\omega_\perp$ alone, as given by (41). The average value of ψ^2 is $\psi_0^2/2$ so the observed $(g-2)$ frequency is $\omega_0(1-C)$ with the correction factor given by

$$C = \tfrac{1}{4}\psi_0^2\{1 + (h-1)(h-1+2/\gamma)\}. \tag{42}$$

More generally the spin moves under the action of the three Eqs. (36), (37) and (40) which can be solved [49, 50] to give

$$C = \frac{1}{4}\psi_0^2\left[1 - \frac{\omega_0^2}{\gamma^2(\omega_0^2-\omega_v^2)} - \frac{\omega_v^2(h-1)(h-1+2/\gamma)}{\omega_0^2-\omega_v^2}\right]. \tag{43}$$

When the pitch and $(g-2)$ frequencies are nearly equal the spin moves out of the x–y median plane and the corrections are large, but not infinite as suggested by (43); one must refer to [50] for an exact solution. In the experiments reviewed here the pitch and $(g-2)$ frequencies are far apart, the spin stays close to the median plane and the corrections are small.

When the vertical focusing is provided by magnetic gradients, $(h-1) = \gamma a$, while for focusing by electric quadrupoles at the magic energy, $h = 1$. But the error in the correction is dominated by the uncertainty in knowing ψ_0 precisely, so in practice when the pitch frequency is much higher than the $(g-2)$ frequency the correction to be applied in both cases comes to

$$C = \psi_0^2/4 = n\langle z^2\rangle/2r^2 \tag{44}$$

where z is the instantaneous vertical excursion of the muon from the median plane in a weak focusing ring of radius r, and n is the field index. The angle brackets $\langle$ and $\rangle$ indicate the average over the orbit; more generally the average must also cover all muons in the relevant population.

4. CERN cyclotron 1958–1962

By 1958, QED was an established theory of some 10 years' standing, corroborated by accurate measurements of the Lamb shift. The g-factor of the electron was known through electron spin resonance [52] to one part per million (ppm); in 1950, Karplus and Kroll [53] had shown how to calculate the higher order corrections to g, and a numerical error in their results had been corrected by Petermann [54], Sommerfield [55], and Suura and Wichmann [56], bringing theory into line with experiment at the level of $(\alpha/\pi)^2$. Professor Crane at the University of Michigan [7] had discovered the principle of $(g-2)$ spin motion explained above and was using it to measure a for the free electron. Eq. (20) had been proved to hold for relativistic velocities.

Turning to the muon, the bremsstrahlung cross-section at high energies had been measured with cosmic rays and was shown to agree [57] with a spin assignment of $1/2$ rather than $3/2$. A similar conclusion followed from data on neutron production by cosmic-ray muons [58]. Experiments with cosmic-ray and accelerator-generated muons were in progress to compare the electromagnetic scattering of muons and electrons by nuclei. Thus evidence was accumulating that the muon behaves as a heavy electron of spin $1/2$. Berestetskii et al. [8] had emphasized that QED theory implied an anomalous magnetic moment for the muon, of the same order as for the electron, but as the typical invariant momentum transfer involved was $q^2 \sim m^2$, an experiment for the muon would test the theory at much shorter distances. Feynman [59] felt that the divergences in QED would be limited by a real energy–momentum cut-off Λ, and anticipated that Λ could be of the order of the nucleon mass. This would imply a 0.5% effect on the muon $(g-2)$. Alternatively if the muon had a structure that gave it a form factor for photon interactions, the value of a would be less than predicted.

On the other hand, it was thought [34] that the muon should have an extra interaction that would distinguish it from the electron and explain its higher mass. This could be a coupling to a new massive field, or some specially mediated coupling to the nucleon. Whatever the source, the new field should have its own quantum fluctuations, and therefore give rise to an extra contribution to the anomalous moment a. The $(g-2)$ experiment was recognized as a very sensitive test of the existence of such fields, and potentially a crucial signpost to the μ–e problem.

At this stage there was no prospect of such an experiment, but in 1957 parity violation was discovered [60], muon beams were found to be highly polarized and, better still, it was found that the angular distribution of the decay electrons could indicate the muon spin direction as a function of time [9]. The angular distribution of electrons from the decay of polarized muons agreed [61] with spin $1/2$ and was inconsistent [62] with spin $3/2$. A wide variety of muon precession and spin-resonance experiments would be carried out in the next few years [63].

The $(g-2)$ principle was invoked in the first paper on muon precession by Garwin et al. [9], who concluded out that g must be 2.00 to within 10%, because although the muon trajectory had been deflected through 100° by the cyclotron magnetic field, the muon polarization was still longitudinal. The possibility of a $(g-2)$ experiment for muons was envisaged, and groups at Berkeley, Chicago, Columbia and Dubna started to study the problem [10]. Compared with the measurement for the electron, the muon $(g-2)$ experiment

Fig. 10. The first experimental magnet in which muons were stored at CERN for up to 30 turns. Left to right: Georges Charpak, Francis Farley, Bruno Nicolai, Hans Sens, Antonio Zichichi, Carl York and Richard Garwin.

was much more difficult because of the low intensity, diffuse nature and high momentum of available muon sources. The lower value of (e/mc) made all precession frequencies 200 times smaller, but the time available for an experiment was limited by the decay lifetime, 2.2 μs. Therefore large volumes of high magnetic fields would be needed to give a reasonable number of precession cycles. One solution was to scale up the method used at Ann Arbor [64] for the electrons, using a large solenoid and injecting the muons spirally at one end. This was pursued at Berkeley [65] and finally led to a 6% measurement (Section 5).

At CERN, the work centred on the belief that it should be possible to store muons in a conventional bending magnet with a more or less uniform vertical field between roughly rectangular pole pieces. In a typical field of 1.5 T, the muon orbit would make 440 turns during the lifetime of 2.2 μs. As $a \sim \alpha/2\pi \sim 1/800$, the angle between the spin and the momentum vector would develop 800 times more slowly, giving a change in beam polarization of about 180° to be studied. The polarized muon beam from the CERN synchrocyclotron could fairly easily be trapped inside a magnet. The particles were aimed at an absorber in the field; they lost energy and therefore turned more sharply and remained inside the magnet. To prevent them re-entering the absorber after one turn, a small transverse (y-direction) gradient of the magnetic field was introduced, causing the orbits to drift sideways perpendicular to the gradient. Vertical focusing was added by means of a parabolic term in the field. If the field is of the form

$$B_z = B_o(1 + a_1 y + b_1 y^2) \tag{45}$$

where a_1 and b_1 are small, an orbit of radius ρ moves over in the x-direction through a distance $s = a_1 \pi \rho^2$ per turn (called the step size). On average, the wavelength of the vertical oscillations is $2\pi/b_1^{1/2}$.

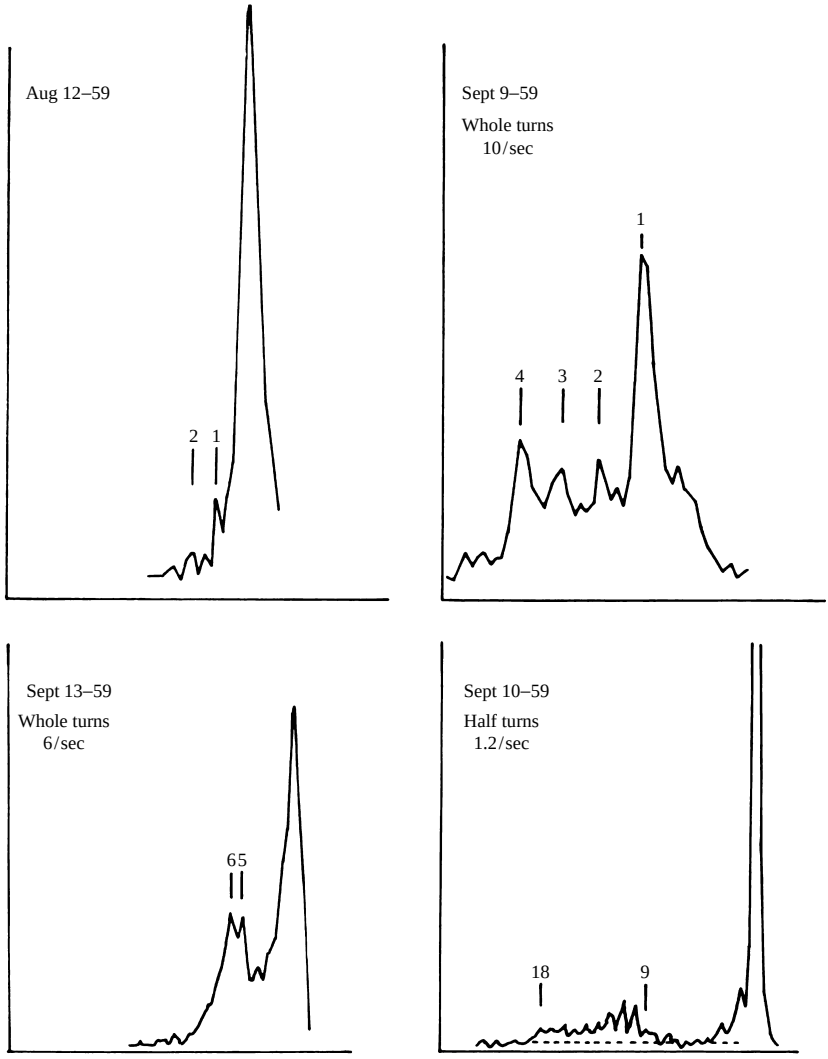

Fig. 11. The first evidence of muons making several turns in an experimental magnet, shown in Fig. 10. The time of arrival of the particles at a scintillator fixed inside the magnet is plotted horizontally (time increases to the left). The first (right-hand) peak coincides with the moment of injection. The equally spaced later peaks correspond to successive turns. Owing to the spread in orbit diameters and injection angles, some muons hit the counter after nine turns (lower right), while others take 18 turns to reach the same point (Charpak et al., unpublished).

Fig. 11 is of historical interest. It shows the first evidence of particles turning several times inside a small experimental magnet. These results gave the laboratory sufficient confidence to order a very long magnet for the experiment.

An overall view of the final storage system [66, 67] is shown in Fig. 12. The magnet pole was 6 m long and 52 cm wide, with a gap of 14 cm. Muons entered on the left through a

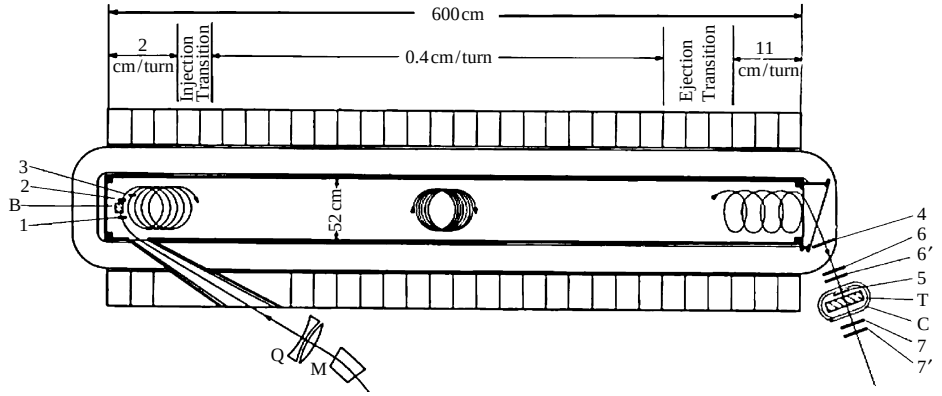

Fig. 12. The 6 m bending magnet used for storing of muons for up to 2000 turns. A transverse field gradient makes the orbit walk to the right. At the end a very large gradient is used to eject the muons which stop in the polarization analyzer. Coincidences 123 and $466'5\bar{7}$ signal an injected and ejected muon respectively. The coordinates used in the text are x (the long axis of the magnet), y (the transverse axis in the plane of the paper) and z (the axis perpendicular to the paper).

magnetically shielded iron channel and hit a beryllium absorber in the injection part of the field. Here the step size s was 1.2 cm. Then there was a transition to the long storage region, where $s = 0.4$ cm with the field gradient $a_1 = (1/B)(\mathrm{d}B/\mathrm{d}y) = 3.9 \times 10^{-4}/\mathrm{cm}$. Finally, a smooth transition was made to the ejection gradient, where $s = 11$ cm per turn. After ejection, the muons fell onto the polarization analyzer Fig. 13, where they were stopped and decayed to e^+.

The time t spent by a muon in the field was determined by coincidences in counters 123 at the input, and counters $466'5\bar{7}$ at the output. The time interval was measured with a 10 MHz crystal. The shimming of this large magnet to produce the correct gradients was a tour de force. This was assisted by the theorem that in weak gradients the flux through a wandering orbit is an invariant of the motion. Therefore, if the field along the centreline of the magnet was constant, unwanted sideways excursions would be avoided, and this could be checked more exactly by moving a flux coil, of the same diameter as the orbit, all along the magnet.

However, the constant flux theorem implied that once the particle was trapped inside the magnet it would never emerge. This was seen as a major difficulty, because the final spin direction could only be measured by stopping the muon in a weak or zero magnetic field: otherwise, one would lose track of the spin direction while waiting for the muon to decay. For weak gradients and slowly walking orbits, calculations using the first particle tracking program on a computer confirmed these doubts, and some participants lost faith in the project. Fortunately, it was found that in large gradients, of order $\pm 12\%$ over the orbit diameter, the particles were ejected successfully.

The muons were trapped in the magnet for 2–8 μs depending on the location of the orbit centre on the varying gradient given by Eq. (45). About one muon per second was stopped finally in the polarization analyzer, and the decay electron counting rate was 0.25/s.

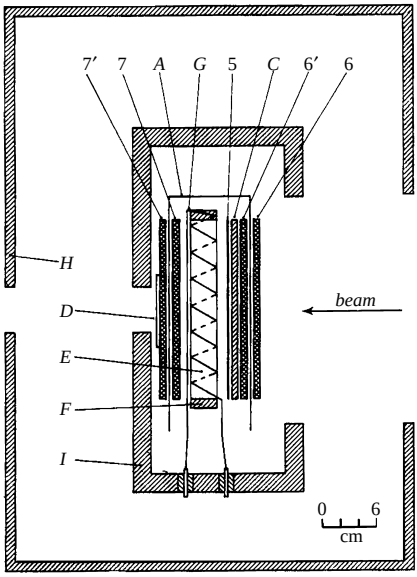

Fig. 13. The polarization analyzer. When a muon stops in the liquid methylene iodide E a pulse of current in coil G is used to flip the spin through $\pm 90°$. Backward or forward decay electrons are detected in counter telescopes $66'$ and $77'$. The static magnetic field is kept small by the double iron shield H, I and the mumetal shield A. The muon must pass the thin scintillator 5, backed by plexiglass C. D is a mirror used for alignment.

The spin direction can, in principle, be obtained from the ratio of two counting rates measured in different directions. But if two counter telescopes are used (say one forward and one backward relative to the direction of the arriving muons), it is not easy to ensure that they have equal efficiencies and solid angles. It is more reliable to use only one set of counters, but to move the muon spin direction after it has stopped. This can be done with a small constant magnetic field, but it is more efficient to turn the spin rapidly to a new position by applying a short, sharp magnetic pulse with a solenoid wound round the absorber in which the muon is stopped. This flipping was accomplished within 1 μs, and after that the gate that selected the decay electrons was opened.

In the apparatus shown in Fig. 13, the electron counts c^+ and c^- in the forward telescope $77'$ were recorded in separate runs with the spin flipped through $+90°$ and $-90°$ respectively. The asymmetry A of these counts was then related to the initial direction θ_s of the muon spin (before flipping) relative to the mean electron direction subtended by telescope $77'$:

$$A \equiv \frac{(c^+ - c^-)}{(c^+ + c^-)} = A_0 \sin\theta_s. \tag{46}$$

By flipping instead through $180°$ and $0°$ another ratio, proportional to $A_0 \cos\theta_s$, was measured; so θ_s could be determined completely. Similar, but independent, calculations were made for the telescope $66'$, which recorded the decay electrons emitted backwards.

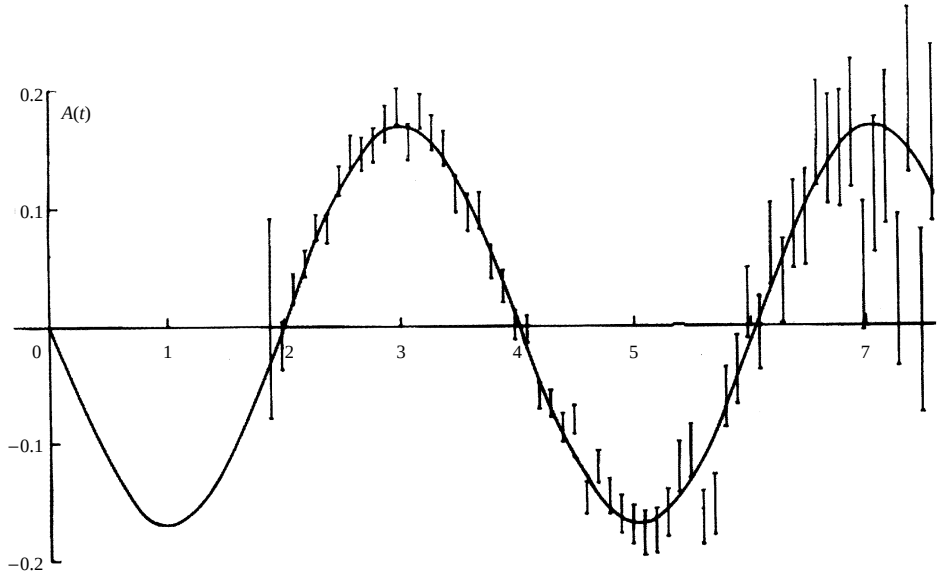

Fig. 14. Asymmetry A of observed decay electron counts as a function of the storage time t. The time t spent in the magnet depended on the transverse position of the orbit on the parabolic magnetic field (45). The muons that were stored for 7.5 μs made 1600 turns in the magnet and then emerged spontaneously at the far end. The sinusoidal variation results from the $(g-2)$ precession; the frequency is measured to $\pm 0.4\%$.

This polarization analyzer was first used to study the muon beam available for injection. For muons that had been through the magnet, the analyzer recorded the asymmetry A as a function of the time t that the particle had spent in the field. This showed a sinusoidal variation due to the $(g-2)$ precession in the magnet. Using Eqs. (20) and (46), it follows that

$$A = A_0 \sin\theta_s = A_0 \sin\{a(e/mc)Bt + \phi\} \tag{47}$$

where ϕ is an initial phase determined by measuring the initial polarization direction and the orientation of the analyzer relative to the muon beam.

The experimental data are given in Fig. 14, together with the fitted line obtained by varying A_0 and a in Eq. (47). Full discussion of the precautions that are necessary to determine the mean field B seen by the muons, and to avoid systematic errors in the initial phase ϕ, are given in [67]. The results of this experiment [66, 67] are given in Table 6 (Section 8.11). The first experiment gave $\pm 2\%$ accuracy in a and this was later improved to $\pm 0.4\%$. The figures agreed with theory within experimental errors. The corresponding 95% confidence limit for the photon propagator cut-off, Eq. (1), was $\Lambda > 1.0$ GeV.

This was the first real evidence that the muon behaved so precisely like a heavy electron. The result was a surprise to many, because it was confidently expected that g would be perturbed by an extra interaction associated with the muon to account for its larger mass [34, 35]. When nothing was observed at the 0.4% level, the muon became accepted as a

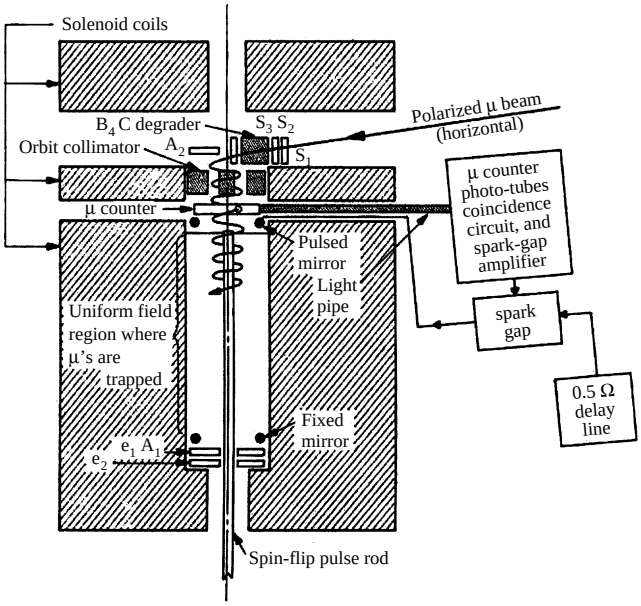

Fig. 15. The Berkeley storage system: muons enter from the right and spiral through the upper magnetic mirror into the solenoid. The mirror is then switched on to trap the particles. Decay electrons pass through the lower mirror to the detectors e_1, e_2.

structureless point-like QED particle, and the possibility of finding a clue to the μ–e mass difference now appeared more remote.

5. Berkeley cyclotron 1960–1968

An alternative approach was pursued at Berkeley using a muon beam from the 400 MeV 184" cyclotron in which the first man-made pions were produced. The apparatus was modeled on the electron $(g-2)$ experiment of Crane et al. at Ann Arbor [7, 44]. They trapped polarized electrons in a solenoid with magnetic mirrors at each end, switching the mirrors on and off to allow the particles to enter and exit.

The Berkeley experiment [65], shown in Fig. 15, used a 2.8 T solenoid with a fixed magnetic mirror at the bottom, 2% stronger than the main field, and a pulsed mirror at the top. Muons coming from the right were slowed down in a boron carbide degrader so that they began to spiral downwards into the centre of the field. When a particle passed through the counter labeled "μ-counter" it triggered a spark gap which turned on the upper magnetic mirror, trapping the muon for 6 μs or more.

The $(g-2)$ precession in the plane perpendicular to the field was observed in an ingenious way. At a chosen time t after injection, a short pulse of current was applied to a vertical rod running along the centre of the solenoid. This produced an azimuthal magnetic field along the orbit, so any transverse components of spin were flipped into the vertical plane, and this direction would be preserved until the muon decayed. The decay

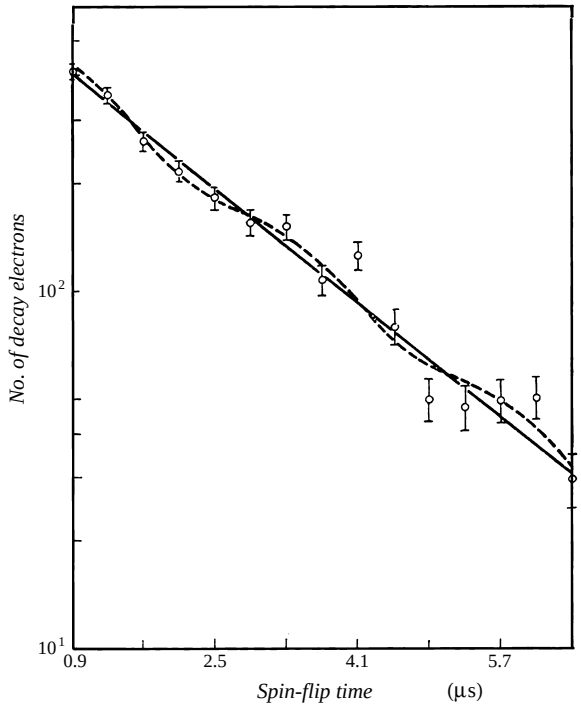

Fig. 16. Counts versus flip time t in the Berkeley experiment show a small $(g-2)$ modulation. The fit determined a to $\pm 5.7\%$.

electrons emitted downwards had sufficient energy to punch through the lower magnetic mirror and register in the detectors e_1 and e_2. The counting rate then depended on the vertical component of the muon spin, which in turn tracked the radial component at the time t when the spin was flipped. Results accumulated with various flip times t, plotted in Fig. 16, show a $(g-2)$ modulation of rather small amplitude. Fitting the frequency [65] gave $a = 1060\ (67) \times 10^{-6}$.

We estimate the pitch correction in this case, Eq. (42), using the relation for particles spiraling in a solenoid with variable axial field B. For small pitch angles ψ,

$$\Delta(\psi^2) = \Delta B/B. \tag{48}$$

The magnetic mirrors at Berkeley had a field 2% greater than the main field, so $\psi^2 = 0.02$ along the main track of a particle that was just reflected. One suspects that the majority of the muons would have been close to this maximum angle, because the acceptance would then have been the greatest. With $\omega_p \gg \omega_a$, Eq. (42) implies a pitch correction of 1% increasing the observed value of a to $1071\ (67) \times 10^{-6}$ which is $8.1 \pm 5.7\%$ below the theory.

The difficulty of the experiment resulted in an error rather larger than the measurement with the CERN cyclotron. Injecting muons from outside into a high field solenoid is

delicate. Only a narrow range of momenta and angles can lead to successful trapping. (Crane side-stepped this problem by starting with an electron gun inside the field). In consequence the counting rates of decay electrons were only 2/min. Optimizing the experimental parameters under these conditions was a slow and tedious process. In the circumstances, making the equipment work and getting a result must be regarded as a heroic achievement.

6. First muon storage ring 1962–1968

6.1. Overview

By now the CERN proton synchrotron (PS) and Brookhaven alternating gradient synchrotron (AGS) were operating, and the distinct properties of the two neutrinos ν_e and ν_μ had been established [68], further emphasizing the parallel but dual behavior of the muon and the electron. Muon pair production by 1 GeV gamma rays on carbon was measured by Alberigi-Quaranta et al. [69] in agreement with theory. With this and the $(g-2)$ data, the evidence for point-like behavior was now much better for the muon than for the electron. The scattering of muons by lead and carbon [70] agreed with the form factors deduced from electron scattering. Logically this was the best evidence for the point-like behavior of the electron, but was generally seen as another contribution to our knowledge of the muon. Knock-on electrons from 8 GeV muons confirmed the picture [71]. Muonium formation in high pressure argon had been observed by Hughes et al. [72], who went on to measure the hyperfine splitting of the ground state confirming the theoretical picture to one part in 2000 [73]. For this and subsequent muonium experiments the $(g-2)$ result was an essential input, not only for the g-factor, but also for deducing the muon mass from the precession frequency at rest, now determined to 16 ppm by Hutchinson et al. [74]; see Eqs. (17) and (20).

The muon $(g-2)$ experiment was now the best test of QED at short distances. For this reason, and to search again for a new interaction, it was desirable to press the accuracy of the experiment to new levels. It would be essential to increase the number of $(g-2)$ cycles observed, either by increasing the field B or by lengthening the storage time. With the CERN PS available, it was attractive to see what could be done by using high energy muons with relativistically dilated lifetimes. As there is no factor γ in Eq. (20), the $(g-2)$ precession frequency would not be reduced, and more cycles would be available before the muons decayed. But to store muons of GeV energy in a magnetic field and measure their polarization required totally new techniques. Farley [75] proposed to measure the anomalous moment using a muon storage ring.

The experiment is made possible by four miracles of Nature. (First identify your miracle, then put it to work for what you wish to do!) The first miracle is that it is easy to inject muons into a storage ring. One simply injects pions for a few turns; they decay in flight and some of the muons produced will fall onto permanently stored orbits. The easy way to inject pions is to put the primary target of the accelerator inside the storage magnet and hit it with high energy protons, thus producing the pions inside the ring. The second miracle is that the stored muons come from forward decay, so they are strongly polarized. The third miracle is that when the muons decay the electrons have less energy; they are

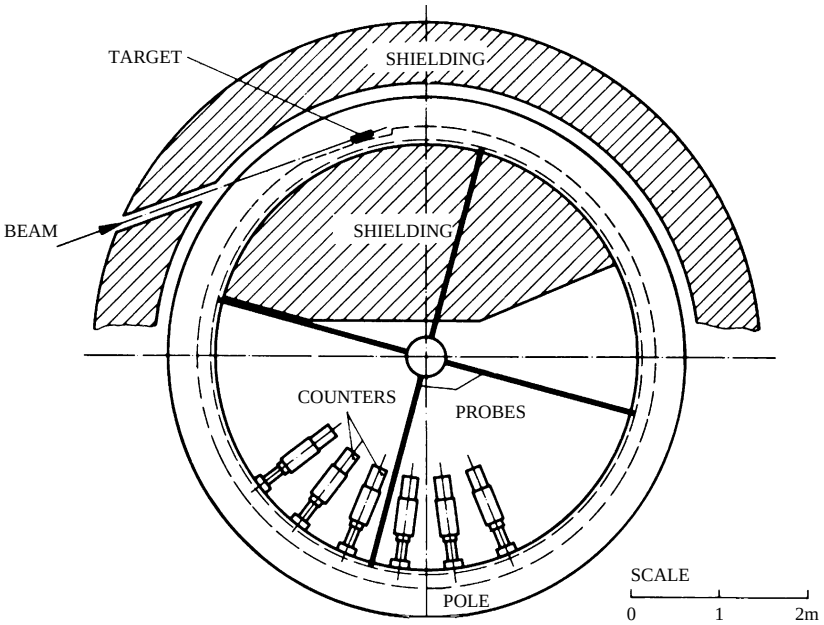

Fig. 17. The first muon storage ring: diameter 5 m, muon momentum 1.3 GeV/c, time dilation factor 12. The injected pulse of 10.5 GeV protons produces pions at the target, which decay in flight to give muons.

bent by the field and come out on the inside of the ring; the higher energy electrons must come from forward decay so as the spin rotates, the electron counting rate is modulated at the $(g-2)$ frequency ($\sim$270 kHz). One just reads it off.

A great advantage of this method is that it works equally well for μ^+ and μ^-. Most muon precession experiments can only be done with μ^+, because stopped μ^- are captured by nuclei and largely depolarized.

It was later realized that the injected muons would be localized in azimuth (injection time 10 ns, rotation time about 50 ns), so the counting rate would also be modulated at the much faster rotation frequency ($\sim$20 MHz). This would enable the mean radius of the stored muons to be calculated, leading to a precise knowledge of the corresponding magnetic field.

The first muon storage ring [76–78] was a weak focusing ring (Fig. 17) with $n = 0.13$, orbit diameter 5 m, a useful aperture of 4 cm $\times$ 8 cm (height $\times$ width), a beam momentum of 1.28 GeV/c corresponding to $\gamma = 12$ with a dilated muon lifetime of 27 μs. The mean field at the central orbit was $\bar{B} = 1.711$ T. The injection of polarized muons was accomplished by the forward decay of pions produced when a target inside the magnetic field was struck by 10.5 GeV protons from the CERN PS. The proton beam consisted of either two or three radio-frequency bunches (fast ejection), each $\sim$10 ns wide, spaced by 105 ns. As the rotation time in the ring was chosen to be 52.5 ns, these bunches overlapped exactly inside the ring. Approximately 70% of the protons interacted, creating, among other things, pions

of 1.3 GeV/c that started to turn around the ring. The pions made, on an average, four turns before again hitting the target, and in each turn about 20% decayed.

The muons created in the exactly forward decay, together with undecayed pions and stable particles from the target, eventually hit the target and were lost. However, the decay of pions at small forward angles gave rise to muons of slightly lower momentum, and some of these fell onto orbits that missed the target and remained permanently stored in the ring. Thus the perturbation, essential for inflection into any circular machine, was here achieved by the shrinking of the orbit, arising from the change of momentum in π–μ decay (and to some extent by the change in angle at the decay point, which could leave the muon with a smaller oscillation amplitude than that of its parent pion). The muons injected in this way were forward polarized, because they came from the forward decay of pions in flight. About 200 muons were stored per PS cycle. The muon injection was accomplished in a time much shorter than both the dilated muon lifetime (27 μs) and the precession period of the anomalous moment (3.7 μs).

6.2. Injecting muons into storage rings

The number of muons N_μ stored per interacting proton depends on the method of injection and the ring parameters; (i) the aperture of the storage ring (u in the horizontal plane, v in the vertical); (ii) the radius r of the ring; (iii) the magnetic field B; and (iv) the field index $n = (r/B)(\mathrm{d}B/\mathrm{d}r)$.

$$N_\mu = F\frac{u^3 v}{r^4} n^{1/2}(1-n)^{5/2} \cdot p_\pi \cdot Y \tag{49}$$

where Y is the yield of pions (per GeV/c and steradian), which depends on the proton and the pion momenta, and F is a numerical factor. The formula is the product of the following factors: the angular acceptance in the vertical plane $n^{1/2}(v/r)$, the angular acceptance in the horizontal plane $(1-n)^{1/2}(u/r)$, the momentum bite for the pions $(1-n)(u/r)p_\pi$, and finally the accepted fraction of the muon momentum spectrum $(1-n)(u/r)$. In F the probability of the pions decaying while crossing the storage volume must be included. This probability is high when protons are injected onto an internal target in the ring, because the pions can make several turns; it is lower in the case of pion injection through an inflector; and it is very low in the case of trapping by backward decay. In F the losses due to the decay angles must also be included.

Three methods are available for inserting muons into the storage volume of the ring:

(i) by injecting protons and having them interact with a target located at the outer edge of the storage region;
(ii) by injecting pions of the right momentum so that they cross the storage volume and have a good chance to produce trapped muons, either by forward or by backward decay;
(iii) by directly injecting muons of the desired momentum and putting them onto stable orbits by means of a fast kicker.

The first method is the easiest and was used in this experiment. The pions of the correct momentum, produced in the internal target, travelled around the ring for about four revolutions before returning to the target; most of them decayed before this, and the

muon capture yield from the circulating pions was fairly high. Pions with wrong momenta travelled a short distance round the ring, but their much greater number meant that a considerable number of extra muons were also trapped. These muons were emitted at large angles in the pion rest frame, so the average longitudinal polarization observed was only 26% compared with 95% expected. Furthermore, when protons were injected, the general background close to the target was very high, and the decay electron counters had to be located on the opposite side of the ring (see Fig. 17). The method of injection used in this first muon storage ring had the advantage of being technically simple, but it had the following disadvantages:

(i) low muon polarization due to muons from a wide range of pion momenta;
(ii) high general background;
(iii) contamination with electrons at early times;
(iv) low average trapping efficiency.

In early tests a magnetic horn was used around the target to concentrate pions of the correct energy in the forward direction. This gave a good muon polarization, but because of increased background it was not finally adopted. The other methods of injecting muons are discussed below.

6.3. Muon polarization

With pion injection, the final muon polarization is controlled by the decay kinematics of the π–μ system. A useful general result can be derived as follows.

Suppose that particles of fixed momentum p^* and energy E^* are emitted with angular distribution $\mathrm{d}N/\mathrm{d}\Omega^* = f(\theta^*)$ in a system moving with velocity $\beta_c \cdot c$ in the laboratory. θ^* is the angle in the moving system relative to the direction of motion and Ω^* the solid angle. With $\gamma_c = (1-\beta_c^2)^{-1/2}$ the energy of the particle in the laboratory will be given by the Lorentz transformation

$$E_{\mathrm{lab}} = \gamma_c\{E^* + \beta_c p^* \cos\theta^*\}. \tag{50}$$

As

$$\Omega^* = 2\pi(1-\cos\theta^*)$$
$$\mathrm{d}\Omega^* = -2\pi\,\mathrm{d}(\cos\theta^*)$$
$$\mathrm{d}E_{\mathrm{lab}} = (\beta_c\gamma_c p^*/2\pi)\,\mathrm{d}\Omega^*,$$

so

$$\mathrm{d}N/\mathrm{d}E_{\mathrm{lab}} = (2\pi/\beta_c\gamma_c p^*)(\mathrm{d}N/\mathrm{d}\Omega^*) = (2\pi/\beta_c\gamma_c p^*)\,f(\theta^*). \tag{51}$$

The parameters β_c, γ_c and p^* are all independent of θ^*, so (51) shows that the energy distribution in the laboratory has the same functional form as the angular distribution in the moving system. If one of these is known, the other can be inferred.

As the π–μ decay is isotropic in the pion frame, $f(\theta^*) = \text{const}$, and the spectrum of muon energy in the laboratory is flat. At high energies all the particles are relativistic and the muon momentum spectrum $\mathrm{d}N/\mathrm{d}p$ is also effectively flat. The maximum from forward decay is just beyond the original pion momentum (because the backward going neutrino

gives the muon a small forward boost); the minimum is at 42% of the pion momentum. Within this spectrum there is a 1:1 correlation of decay angle θ^* with the laboratory energy $E_{\rm lab}$. So the selection of stored muon momenta by the ring magnet in effect selects the decay angles in the pion frame, and the average value of $\cos\theta^*$ gives the muon polarization.

Typically the pions go round the magnet with momentum 1–2% above the nominal central momentum. Muons with the top energy follow the same orbit as the pions and will eventually hit something and be lost. But muons with 1–3% lower momentum fall onto permanently stored trajectories. Because they come from almost forward decay the polarization is of order 97%.

6.4. Muon decay in flight

In the case of muon decay to electrons in flight the situation is more complicated because there is a spectrum of decay electrons in the muon frame and this will smear the one-to-one correlation of $E_{\rm lab}$ with θ^*, but Eq. (51) applies for each decay electron energy. The angular distribution of electrons in the muon frame is given by

$$\mathrm{d}N(y,\theta^*) = n(y)\{1 - A(y)\cos\theta^*\}\,\mathrm{d}y\,\mathrm{d}\Omega^* \tag{52}$$

where $y = p^*/p^*_{\rm max}$ defines the electron momentum p^*, the angle between the muon spin and the electron momentum is θ^* and Ω^* is the solid angle, both in the muon frame. The momentum spectrum and angular distribution are given by the Michel formulae [79]

$$n(y) = 2y^2(3-2y), \qquad A(y) = \frac{2y-1}{3-2y}. \tag{53}$$

The spectrum rises almost linearly from zero at $p^* = 0$ to a peak at the top energy. The asymmetry A is $-1/3$ at very low energy, changes sign at $y = 1/2$ and rises to 1 at the top energy.

When the muon decays in flight the electron energy is boosted by the Lorentz transformation (50). In the laboratory the spectrum (53) becomes a falling triangle with maximum number at low momentum dropping to zero at the end point which is equal to the momentum of the stored muons, Fig. 18. To have this maximum momentum in the laboratory, the electron must be emitted exactly forward and have the top energy in the muon frame; so the asymmetry for these particles in the laboratory is $A = 1$. These particles carry the maximum information about the muon spin, but there are none of them. At lower laboratory energy a mixture of electron energies and decay angles can contribute; the number rises and the asymmetry falls, crossing zero at about 30% of the muon momentum. Put simply, to have high energy in the laboratory, the electron must be emitted forwards in the muon frame. So by recording high energy decays one selects forward decays and as the muon spin rotates the number is modulated according to Eq. (52).

The highest energy decays in the laboratory frame have the same momentum as the muons, and are trapped in the magnet. But those with lower energy are bent more and exit the field on the inside of the ring. Here many of them hit one of the lead-scintillator detectors in which they produce an electron–photon shower with the result that the light

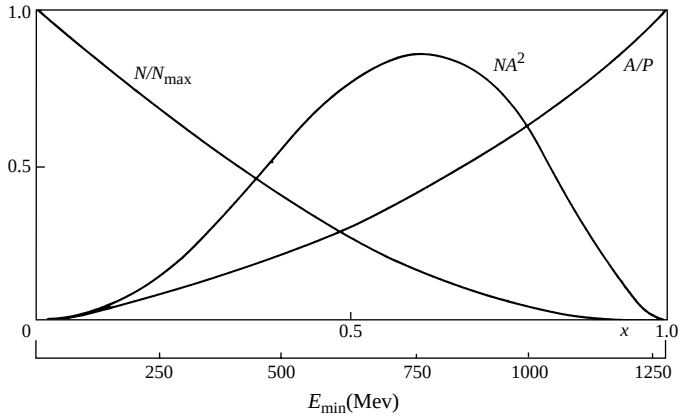

Fig. 18. The energy spectrum N of decay electrons hitting a detector: asymmetry coefficient A_{mean} and NA^2_{mean} versus E_e/E_μ. The maximum of NA^2_{mean} occurs when E_e is about 0.65 times the stored muon energy.

output is proportional to the electron energy. By selecting pulse height in the detector one selects a band of decay electron energies.

To optimize the experiment one needs to calculate the energy spectrum and asymmetry for the decay electrons which actually hit a detector. To do this one generates decay events in the computer, tracks the electron through the magnetic field and decides whether it arrives at a detector or is lost in some way. To compute the average asymmetry for the subset of particles which hit a detector it is convenient to treat the asymmetry as a vector $\vec{A}$ whose direction is along the electron momentum in the muon frame and whose length is given by $A(y)$ in (53). Then if the direction of the muon spin direction is given by the unit vector $\vec{s}$, Eq. (52) can be rewritten using the scalar product $\vec{s}\cdot\vec{A}(y)$ to read

$$\mathrm{d}N(y,\theta^*) = n(y)\{1-\vec{s}\cdot\vec{A}(y)\}\,\mathrm{d}y\,\mathrm{d}\Omega^*. \tag{54}$$

Summing over N decays, the overall asymmetry for a given set of electrons (for example those that have a particular energy and hit a particular detector) will be given by the average vector

$$\vec{A}_{\text{mean}} = (1/N)\sum_{1}^{N}\vec{A}(y). \tag{55}$$

This is easy to compute and is valid for any muon spin direction. The length of $\vec{A}_{\text{mean}}$ gives the magnitude of the asymmetry and its direction gives the phase of the $(g-2)$ precession to be expected. The results of a typical calculation are given in Fig. 18.

Summarizing this section, the muons precess inside the storage ring according to (20). When they decay the electrons emerge on the inside of the ring where they hit the detectors and produce a pulse proportional to their energy. By selecting high energy decays, one selects forward decay in the muon rest frame; so as the spin rotates the number of electrons

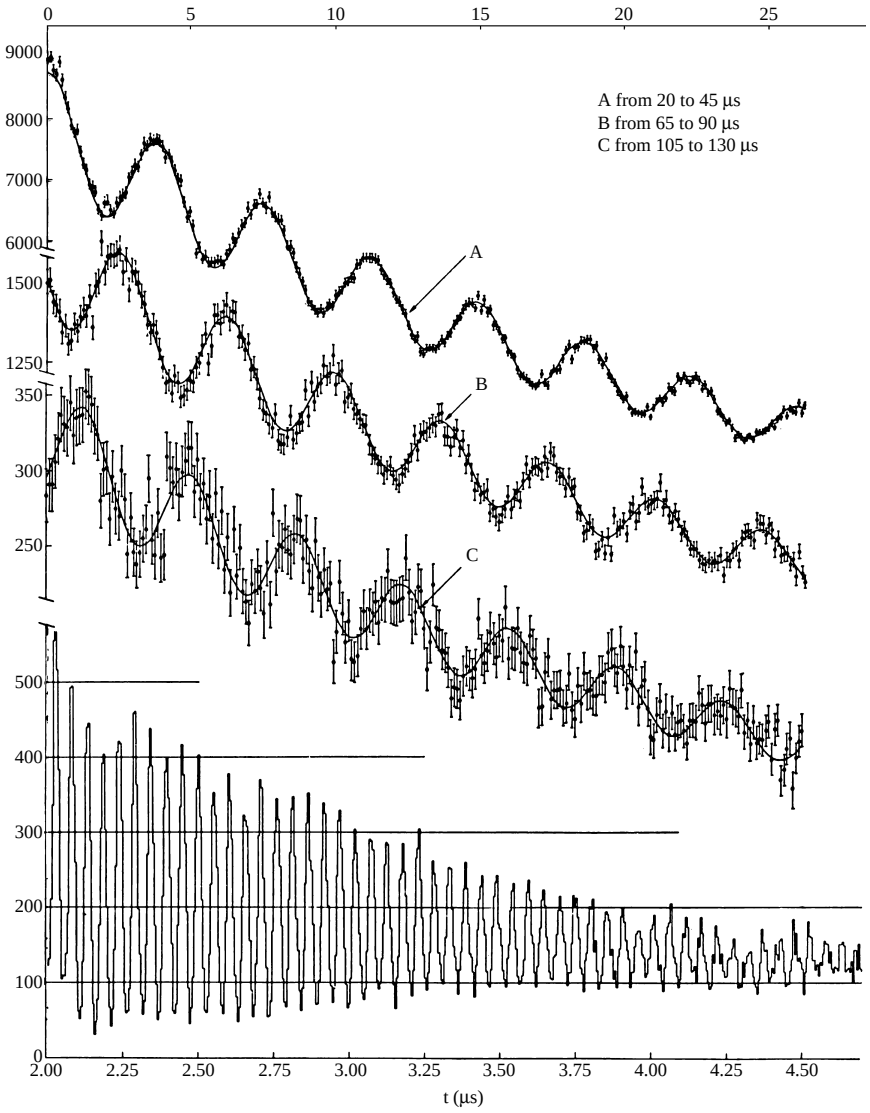

Fig. 19. The first muon storage ring: decay electron counts as a function of time after the injected pulse. The lower curve 1.5–4.5 μs (lower timescale) shows the 19 MHz modulation due to the rotation of the bunch of muons around the ring. As it spreads out the modulation dies away. This is used to determine the radial distribution of muon orbits. Curves A, B and C are defined by the legend (upper time scale); they show various sections of the experimental decay (lifetime 27 μs) modulated by the $(g-2)$ precession. The frequency is determined to 215 ppm, $\bar{B}$ to 160 ppm leading to 270 ppm in a.

is modulated by the $(g-2)$-precession and the frequency can be read from the record of counts versus time, Fig. 19.

6.5. Experimental details and results

The dilated muon lifetime was now 27 μs so the muon precession could be followed out to storage time $t = 130$ μs as shown in Fig. 19. Data for t less than 20 μs could not be used because of background due to neutrons and other effects created when the protons hit the target in the ring. The initial polarization angle of the muons is not needed for the measurement: one just fits the oscillations that are seen. With thirty $(g-2)$ cycles to fit, the accuracy in ω was now much better. Fitting a frequency ω to exponentially decaying oscillations the error is

$$\delta\omega/\omega = \frac{\sqrt{2}}{\omega\tau A\sqrt{N}} \tag{56}$$

where N is the total counts, τ the dilated lifetime and A the amplitude of the oscillations (asymmetry). To get good accuracy one should increase the number of cycles per lifetime by using high magnetic field and high energy, and maximize the product NA^2. The best value of NA^2 was obtained by accepting decay electrons above 780 MeV see Fig. 18.

The results for electron energy above this threshold were fitted by varying eight parameters in the function

$$N(t) = N_0(1 + A_L \mathrm{e}^{-t/\tau_L})\mathrm{e}^{-t/\tau}\{1 - A\cos(\omega_a t + \phi)\} + W. \tag{57}$$

In this expression the small correction term with parameters A_L and τ_L takes account of an excess of counts at early times over the extrapolated late time exponential. This is ascribed to muon losses caused by orbit perturbations. W is the late time background. The fitted frequency ω_a was insensitive to the starting time of the fit. To calculate the anomalous moment a from the fitted frequency using Eq. (28) one needs the mean proton NMR frequency ω_p corresponding to the average magnetic field seen by the stored muon population.

The magnetic field was surveyed between runs at 288 positions in the azimuth and ten radii. During the runs it was monitored by four plunging NMR probes which could be driven into the centre of the aperture. The radial magnetic gradient needed for vertical focusing implied a field variation of $\pm 0.2\%$ over the horizontal aperture of the storage ring (8 cm), so a major problem was to know the mean radius of the ensemble of muons that contributed to the data. This was obtained from the rotation frequency of the muon bunch shortly after injection. The data from $t = 1.5$–4.5 μs is shown in the lower curve of Fig. 19.

The muons are bunched at injection so there is a strong modulation of the counts at the rotation frequency. As they slowly spread around the ring, because of their range of momenta and correspondingly different rotation periods, the modulation gradually dies away. The envelope of the modulation is the Fourier transform of the frequency spectrum, or equivalently of the radial distribution. By making the inverse transform one recovers the radial distribution of the muon equilibrium orbits, Fig. 20. Using this and the map of the magnetic field, the mean field for the muon population is readily calculated. A conservatively assigned error of ± 3 mm in radius implied an error of 160 ppm in the field.

This method of finding the muon radius has one elegant advantage: it uses the same decay electron data as for fitting the $(g-2)$ frequency. In principle muons at larger radii

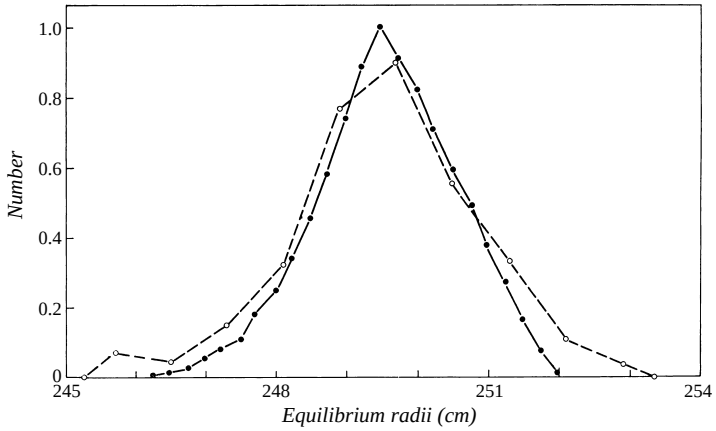

Fig. 20. The radial distribution of muons (horizontal axis, cm) derived from the analysis of the decay electron data at early times. The muon rotation frequency has been analyzed from 1.8–5.5 μs. The reconstructed muon number versus equilibrium radius (dashed line) may be compared with the radial distribution of muons predicted by the injection calculations (solid line).

have less chance of sending an electron to the counters than muons on the inside of the ring; so there is a bias, which should be corrected. But as the same detectors are used for finding the mean radius and for fitting the $(g-2)$ this error cancels out. Further details, together with checks to ensure that the measurement at early times was representative of the muon population at later times when the $(g-2)$ precession was measured, are given in [78] and the review article [51].

To calculate a from ω_a using (28) one needs the value of λ. At that time the best measurement was the experiment by Hutchinson et al. [74] of μ^+ precession in water, combined with the calculation of Ruderman [80] on the diamagnetic correction for muons in water. The result [77, 78] was

$$a = (116\,616 \pm 31) \times 10^{-8}\ (270\ \text{ppm}). \tag{58}$$

Initially, this was 1.7 standard deviations higher than the theoretical value, suggesting that there was more to be discovered about the muon. In fact the discrepancy resulted from a defect in the theory. Theorists had originally speculated that the contribution of the six $(\alpha/\pi)^3$ diagrams involving photon–photon scattering (see Fig. 1(f)) in the QED expansion for a would be small, and perhaps these terms would cancel exactly; but they had never been computed. The experimental result stimulated Aldins, Kinoshita, Brodsky and Dufner [81] to make the calculation and they obtained the surprisingly large coefficient of 18.4! The theory then agreed with the measurement, to the great satisfaction of the experimental team;

$$a_{\text{exp}} - a_{\text{th}} = 240 \pm 270\ \text{ppm}. \tag{59}$$

The limit for the Feynman cut-off, Eq. (1), was now $\Lambda > 5$ GeV.

An auxiliary result of the muon storage ring was the measurement of the lifetime for particles in a circular orbit as a check on the Einstein clock paradox [82]. The time dilation in a circular orbit was confirmed to 1%. The measured lifetime, $(26.3 \pm 0.05)\ \mu$s, was 1.2% shorter than the expected value of 26.69 μs with a statistical error of only $\pm 0.2\%$. The discrepancy was ascribed to a slow loss of muons due to imperfections in the magnetic field. A more precise verification of the Einstein time dilation is described below.

7. Second muon storage ring 1969–1976

7.1. Motivation

By 1969 an electron–electron colliding-beam experiment [83] had demonstrated the point-like nature of the electron ($\Lambda_\gamma > 4$ GeV, $\Lambda_e > 6$ GeV), and e^+e^- storage rings were giving useful data on vector meson production [84]. Experiments on e^+e^- and $\mu^+\mu^-$ pair production, on wide-angle bremsstrahlung and a comparison of e–p and μ–p scattering were all in accord with theory. Muon pair production [85] by muon bremsstrahlung (with two identical muons in the final state) showed that the muon obeyed Fermi–Dirac statistics. For reviews see [86].

The pure quantum effects were less satisfactory. The Lamb-shift data [87] were consistently higher than theory, but this was resolved by a recalculation of a small theoretical term by Appelquist and Brodsky [88]. The electron $(g-2)$ data of Wilkinson and Crane [44] had been rediscussed by Farley [40], Henry and Silver [65] and by Rich [89] who concluded that $a^e_{\rm exp} - a^e_{\rm th} = -(79 \pm 26)$ ppm. This discrepancy was to be resolved in a new measurement by Wesley and Rich [90]. Thus QED was doing well, but in early 1969, a_μ, a_e and the Lamb shift all showed uncomfortably large departures from theory. It could have been the beginning of something new.

The major motivations for carrying out a third measurement were therefore as follows:

(i) to look for departures from standard QED;
(ii) to detect the contribution of strong interactions to a_μ through the hadron loops in the vacuum polarization, see Section 2.3;
(iii) to search for new interactions of the muon.

7.2. General design

The third CERN $(g-2)$ experiment [45, 91, 92] was inspired by the first muon storage ring and the main challenge lay in the systematic difficulties of the last experiment. The announced objective [45, 93] was an accuracy of 20 ppm; the error finally quoted was 7 ppm. The design was an attempt to overcome the major sources of uncertainty in the previous experiment, which can be summarized as follows:

(i) The radial magnetic gradient required to provide the vertical focusing implied a magnetic field variation of $\pm 0.2\%$ over the aperture in which the muons were stored, and a corresponding radial dependence of ω_a. Even if the mean radius was determined precisely after injection, uncertainties in radius at the new level of accuracy would arise from uncontrolled muon losses.

(ii) The burst of particles created in the ring at injection upset the counting system and also produced a non-rotating background at early times, which made the interpretation of the data collected in the first few microseconds difficult.
(iii) In spite of careful shaping of the magnetic field, there were small muon losses up to at least 100 μs after injection.

The new project overcame the previous systematic troubles by introducing the following improvements:

(i) Using a ring magnet with a uniform magnetic field and focusing vertically with an electric quadrupole field. For the particle orbits this field is equivalent to a weak gradient in the magnetic field.
(ii) Injecting a momentum-selected beam of pions, instead of protons, into the ring in order to reduce the background.
(iii) Reducing the loss of muons by more precise field shaping and by using an electric scraper.
(iv) Increasing the intensity of the stored muons to improve the statistical accuracy in ω_a.
(v) Increasing the product $B\cdot\gamma$, thus increasing the number of $(g-2)$ cycles per lifetime, and therefore increasing the precision in ω_a.

The previous experiment showed that in a gradient field, even if the determination of the radial distribution from the muon rotation frequency was very precise, uncertainties about muon losses would give a significant error in the mean radius. Since the relative tendency of muons at different radii to be lost is unknown, the essential problem was to achieve focusing but remove the dependence of ω_a on the radius. This can be achieved in principle because the forces that hold the muon in its orbit, and give focusing for small deviations from equilibrium, arise from what appears, in the muon rest frame, as an electric field; but the spin precession is determined by what appears in the rest frame as a magnetic field. These two fields may therefore be varied independently by applying suitable magnetic and electric fields in the laboratory.

The idea in the new experiment was to use a completely uniform magnetic field, so that the $(g-2)$ frequency would be independent of muon radius and it would no longer be necessary to know where the muons were. But uniform magnets have no vertical focusing; instead an electric quadrupole with constant sign would be installed around the stored beam, giving a vertical restoring force. The associated horizontal defocusing would slightly reduce the strong semicircular focusing effect of the magnet. The combination behaves, to a good approximation, just like a weak focusing magnet with radial gradient (see Section 7.3).

However the radial electric field of the electric quadrupole can change the $(g-2)$ frequency. This was a well known effect considered in the electron $(g-2)$ experiments [44]. As the strength of the electric field would vary with radius, the muon $(g-2)$ frequency would still be a function of the radius, and nothing would be gained. The solution was to work at the "magic" momentum at which radial electric fields do not affect the $(g-2)$ frequency.

Muon precession in combined magnetic and electric fields is discussed in Section 3.2 above. Referring to Eq. (32) one sees that the condition for radial electric fields to do

nothing is $\beta^2\gamma^2 = 1/a$. This determines the "magic" momentum 3.094 GeV/c which was chosen for the second muon storage ring. The fourth miracle of Nature (Section 6.1) is that this momentum was extremely convenient. It was easily available from the CERN proton synchrotron and was a natural step up from the previous 1.28 GeV/c. The muon lifetime would be dilated to 64 μs.

7.3. Electric focusing

Using transverse coordinates x radial and z vertical relative to the central orbit in a uniform magnetic field B with electric quadrupoles all around the orbit giving fields $E_x = -kx,\ E_z = kz$, the vertical force on a particle of charge e at height z is

$$ekz. \tag{60}$$

If on the other hand the magnet had a radial gradient with field index

$$n \equiv -\frac{r}{B}\frac{\mathrm{d}B}{\mathrm{d}r} \tag{61}$$

the radial component of magnetic field at height z is found by using curl $B = 0$, giving $B_r = z \cdot (\mathrm{d}B_r/\mathrm{d}z) = n(z/r)(\mathrm{d}B_z/\mathrm{d}r)$, so the vertical magnetic force would be

$$e\beta Bnz/r. \tag{62}$$

Equating (60) and (62) one finds that the electric quadrupole is equivalent to a weak magnetic gradient with

$$n = \frac{kr}{\beta B} = \frac{2rV}{\beta B(u^2+v^2)} \tag{63}$$

where V is the voltage applied to the quadrupole electrodes with horizontal separation $2u$ and vertical separation $2v$.

In a magnetic gradient the difference in horizontal force on a particle at radial distance x outside the central orbit, compared to the force on the central orbit, is $e\beta Bnx/r$. Equating this to the horizontal force at the same position in the electric quadrupole ekx, one finds again Eq. (63). So in both planes the electric quadrupole is equivalent to a weak magnetic gradient. All the established doctrine for focusing particles in such a magnet therefore applies using the equivalent magnetic gradient defined by (63): for further discussion see [94].

The voltage to be applied to the electric quadrupoles disposed continuously round the ring with half-aperture u (horizontal) $\times v$ (vertical) is

$$V = n\frac{\beta pc}{2e}\frac{u^2+v^2}{r^2} \sim 22\ \mathrm{kV} \tag{64}$$

In practice the electrodes were not continuous in azimuth and the voltage was increased in inverse proportion to the fraction of the ring occupied by the quadrupoles. The discrete quadrupole pattern produces an alternating gradient effect which increases the focusing by a small amount, but the analogy with a continuous weak focusing magnetic ring is still very close.

7.4. Electric field correction

The magic momentum, for which the electric field has no effect on the spin motion, is correct at the centre of the aperture, where the electric field is in any case zero. At larger radii the momentum is greater than the magic one and the electric force is outwards: the $(g-2)$ frequency is reduced. At lower radii the momentum is below the magic one but the electric field is reversed and the $(g-2)$ frequency is again reduced. The combination of two linear effects makes the $(g-2)$ frequency vary parabolically across the aperture with its maximum at the centre: for the average muon, a correction must be applied.

Differentiating Eq. (32) with respect to particle momentum $p = \beta\gamma mc$ one finds

$$\frac{\Delta\omega}{\omega} = \frac{2\beta E}{B}\frac{\Delta p}{p}. \tag{65}$$

The particle momentum is determined by its equilibrium radius x_e (relative to the centre of the aperture) and the horizontal electric field by its instantaneous position x. Using

$$\frac{\Delta p}{p} = (1-n)\frac{x_e}{r}$$

and with help from (63)

$$E = kx = n\beta B(x/r)$$

one finds

$$\frac{\Delta\omega}{\omega} = 2n(1-n)\beta^2\frac{x x_e}{r^2}. \tag{66}$$

For a given particle, if the quadrupole field is perfect, with the result that the horizontal oscillations around the equilibrium orbit are sinusoidal, the time-average value of x is x_e. Indicating the average over all particles by the symbols $\langle\rangle$ the correction is

$$\frac{\Delta\omega}{\omega} = 2n(1-n)\beta^2\frac{\langle x_e^2\rangle}{r^2}. \tag{67}$$

To find the correction it is necessary to compute (or measure) $\langle x_e^2\rangle$. If the muons populate the available phase space uniformly in a rectangular aperture $\pm u$, the distribution of equilibrium orbits for $x_e > 0$ is $N(x_e) \propto (x_e - u)^2$ with a similar expression for $x_e < 0$; two parabolae meeting at a cusp in the centre of the aperture. One readily finds $\langle x_e^2\rangle = u^2/10$. With $\beta \sim 1$, the correction to be applied, increasing the observed $(g-2)$ frequency to get the true value, is

$$\Delta\omega/\omega = 0.2n(1-n)(u/r)^2. \tag{68}$$

This storage ring had horizontal half-aperture $u = 6$ cm and radius $r = 7$ m, so with $n = 0.14$ the correction was 1.7 ppm.

7.5. Pion injection

The system for injecting muons into the ring was designed to give maximum muon polarization, minimum background and as large an intensity as possible. A high value of

the longitudinal polarization can be achieved by starting with a momentum-selected pion beam, and accepting only decay muons with momenta in a narrow band just below the pion momentum. It was therefore decided to locate the primary target outside the storage ring, and guide a momentum-selected pion beam into the ring via a pulsed inflector. The pions would inevitably hit the large inflector structure after making only one turn; and the useful aperture of the inflector would be very small. The loss of intensity due to these factors could be compensated by using special beam optics to collect pions over a large solid angle and match them to the acceptance of the inflector.

The pions of 3.2 GeV/c must be brought to a point just outside the muon storage region, where they should be traveling tangentially. This can only be achieved by canceling the main magnetic field along the pion track and this was the task of the pulsed inflector. The inflector was in the form of a coaxial line in which a 10 μs pulse of peak current 300 kA produced the required field of 1.5 T between the inner and outer conductors. The metal walls were thick enough to keep this pulsed field out of the muon storage region (a small amount of leakage was observed and a correction was applied for this to the $(g-2)$ data).

The technical difficulty of this method of injection was outweighed by the increased pion flux and the high longitudinal polarization (95%) of the stored muons. This was confirmed by the large modulation of the decay electron counts. The calculated polarization direction was independent of the muon equilibrium radius; and consequently any possible asymmetric muon losses should cause no significant shift in the measured spin precession frequency.

The background was reduced considerably with respect to the previous experiment so that the electron detectors could now be located all around the ring. But it was still much larger than expected and our understanding of this effect is discussed below (Section 7).

7.6. Ring magnet

For a given momentum the maximum accuracy in ω_a is obtained by working at the highest magnetic field. The actual field of 1.47 T was chosen to meet this requirement without jeopardizing good field uniformity and corresponded to an orbit radius of 7 m. The field had to be as uniform as possible so that the $(g-2)$ frequency of all the muons would be the same. As the muons sample the field all the way round the ring, this meant that, after averaging in azimuth, the field should be independent of the radius.

The field could not be measured while the muons were stored. The magnet had to be switched off to remove the vacuum chamber and install the NMR equipment, which took a few days. Then the magnet was switched on again and the field was surveyed. To run the muons again, the procedure was reversed, which again implied turning the magnet off and on. Therefore it was essential that the field should be stable and reproducible to a few parts per million (ppm).

The desired stability was obtained in the following way: [95, 96]:

(i) The magnet was built on an isolated ring of concrete, temperature stabilized by circulating water through internal pipes.
(ii) The experiment was constructed in a building at controlled temperature.
(iii) To obtained mechanical stability, the magnet consisted of 40 separate blocks, mounted individually on the floor but not connected to each other.

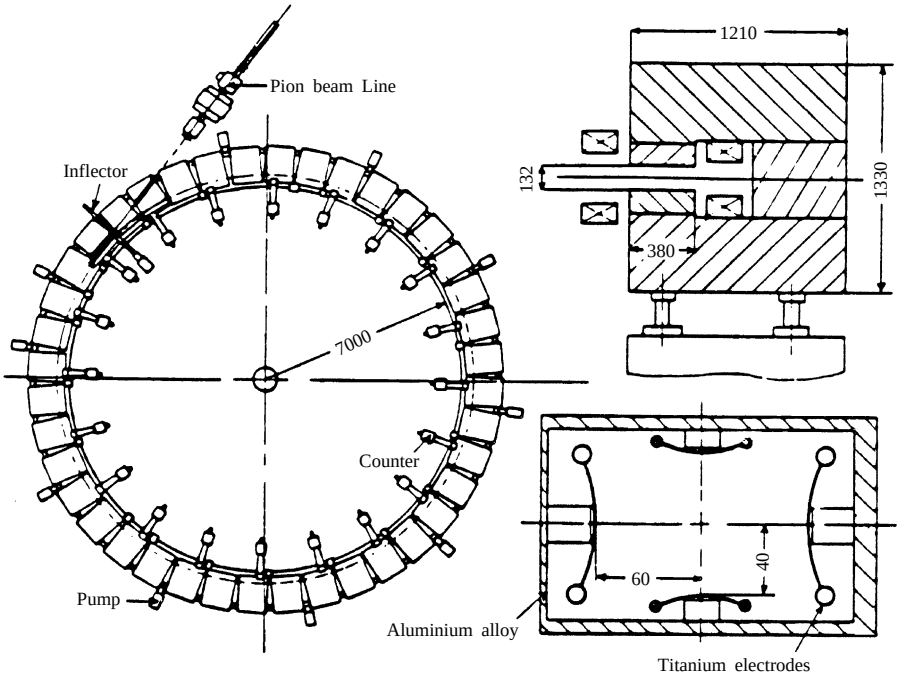

Fig. 21. The second muon storage ring, which consisted of 40 contiguous magnet blocks. The open side of the C-shaped yoke (upper right) faces the centre of the ring. The cross-section of the vacuum chamber and electric quadrupole is shown bottom right. The decay electrons are detected by 20 counters. Dimensions are in mm.

(iv) The coils did not touch the iron but were supported independently from the floor on arms that could deflect elastically to allow for thermal expansion, returning always to the same position. Most magnets emit creaks and groans when turned on, as the components slide past each other in response to magnetic forces and thermal effects. This magnet was entirely silent.

(v) The field in each of the 40 blocks was separately stabilized with reference to an NMR probe located in the median plane, radially just outside the muon storage region [97]. Error signals generated a compensating current in subsidiary coils installed in each block. Pickup coils in the feedback loop eliminated rapid field changes.

As can be seen from Fig. 21, the second muon storage ring consisted of 40 C-shaped bending magnets, each about 1 m long, fitted together to form a regular polygon with open sides facing the centre of the ring. The pole was 38 cm wide with 14 cm gap. The pole pieces were cut at an angle of 4.5° at each end so that they fitted together. However the yokes were not fitted together and consequently the field at each junction was reduced; this drop in the field, after various adjustments in the geometry of the iron of the magnet, was about 400 ppm. The magnets were energized together by four large circular coils providing continuous current all the way round the ring. The field in each magnet was separately stabilized by NMR probes mounted in the median plane, just outside the muon storage

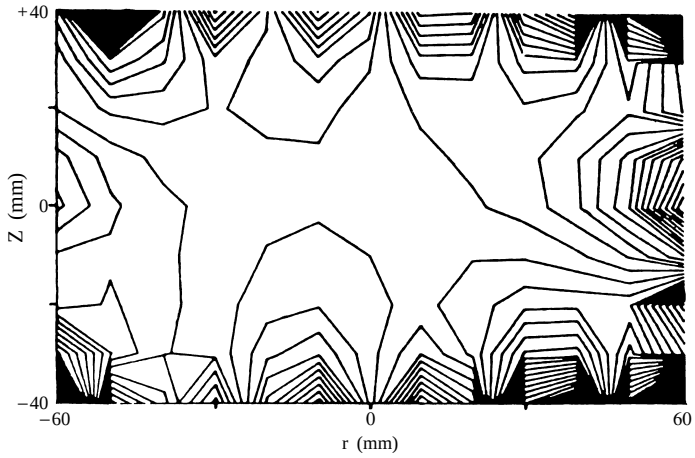

Fig. 22. A contour line plot of the magnetic field strength in the muon storage aperture. This map is obtained by averaging a three-dimensional map in azimuth. The interval between the contours is 2 ppm. The muons spend most of their time near the centre of the aperture where the field is almost uniform.

region, controlling the current through compensating coils wound around the yoke close to each pole.

To bring the magnet into the same operating condition, a special switching-on procedure was adopted; without it the field shape would have varied, and although the values at the 40 stabilizer probes were constant, temporary eddy currents or hysteresis in the yoke could modify the distribution of magnetization in the iron and the overall average field in the storage region could change by as much as 50 ppm. The procedure consisted of three rapid up and down cycles of the main current to a value some 10% higher than the operating point, followed by slow gradually decreasing oscillations of a few per cent in amplitude. This cycling was controlled automatically and took about half an hour, after which point the stabilization system switched on automatically.

Between runs the vacuum chamber was removed and the field was mapped at $\sim$250 000 points (1 cm vertical $\times$1 cm radial $\times$2 cm azimuthal). The raw proton resonance frequency must be corrected [98] for the diamagnetic shielding in water (25.6 ppm) before it can be used in Eqs. (28) and (69); see [97] for details, calibration and many precautions. A contour plot of the field across the storage region, after averaging in azimuth, is shown in Fig. 22. This was obtained by averaging the three-dimensional map in azimuth. The interval between the contours of equal field strength is 2 ppm. Repeating the procedure several months later gave almost exactly the same contour plot, as could be demonstrated by subtracting the two pictures.

During data-taking runs the field was monitored in 37 of the magnets with small NMR probes which could be driven into the muon storage ring along a radial line in the median plane without breaking the vacuum. The 400 points at which these plunging probe measurements were made were located within the coordinate system of the full field map

by survey and the relationship between the two sets of readings determined. This allowed the drift in the mean field to be followed throughout the periods between full-scale maps.

As a result of the cycling procedure and the stabilization at forty positions, the field in the storage region followed a predictable pattern; as the magnet warmed up after switching on, the average value rose by some 5 ppm over the first two days and then remained constant to within ± 1 ppm. The important consequence was that the magnet could be turned on and off and, after the warm-up period, the field averaged over the muon orbit would return to the same value within ± 1 ppm [97]; this made it possible to do the experiment with high accuracy. Further details of how this excellent result was achieved are given in [96].

It is worth emphasizing the extreme insensitivity of the average value of magnetic field $\langle B \rangle$ computed for different assumed radial distributions of muons. Even in extreme cases the average magnetic field was the same within less than 2 ppm, compared with the 160 ppm uncertainty in the previous experiment and the present statistical accuracy of $\sim$7 ppm. The $(g-2)$ frequency was essentially independent of the distribution of muons within the storage region. However, an accurate value for the mean radius of the population was needed for checking the Einstein time dilation (see below).

7.7. Electric quadrupoles and scraping

The electric quadrupole system has been described by Flegel and Krienen [99]. This quadrupole embedded in the vertical magnetic field resembles the well known Penning gauge, in which ionization of the residual gas by trapped electrons leads to an enhanced current. As a result electric breakdown in the residual gas can easily occur. It was discovered that the build-up of ionization leading to a spark usually takes some milliseconds, so the problem was minimized by turning the quadrupoles on for only $\sim$1 ms during the time the muons were to be stored. The problem was worse when μ^- were stored, as the quadrupoles were then perfect for trapping e^-: in this case the vacuum had to be better than 10^{-6} Torr.

Muon losses during the storage time can change the mean spin angle, if those that are lost have different initial spin angle from those which remain. This was not a serious error for the $(g-2)$ measurement, but for the measurement of the muon lifetime it was essential to reduce the late-time muon losses to a minimum. This was done by shifting the muon orbits at early times both vertically and horizontally in order to "scrape off" the muons which passed near the edge of the aperture and were most likely to be lost.

The orbits were shifted by applying asymmetric voltages to opposite quadrupole plates at injection time, and then gradually bringing them back to normal. This had the effect of adding a uniform electric field which moved the equilibrium orbit. While one member of a pair was pulsed normally with a 1 μs rise time, the other was fed with a 10 μs rise time. To move the orbit vertically, the bottom electrodes, all the way round the ring, received the slowly rising pulse, so the median plane of the muon orbits was initially low and returned to its normal position with the 10 μs time constant. To move the orbit horizontally, the inner electrodes on one side of the ring received the slow pulse, while on the other side the outer electrodes received the slow pulse.

The result was that the aperture of the ring was reduced both vertically and horizontally during scraping, then gradually restored to normal with a time constant of about 60 turns. This gradual change should not excite extra oscillations, so the net result was to leave a clear space of a few millimeters between the stored muons and the electrodes. Then small imperfections in the fields, leading to a slow growth of oscillation amplitudes, would not cause muons to be lost.

7.8. Radial distribution

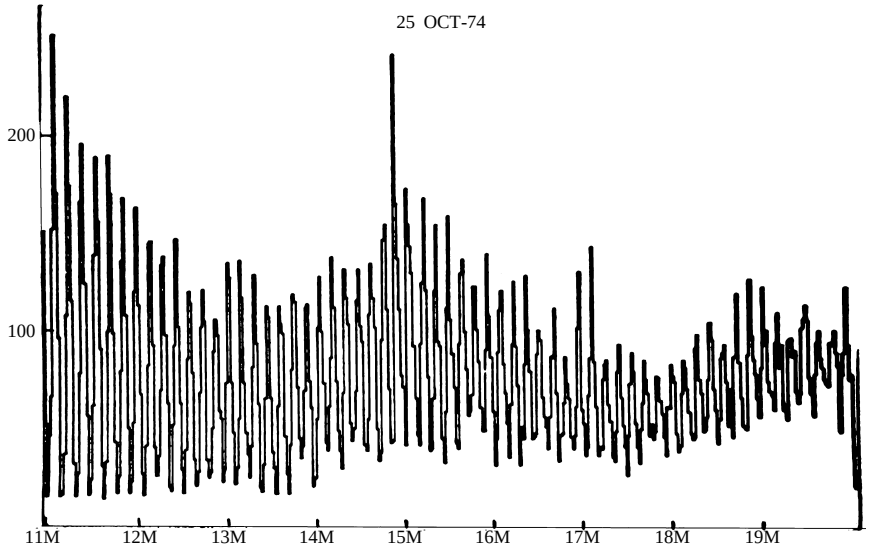

Fig. 23. Counting rate versus time showing rotation pattern and $(g-2)$ modulation (online computer output for one run). The Fourier transform of the rotation data gives the radial distribution of muons.

As before, the radial distribution of the muons is obtained by analyzing the pattern of counts at early times when the data is modulated by the rotating bunch. In the example shown in Fig. 23 one can see the rotation signal combined with the $(g-2)$ modulation. The analysis yielded Fig. 24 in which the unscraped data agrees well with the prediction and the narrowing of the distribution caused by scraping is clearly visible. The rotation frequency ω_{rot} depends on the relativistic γ factor which can be calculated directly from the measurements:

$$\gamma = 2\lambda\omega_{\text{rot}}/g\omega_p \tag{69}$$

in which ω_p is the proton frequency corresponding to the average magnetic field, $\lambda = \omega_s/\omega_p$ is given by (19) and g is of course known from this experiment to better than 1 in 10^8. Eq. (69) is used in checking the time dilation (Section 7.9).

The measurement of the radial distribution agreed with predictions assuming that the muons populated the available phase space uniformly. This confirmed the assumption

which was used to calculate the electric field correction (68) and pitch correction (44). For $n = 0.135$, $v = 4$ cm, $r = 700$ cm, the pitch correction was 0.5 ppm. The statistical error on the mean radius was typically 0.1–0.2 mm.

Fig. 25 gives the combined decay electron counts versus storage time for the whole experiment, now showing the $(g-2)$ precession out to 534 μs with a strictly exponential muon decay. The results were fitted with

$$N(t) = N_0\{L(t)\exp(-t/\tau)\,[1 - A\cos(\omega_a t + \phi)] + W\} \tag{70}$$

in which the function $L(t) = 1 + A_L\exp(-t/\tau_L)$ is an empirical correction factor to allow for muon losses and gain changes at early times, and W is late-time background. A maximum likelihood fit was made to the data by varying the five main parameters, N_0, τ, A, ω_a and ϕ together with the auxiliary parameters A_L, τ_L and W in Eq. (70).

Nine separate runs were made over a period of two years and fitted separately. As the field was determined in terms of the proton resonance frequency ω_p, the measurement of the $(g-2)$ precession frequency ω_a is expressed as the ratio $R = \omega_a/\omega_p$. The nine R-values, six for μ^+ and three for μ^-, were consistent ($\chi^2 = 7.3$ for eight degrees of freedom). The overall mean value was the essential result of the experiment:

$$R = \omega_a/\omega_p = 3.707\,213\,(27) \times 10^{-3}(7\text{ ppm}). \tag{71}$$

The error was 7.0 ppm statistical from ω_a plus 1.5 ppm from ω_p.

The corresponding value of the anomaly is given by Eq. (28) using the current result for λ, Eq. (19). The result is slightly different from that published in [92] because the value of λ has changed. Combining the data for μ^+ and μ^-,

$$a = 1\,165\,923\,(8.5) \times 10^{-9}\ (7\text{ ppm}) \tag{72}$$

in agreement with the theory.

For further details of this experiment and the precautions taken, see the final report [92] and the review article [51].

7.9. Muon lifetime in flight

Accurate measurements of the muon lifetime in a circular orbit provide a stringent test of Einstein's theory of special relativity. As a bonus it sheds light on the so-called twin paradox, gives an upper limit to the granularity of space–time and tests the CPT invariance of the weak interaction. The muon is an unstable particle, and can therefore be regarded as a clock and used to measure the time dilation predicted by special relativity. Experiments verifying the time dilation in a straight path have been made with cosmic rays and high energy accelerators. Time dilation in a circular path has always seemed more controversial.

The twin paradox was discussed in Einstein's first paper [100]. It is a paradox because, if only relative motion is important, one can ask which twin moves and which remains at rest? The difference is that to return to the same point, one twin must have suffered some acceleration which the other (older) twin did not. It seems that, according to relativity, the one with a history of acceleration finishes younger than the sessile partner; a result which is hard for the human mind to grasp. Inevitably one asks, can this be true? Perhaps some other effect comes into play, which ages the accelerated twin and makes the result

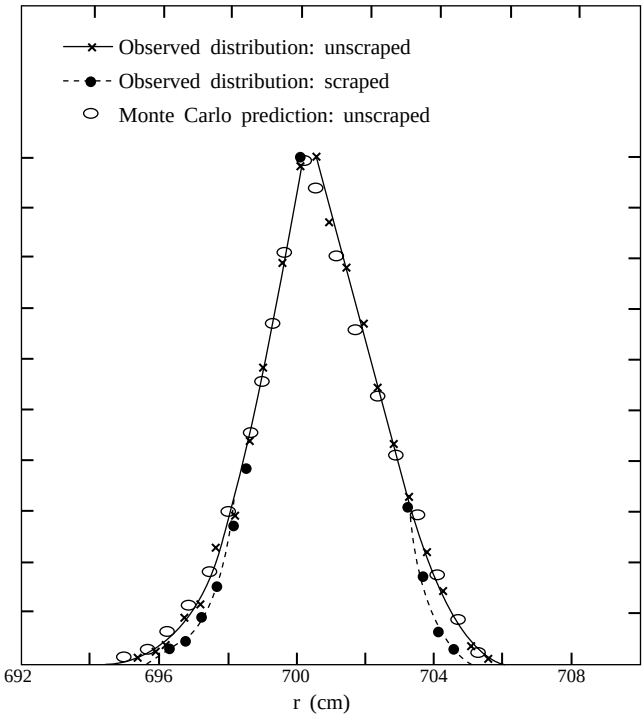

Fig. 24. The Fourier transform of the rotation data for scraped and unscraped runs, compared to prediction.

symmetric after all. We know that acceleration is destructive, and more exactly acceleration implies gravity and the gravitational red-shift in some situations offsets special relativity exactly. There are many theories. The question can only be resolved by experiment.

Hafele and Keating [101] loaded cesium atomic clocks onto a commercial aircraft on a round-the-world trip and verified the time dilation at low velocity with an accuracy of about 10%. In the CERN Muon Storage Ring, the muon performs a round trip and so when it is compared with a muon at rest the experiment mimics closely the twin paradox. The circulating muons, although they return again and again to the same place, should remain younger than their stay-at-home brothers. The stationary twin's timescale is given by the muon decay rate at rest determined in a separate experiment [102].

An accurate measurement of the muon lifetime in a circular orbit at $\gamma = 29.3$ requires high orbit stability in a short time interval (a few hundred microseconds), for any loss of muons will set a limit to the accuracy of the measurement. The reported stability was achieved by using a scraping system (Section 7.7) that shifted the muon orbits at early times in order to scrape off those muons most likely to be lost. A correction was made for the residual loss rate ($\sim$0.1% per lifetime) which was measured by a calibrated loss detector.

Fitting the decay electron counting rate (see for example Fig. 25) gave the lifetime in flight. A fit to the rotation frequency gave the radial distribution, Fig. 24, and the

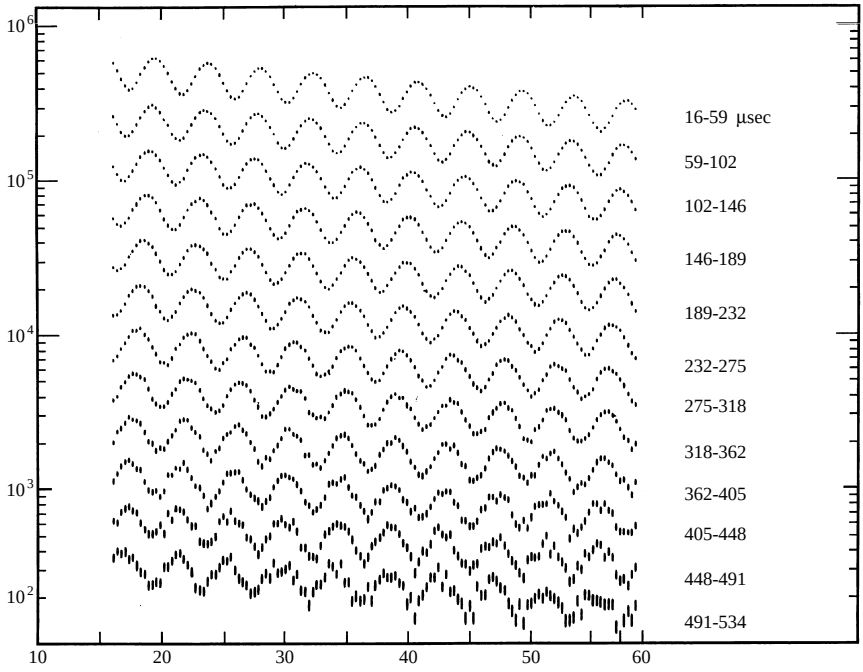

Fig. 25. The second muon storage ring: decay electron counts versus time (in microseconds) after injection. The range of time for each line is shown on the right (in microseconds).

mean value of $\gamma = 29.327$ (4) was obtained from Eq. (69). Multiplying by the lifetime [102] at rest 2.1971l (8) μs gives a predicted lifetime of 64.435 (9) μs compared to the experimental value 64.378 (26) μs. So the Einstein time dilation was verified to 0.9 ± 0.4 parts per thousand. Further details are given in [103]. The method was also used to determine the lifetime of negative muons, which cannot be measured at rest because they are captured by nuclei.

This is the best reported measurement of time dilation in a circular orbit. More accurate data is expected, but not yet available, from the Brookhaven muon storage ring to be discussed next.

8. Brookhaven muon storage ring 1984–2003

The electroweak contribution to the muon $(g - 2)$, Section 2.2, is the only experimentally accessible quantity involving loops of virtual intermediate Z and W bosons. In 1984 theorists were pressing for the measurement to be improved to check these predictions. Vernon Hughes organized a workshop at Brookhaven[1] to work out the general

[1] The main participants were J. Bailey, H.N. Brown, F. Combley, G. Danby, S. Dhawan, F.J.M. Farley, J.H. Field, P. Franzini, M. Giorgi, V.W. Hughes, J.W. Jackson, D. Joyce, F. Krienen, D. Lowenstein, W. Lysenko, W. Marciano, M. May, M. Month, P. Nath, S. Parke, G. Petrucci, E. Picasso and R. Siegel.

parameters of a new experiment and many of the collaborators in the CERN ($g - 2$) experiments participated. An improvement in accuracy by a factor 20–0.35 ppm was taken as the target, implying a 400-fold increase in the counting statistics [104]. A large part of this would come from the increased intensity of the Brookhaven AGS, compared to the CERN PS in 1975. (The CERN machine had also been upgraded, but was fully committed as an injector to the SPS and LEP.)

It was decided to use once more a storage ring with uniform magnetic field and electric focusing, working at the magic energy. The magnet aperture would be larger to give a more uniform field and the field would be surveyed inside the vacuum chamber by a moving trolley carrying 17 nuclear magnetic resonance (NMR) probes. Therefore the field could be measured at any time without switching the magnet on and off. This trolley could not be in place when the muons were stored, so to monitor the field between trolley runs about 360 fixed NMR probes were installed above and below the vacuum chamber.

To handle the large increase in counting rate, 24 separate electron calorimeters were used and the counts from each were recorded and analyzed separately. To limit the peak counting rate only one radio-frequency bunch of protons in the AGS was used at a time, but to collect statistics a new bunch was ejected every 33 ms during the flat top, thus using the whole intensity available from the accelerator. In effect, the experiment was repeated 12 times during each AGS cycle. Even so, there was some overlap of signals at early times and special techniques were developed to correct for this. Increasing the beam intensity implied a large increase in the neutron background generated at injection ("flash"); this problem was solved by injecting muons instead of pions.

The main improvements and changes in the Brookhaven experiment were as follows:

1. High proton intensity from AGS. The experiment ran with a maximum intensity of 65 TP, i.e. 6.5×10^{13} protons per AGS cycle. The particles were delivered in 12 bunches, 33 ms apart, with an AGS cycle of about 3 s.
2. Superconducting inflector and shield. The inflector needs to cancel the 1.5 T main field and could not be pulsed every 33 ms. It was operated in DC mode and an ingenious design minimized the stray field in the storage region. The small leakage field was completely eliminated by adding a superconducting shield.
3. Muon injection and fast kicker. The muon injection made effectively a factor of ten more muons available for analysis. The combination of a better capture efficiency and the reduction of the flash (permitting the detectors to be turned on earlier) both contributed to this factor. The kicker, required for muon injection, and the measurements of its eddy current are described below.
4. Muon injection and the fact that the inflector aperture did not fill the horizontal phase space gave rise to coherent betatron oscillations, i.e. motion of the beam as a whole, which needed to be included in the analysis.
5. Electrostatic focusing quadrupoles. The need to accommodate the kicker meant that the azimuthal coverage available for the quadrupoles was 1.7 times smaller than in the last CERN experiment. That meant that the electric field strength had to be 1.7 times higher for the same field focusing index. The combination of electric and magnetic fields created ideal conditions for trapping low energy electrons which multiplied rapidly leading to sparking. An ingenious design of the connecting leads intercepted these electrons and led to reliable operation.

6. A single magnet provided the 1.5 T magnetic field uniform to 1 ppm when averaged over azimuth. The variations in azimuth were at most ± 100 ppm. It is the largest diameter superconducting magnet in the world providing superb stability due to its large L/R time constant.
7. The magnetic field was measured with a moving trolley every two to three days with no need to break vacuum nor turn off the magnet. In between trolley runs, the field was monitored by some 360 fixed NMR probes located above and below the vacuum chamber.
8. Custom made, 400 MHz waveform digitizers were used to record the signal from each decay electron. This made it possible to reconstruct the time and energy spectrum of overlapping pulses, and to subtract them from the record.
9. The photomultiplier tubes were gated off during injection for periods which varied from 4 to 50 μs around the ring. After this the gain of the system was stable to better than 0.1% from early to late times. The timing stability was monitored by pulsing a laser light onto the calorimeters before and during the fill and comparing the output to a "standard" photodiode in a quiet area shielded from the beam.
10. The calorimeters were made of scintillating fibers with good light yield. Five fingers of plastic scintillator, called "front surface detectors", were fitted in front of the calorimeters and used for measuring muon losses, the vertical beam position, and other diagnostics.
11. Fiber beam monitors could be located in the muon storage region to measure the x (radial) and y (vertical) beam profile. The coherent betatron oscillations of the muons as well as the stored protons were observed for the first time using these instruments. The lifetime of the beam was reduced to half its natural value when the fiber monitors were used so they were withdrawn for the $(g-2)$ measurements.
12. The radial field was measured with a Hall probe in the centre of the muon storage region at several locations around the ring. The average radial field for most of the run was 10–20 ppm.
13. The transverse cross-section of the muon storage region was circular, which greatly reduced the need to measure the higher order multipoles of the magnetic field.

8.1. Neutron background

If protons are injected into the ring (as in the first CERN storage ring) the late background due to fast neutrons is rather serious [105]. With pion injection, used in the second muon storage ring, the situation was much improved but the background in the detectors at early times was still uncomfortably high. Considerable research was done on this at Brookhaven and it now appears that the main source is the pions which leave the ring and hit a detector on the first turn. They interact inside the detector producing fast neutrons, which have a mean free path of a few centimeters and are trapped inside the calorimeter. They gradually diffuse out of the calorimeter with a characteristic time of order 30 μs. But at any moment a neutron can be captured, the (n,γ) reaction giving a pulse of light. The overlapping of many soft gammas soon after injection gives an intense, quasi-continuous flash of light, decaying roughly as $1/t^{\eta}$ with $\eta \sim 1$. At later times the individual gamma pulses can be seen. This phenomenon, referred to for convenience as "the flash", can lead to paralysis and gain changes in the photomultipliers, interfering with the muon precession

data. Neutron gas circulating in the room is another factor but is probably less important than the neutrons which bounce around inside the detector itself.

8.2. Muon injection

It was realized that increasing the number of injected pions would increase the flash to unacceptable levels. The solution was to let the pions decay to muons outside the storage ring in a long focusing channel. The muons of slightly lower momentum than the pions could then be separated and injected into the ring. To put the muons onto permanently stored orbits requires an outward kick of order 10 mR after the particles have made about one quarter of a turn; so this is an additional complication. The kicker magnet must be pulsed with a field that ideally drops to zero before the particles come around for the second turn (150 ns), but it can contain no iron or ferrite, which would change the carefully shimmed field of the main magnet. Current sheets inside and outside the orbit were used to produce the desired pulsed field. Further details of the fast kicker are given in [106].

Direct pion injection is simpler, but not very efficient. Only about 10% of the pions decay when they are crossing the muon storage region and the yield of stored muons is only about 50 per million pions. In an external channel about 70% of the pions decay and the muons of slightly lower momentum can be trapped in the channel and matched more efficiently to the phase space of the system. This results in a factor 7 increase in the number of muons stored per pion. The useful muons are separated by momentum analysis before injection. Nevertheless about 1% of the injected particles are pions, so the flash is not eliminated completely. Overall, one gets a major increase in muon intensity and a large reduction in the background.

Injection into the successive muon storage rings can be seen to have followed a logical progression. Proton injection onto a target in the ring is technically simple, as the high momentum beam is not appreciably deflected by the magnet; but the background is huge. Pion injection, used next, requires an inflector to cancel the main field along the track of the incoming beam, so is more difficult; the background is much less, but still serious. The next logical step is to let the pions decay outside the storage ring; an inflector is again needed and in addition the muons have to be kicked onto the correct orbit after one quarter of a turn. More challenging technology, but this is the only way to have a low background with a large number of stored particles.

8.3. Kicker field and eddy currents

Eddy currents, excited in the vacuum chamber and the kicker electrodes by the fast magnetic pulse, could interfere with the measurement of $(g-2)$ precession at later times. It was important to minimize them in the design and measure them in practice. Ideally the residual eddy currents should contribute less than 0.1 ppm to the average field 20 μs after injection, when the measurements would start. Taking into account the total length of the kicker (3×1.7 m) compared to the ring circumference of 45 m, this corresponded to a 13 mG residual field in the kicker.

The OPERA 2-d transient analysis software package [107] was used to calculate the magnetic field distribution during the kicker pulse. The material of the kicker plates, their thickness and geometry were adjusted to minimize the eddy currents. With a pulse width

of 400 ns at the base, eddy currents in the top and bottom walls of the vacuum chamber reduced the pulsed field by about 20% and changed its shape. Surprisingly, the residual eddy currents were mainly in the kicker conductors themselves, rather than the walls of the vacuum chamber.

The time dependent magnetic field in the kicker was measured using the Faraday effect in a TGG crystal[2] placed between the kicker plates. The beam from an argon laser ($\lambda = 514.5$ nm) was passed through this crystal, located between almost crossed polarizers. Rotation of the plane of polarization then changed the light intensity and allowed the magnetic field to be measured. The advantage of this method is that there were no metallic parts which could change the field or carry extra eddy currents. The technique has a large dynamic range and fast response time, limited only by the rise time of the detection electronics. Further details are given in [106].

Aluminum, copper and titanium were considered for the kicker electrodes. Opposite eddy currents are excited by the rising and falling edges of the symmetric pulse of magnetic field, and should cancel exactly, except for the decay during the interval between the two transients. The ideal material to minimize the remaining eddy currents would therefore be a superconductor with infinite L/R time constant, in which case the cancellation would be exact. The inductance L is fixed by the geometry of the electrodes, vacuum chamber and the magnetic field requirements, leaving the resistance R as the only parameter that could be varied. A further constraint is that the decay electrons must pass through the kicker plates on their way to the detectors.

For the same electrode thickness copper has the least resistance, followed by aluminum and then titanium. The best metal for withstanding high voltages is titanium so it was considered first. Unfortunately, with titanium plates, 0.5 mm thick, the residual field was high and inhomogeneous, ~100 mG at 20 μs, and did not drop below 13 mG until 45 μs. Copper was considered next because of its lowest resistivity, but the 0.5 mm thick plates were found by Monte Carlo simulation to degrade the decay electrons to an unacceptable level. Fortunately with aluminum plates, 0.75 mm thick, the eddy currents were less than with titanium and dropped rapidly. They were also found to give acceptable energy resolution for the decay electrons.

Using the measured current as input, the OPERA calculation agreed with the magnetic field measured by the Faraday effect, Fig. 26, both in field shape and absolute amplitude, to better than 10%. The residual magnetic field was measured with the same system, using AC coupling to the oscilloscope with increased gain. The result, reproduced in Fig. 27, was a falling exponential with time constant about 20 μs, which contributed less than 0.1 ppm to the mean magnetic field during the measurement period.

8.4. Circular storage aperture

To calculate the muon anomalous moment one must know the field $\langle B \rangle$, averaged over the muons which contribute to the $(g-2)$ precession data. Finding this to a fraction of a

[2] A TGG crystal is an artificially grown crystal with a big Verdet constant, i.e. for the same magnetic field one gets large rotation without compromising the laser light quality. The crystal used in the tests was provided by Optics For Research, Box 82, Caldwell, NJ 07006.

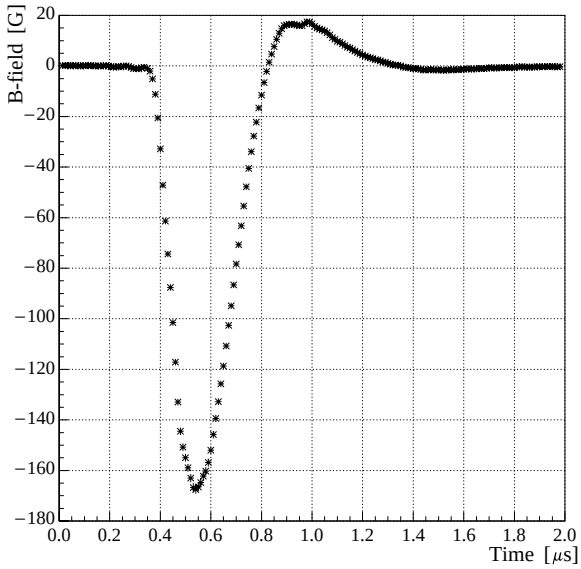

Fig. 26. The pulsed magnetic field produced by the muon kicker measured by the Faraday effect. The muons injected at peak field return 150 ns later when the field is close to zero. The kicker was fired at 95 kV, producing 4500 A in the kicker plates.

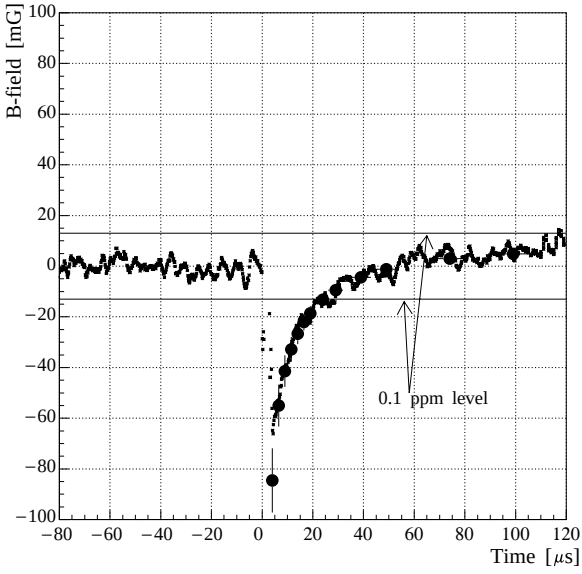

Fig. 27. The residual magnetic field produced by eddy currents, measured by the Faraday effect. The kicker was triggered at 95 kV, producing 4500 A in the kicker plates. The horizontal lines at ±13 mG show the range of ±0.1 ppm in $\langle B \rangle$. 20 μs after injection the residual field is below this limit. The filled circles correspond to OPERA calculations using the measured current pulse as input.

part per million requires special precautions. Even when averaged over azimuth, the field is unlikely to be uniform to this accuracy. So one needs to know the distribution of muons across the aperture.

Using cylindrical coordinates, tied to the centre of the storage aperture, let ϕ be the azimuth angle around the ring, z the height above the median plane and x the radius relative to the centre of the aperture. The magnetic field B satisfies the Laplace equation

$$\frac{\partial^2 B}{\partial x^2} + \frac{\partial^2 B}{\partial z^2} + \frac{1}{x + r_0}\frac{\partial B}{\partial x} + \frac{1}{(x + r_0)^2}\frac{\partial^2 B}{\partial \phi^2} = 0. \tag{73}$$

Averaging over azimuth the field seen by a muon circulating round the ring at position (x, z) in the aperture is

$$\bar{B}(x, z) = \frac{1}{2\pi}\int_0^{2\pi} B(x, z, \phi)\, \mathrm{d}\phi \tag{74}$$

and $\bar{B}(x, z)$ satisfies (73) without the last term, which cancels in integrating round the ring. Because the curvature of the ring is small it turns out that the third term in (73) is less than 1% of the first two terms, so to a good approximation the Cartesian form of the Laplace equation in two dimensions applies:

$$\frac{\partial^2 \bar{B}}{\partial x^2} + \frac{\partial^2 \bar{B}}{\partial z^2} = 0. \tag{75}$$

It is well known that the field can then be expressed as a series of multipoles, which each satisfy (75). These multipoles are most easily represented by changing to new coordinates (r, θ) in the plane of the aperture, with origin at the centre of the aperture, such that $x = r\cos\theta$ and $z = r\sin\theta$. Then

$$\bar{B} = \sum_n r^n [c_n \cos n\theta + s_n \sin n\theta], \tag{76}$$

c_n and s_n being the multipole coefficients whose values can represent any arbitrary distribution of $\bar{B}$ in the aperture plane. The overall average field is $\bar{B} = c_0$. If the other coefficients are all zero, the field is uniform and no problems arise. How large can they be before giving an appreciable error, and how does one calculate the contribution of each multipole component to $\bar{B}$?

Let the number of muons at point (r, θ) in the aperture be $M(r, \theta)$, the total number being $N = \int\int M(r, \theta) r\, \mathrm{d}r\, \mathrm{d}\theta$. Then the average field contributed by the nth cosine multipole is

$$\bar{B}_n = \frac{1}{N}\int\int c_n r^n M(r, \theta)\cos(n\theta) r\, \mathrm{d}r\, \mathrm{d}\theta = c_n I_n \tag{77}$$

where

$$I_n = \frac{1}{N}\int\int r^n M(r, \theta)\cos(n\theta) r\, \mathrm{d}r\, \mathrm{d}\theta. \tag{78}$$

Table 4
Allowable magnetic multipoles: field at the edge of the aperture in ppm for 0.1 ppm effect on $\bar{B}$

n	Rectangular	Square	Circular
2	1.12	–	2.8
4	−1.56	0.80	−50
6	−2.00	–	286
8	5.40	0.92	−1014
10	2.06	–	2768
12	25.0	0.62	6446

I_n may be called the nth moment of the muon distribution; it has no quantities associated with the magnetic field. Including all multipoles of the field, the overall average field will be

$$\bar{B} = \sum_n (c_n I_n + s_n J_n) \tag{79}$$

in which the skew moments of the muon distribution are

$$J_n = \frac{1}{N} \int \int r^n M(r, \theta) \sin(n\theta) r \, \mathrm{d}r \, \mathrm{d}\theta. \tag{80}$$

As this is a complete specification of the average field there can be no cross-terms. For calculating the average field the nth moment I_n only interacts with the nth multipole coefficient c_n. This result greatly simplifies the task of specifying the magnetic field.

Assuming that the muons populate the available phase space uniformly one can calculate the moments I_n and find the corresponding field multipoles which would change $\bar{B}$ by say 0.1 ppm. The results are given in Table 4 for various storage ring cross-sections: a rectangular aperture 10×8 cm^2, an aperture 9.14 cm^2, and a circular aperture of diameter 11 cm. All three have the same acceptance. The permissible multipole is expressed as the corresponding field at the edge of the aperture in ppm.

One sees that the aperture of the storage ring imposes its shape on the muon distribution. With a rectangular aperture, there are particles near the corners, so the moments with $n = 4, 6, 8$ have appreciable values and the corresponding multipoles must be small. A square aperture is even more sensitive to the higher multipoles 8, 12 etc. With a circular aperture, however, the smoothness of the boundary means that the higher cosine terms in the muon distribution are small, and one can tolerate much larger multipoles in the field. Therefore circular limiting stops were installed in the storage region to define the muon population.

8.5. *Electrostatic quadrupoles*

In the CERN experiment the quadrupole electrodes occupied 72% of the total circumference. There was a gap at the location of the inflector magnet, which cancels the magnetic field for the incoming beam and another gap on the opposite side of the ring to preserve the lattice symmetry. The Brookhaven lattice, shown in Fig. 28, had four quadrupole regions. Muon injection requires a kicker magnet which kicks the beam onto

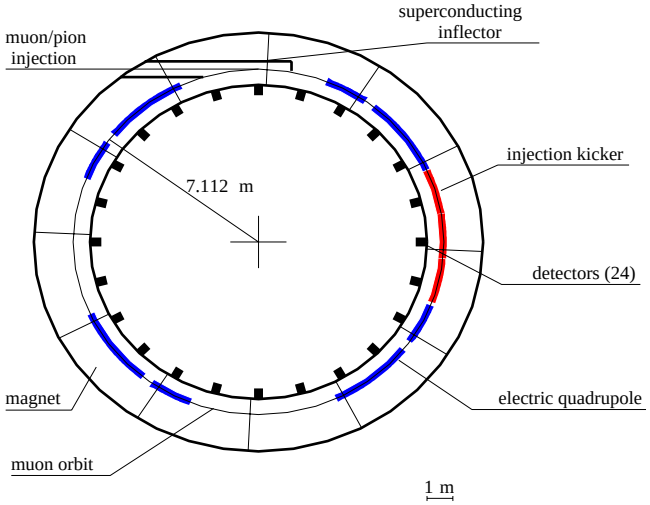

Fig. 28. The muon $g-2$ ring lattice indicating the four quadrupole regions, the kicker region and the inflector location. The muon storage region is a torus of radius $R_0 = 7112$ mm with circular cross-section of diameter 90 mm. The inner ring of 24 detectors are shown as black squares.

a stable trajectory [106]. The kicker magnet must be about 90° from the inflector magnet. Therefore space must be left for both the inflector and kicker magnets with two other gaps at 180° and 270° to preserve the lattice symmetry. The electrodes occupy only 43% of the total circumference for the BNL lattice. The electric field gradient must be 1.7 times greater than the CERN design for the same average field index. However, the higher symmetry has two beneficial results: the beta functions are much more uniform around the azimuth and the orbit stability is better.

To apply a field gradient 1.7 times greater than that used in the CERN ring was very demanding. The main difficulty is the combination of the electric and magnetic fields which creates large regions where low energy electrons can be trapped (as in Penning traps). These trapped electrons undergo oscillations [108] ionizing the residual gas and creating more trapped electrons. This cumulative action leads to a gas discharge and high voltage breakdown. In CERN the problem was solved by turning off the voltage on the plates after 800 μs before the sparks occurred if the vacuum pressure was more than 10^{-6} Torr. With the higher fields needed at Brookhaven the vacuum would have to have been better than 10^{-7} Torr, implying expensive equipment and long pumping times.

The problem was solved by studying the motion of the trapped electrons in greater detail. The electrons oscillate vertically and drift along the length of the quadrupole plates in the direction $\vec{E} \times \vec{B}$. At the end of the plates the electric field is such that the trapped electrons turn around and return to the quadrupole region. But this can be avoided by correctly designing the geometry of the high voltage connections at the end of the plates. The connections are arranged so that the quadrupole field is rotated by $\sim$45°, breaking the symmetry which is responsible for electron trapping. When the electrons reach this region they are mostly driven away from the quadrupole plates instead of returning back. They

drift along the leads and eventually reach the high voltage feed-through region, where the magnetic field is low, and they are lost on the walls of the vacuum chamber. Once the electron trapping was quenched, high DC voltages could be applied to the plates without sparking.

The vertical motion of the electrons trapped inside the quadrupoles is simple-harmonic and the frequency of oscillation is independent of amplitude; all the trapped electrons oscillate at the same frequency. This oscillation caused image charges in the top and bottom quadrupole plates which were sensed by capacitively coupling the plates to a spectrum analyzer. One expects that on average the induced charge should be zero because there should be equal number of charges moving upwards and downwards. But due to statistical fluctuations the cancellation is not exact and there is a small residual signal which showed up as a resonance at the vertical oscillation frequency. Plotting the resonance frequency versus the applied high voltage showed that the electric field followed the correct functional form even with high applied voltages [108]. That means that the trapped charge inside the quadrupole region did not change the quality of the electric field at any relevant level.

Sensitive NMR probes were used to observe any magnetic field that might be generated by the circulating trapped charges. The high voltage on the quadrupole plates was turned on and off with a $\sim$100 ms period. The change recorded by the NMR probes was less than 0.01 ppm. The new quadrupole design gave reliable operation at both muon polarities at pressures below 10^{-6} Torr, the negative being the more demanding due to the larger trapping regions.

8.5.1. Electrode design

The equipotential lines for a quadrupole potential lie on hyperbolae. Therefore, the electrodes should ideally have a hyperbolic shape. In a real design, however, the limited extent of the electrodes and the vacuum chamber walls at ground potential produce higher order multipoles. The Brookhaven electrode design is shown in Fig. 29. Flat electrodes have higher normal multipoles b_6, b_{10}, but the width of the electrode can be adjusted so that b_6 is zero. Then the field due to the b_{10} term is $\approx$1.9% of the main electric field at the edge of the aperture. For the same applied voltage the quadrupole component for the flat plate geometry is $\sim$4% higher.

The flat plate design, Fig. 29, was adopted as these electrodes would be easier to fabricate and align than hyperbolic electrodes, which would be curved in two directions. The effects of the vacuum chamber walls were minimized by the diagonal rails which have the correct fourfold symmetry. The NMR trolley (Section 8.8) uses these rails to travel around the ring.

8.6. Superconducting inflector

As in the second muon storage ring, the injected particles (pions or muons) must be brought to a point just outside the storage region where they must be traveling more or less tangentially to the orbit. This requires the incoming track to be shielded from the magnetic field by an “inflector”. In CERN the inflector was a pulsed coaxial line with solid metal walls, so leakage of magnetic field into the muon storage region was negligible. In the new experiment the magnet was wider and it was desired to inject the particles from each

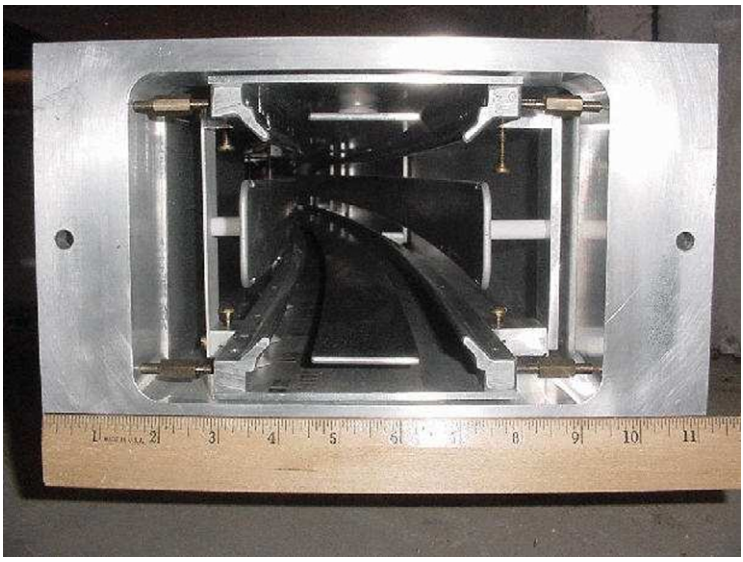

Fig. 29. A photograph of a vacuum chamber housing the quadrupole plates; the ring centre is on the left. The distance between quadrupole plates is 10 cm. The NMR trolley rides on the bottom left and the top right rails when measuring the magnetic field. The other two rails are to maintain the symmetry of the quadrupoles. The ruler units are inches.

circulating bunch in the AGS, once every 33 ms. This implied a longer inflector and to pulse it so rapidly would be very difficult. The problem was solved by using an ingenious arrangement of superconductors [109] which produced a uniform field of 1.5 T along the beam (to cancel the field of the magnet), but zero field in the neighboring muon storage region. The principle is as follows.

A cylinder with cosine theta winding produces a uniform field inside and a pure dipole field outside. If a larger cylinder is placed outside, with another cosine winding carrying an equal and opposite current, the exterior fields will cancel everywhere, but there will be a net uniform field inside the smaller cylinder Fig. 30(a). All the fringing field from the inner cylinder is confined inside the outer. One can then add a uniform current sheet along the line AB to satisfy the boundary conditions so the field to the right is unchanged but the field to the left is zero. Similarly one can add a non-uniform current sheet along the curved field line BCDA. Removing unwanted parts, one is left with Fig. 30(b). This has three current sheets which can be made of superconductor carrying a steady current. There is a uniform field to the right of the line AB where the injected particles must pass, and no stray field in the region to the left of the line AB where the muons will be stored.

If this inflector was infinitely long it would probably work perfectly. It must end where the muons come out into the magnet, and at the end there is inevitably some leakage of the inside field into the muon storage region. This was eliminated by adding a vertical superconducting sheet between the inflector and the storage region with a special switching on procedure. One must first turn on the main magnet; then cool the superconducting sheet, so that it freezes the existing uniform field pattern; then turn on the current in the inflector

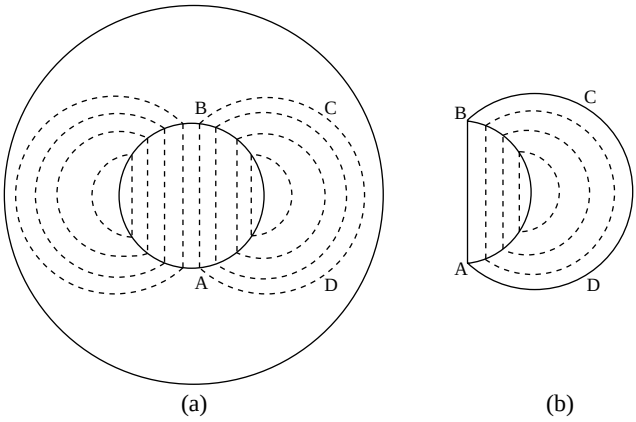

Fig. 30. Superconducting inflector concept: solid lines are current sheets, dotted lines are lines of magnetic field. Current flows into and out of the paper. a: concentric cylinders with equal and opposite cosine-theta current distributions. The field inside the inner cylinder is uniform, but beyond the outer cylinder the fields cancel. b: the same with current sheets added along field lines ABCD to satisfy the boundary conditions and the rest removed. The uniform field to the right of current sheet AB cancels the field of the main magnet along the track of the incoming muons. But the field to the left of AB, where the muons will be stored, is unchanged.

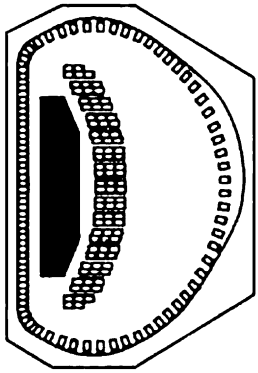

Fig. 31. A cross-section of the inflector showing superconducting windings embedded in epoxy matrix. The injected muons travel in the black area. The muon storage area is on the left.

to cancel the field along the incoming muon track. The superconducting sheet will then prevent any stray field from the inflector passing across it, into the storage region. Once this superconducting sheet had been added (for the 2000 data-taking run), there was no detectable change in the storage region whether the inflector was on or off! For earlier runs the shield was imperfect and local Field gradients made NMR measurements close to the inflector difficult.

A cross-section of the inflector is shown in Fig. 31. Further details of the construction and performance are given in [110].

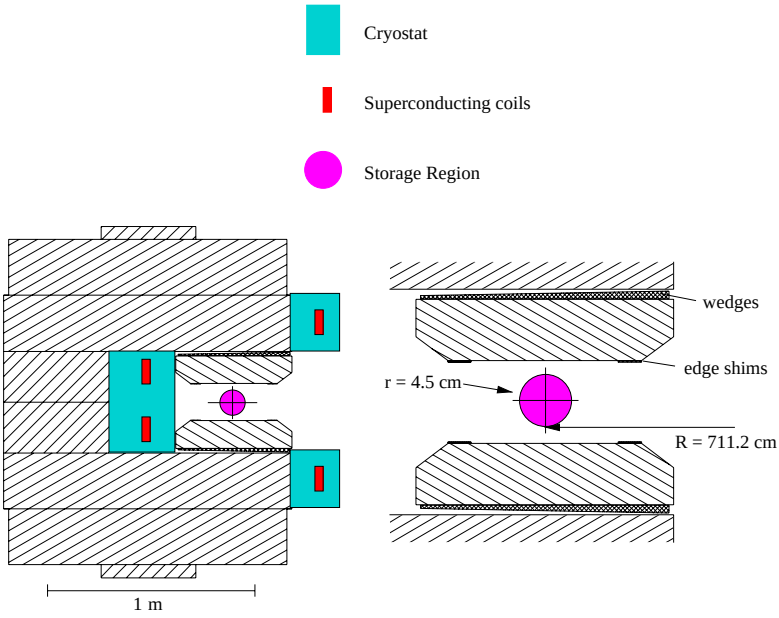

Fig. 32. The cross-section of the magnet.

8.7. Magnet with superconducting coils, shimming technique

The magnet for the BNL muon storage ring [111, 112] is a single iron magnet 14 m in diameter, with superconducting coils, constituting the largest diameter superconducting magnet in the world to date and weighing more than 700 tons. The advantages of a superconducting magnet were the large L/R time constant of the coils, with $L = 0.4$ H, and $R = 11.5\ \mu\Omega$, which meant small ripple currents, thermal stability once cold, low voltage power supply requirement. Since the diameter of the coils was large, they had to be wound at BNL and an elaborate coil support system was designed to ensure coil stability during manipulation. At full field the critical temperature of the outer coil was 6.0 K and the magnet was typically operated at 5.0 K. The stored energy at the full field of 1.5 T was 6 MJ. The quench protection system, designed to protect the coils in the event of a quench, opened the connection to the power supply, so the current flowed through a dump resistor of about 8.5 mΩ. The magnet never quenched by itself but it did so several times owing to operator mistakes or power surge.

The cross-section of the magnet, Fig. 32, shows the iron yoke, the three superconducting coils, the pole pieces, and the muon storage region, edge shims (to adjust the sextupole terms) and the wedge shims (to adjust the quadrupole and octupole terms). The pole pieces are made of high quality ultralow-carbon steel and the air gap between the pole pieces and the iron yoke isolates the storage region from the imperfections of the yoke. To further improve the field uniformity, surface coils were located on the pole pieces. After integrating in azimuth the final field uniformity in the storage region was $\sim$1 ppm.

The $(g-2)$ magnet was placed in the old 8 ft bubble chamber building at BNL, where only a heating system is installed without air conditioning. The day/night temperature change of the room was 1–2 °C, but ten times smaller for the magnet itself, owing to its large heat capacity. This temperature change caused a change in the dipole field of 35 ppm/°C while the rate of temperature change caused a change of 25 ppm/°C/h in the normal quadrupole component and 6 ppm/°C/h in the skew quadrupole component of the field. After the magnet was thermally insulated the temperature stability improved by about an order of magnitude with a corresponding gain in the field stability.

8.8. Field measurement by nuclear magnetic resonance (NMR)

The magnetic field $\vec{B}$ was measured by finding the precession frequency of protons in water using the pulsed NMR method [113]. In a magnetic field there is a net proton magnetization $\vec{M}$ along the magnetic field. A pulse is applied to rotate $\vec{M}$ by 90° and $\vec{M}$ then precesses freely around $\vec{B}$ at the frequency ω_p. This precession induces a signal in a pickup coil wound around the sample. Beating the signal with a fixed frequency (62 MHz) gives a lower frequency oscillation which can be measured by standard techniques.

The magnetic field in the muon storage region was measured every two to three days inside the vacuum chamber with an NMR trolley carrying 17 NMR probes. Between trolley runs the field was monitored continuously by 360 fixed NMR probes located on top and bottom of the vacuum chambers as illustrated in Fig. 33. The trolley was parked in a garage under vacuum and its operation was performed by remote controls. About 5000 measurements were taken around the circumference per trolley run. Inside the trolley the air pressure is kept at 1 atm and there were pressure sensors as well as temperature sensors that monitor these important parameters as a function of time. The absolute value of the magnetic field was obtained by comparing the trolley probes to a standard probe [113] with a carefully constructed spherical water sample that fills a 1 cm^3 volume. The diamagnetic shielding factor σ is given by

$$B_p = (1-\sigma)B_{\text{spherical water}} \tag{81}$$

and has been measured in separate experiments [98] with input from theory [114, 115] yielding $\sigma = 25.790(14)\times 10^{-6}$ at 34.7 °C. The temperature dependence of σ is measured to be $10.36(30)\times 10^{-9}/°\text{C}$ [116].

Table 5
Systematic uncertainties in ω_p [117]

Source of error	Size (ppm)
Absolute calibration of standard probe	0.05
Calibration of trolley probe	0.15
Trolley measurements of B-field	0.10
Interpolation with fixed probes	0.10
Uncertainty from muon distribution	0.03
Others	0.10
Total	0.24

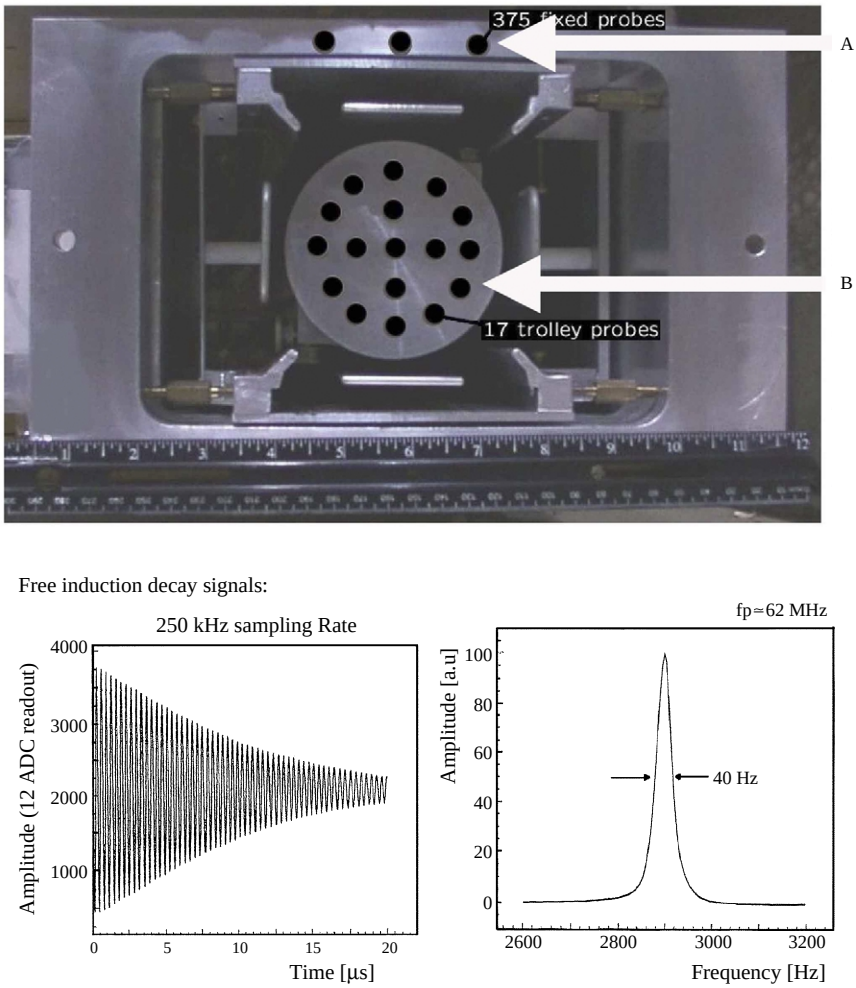

Fig. 33. The trolley carrying NMR probes traveling round the ring inside the vacuum. The locations of the 17 trolley probes are shown by black circles B, and for example the locations of fixed probes outside the vacuum chamber at A. The lower graphs show a typical free induction decay signal after beating with the fixed frequency of 62 MHz (left) and its Fourier transform (right).

The field, averaged over the muon distribution and weighted according to the number of decay electrons recorded at each moment of the run, was obtained by two largely independent analyses. A map of the magnetic field integrated over azimuth for one trolley runout out of 22 taken in 2000 is shown in Fig. 34; the central field was 1.451 274 T. The azimuthal variation of the field is also shown in Fig. 34. The final average proton resonance frequency was $\omega_p/(2\pi) = 61\,791\,595\ (15)$ Hz for the 2000 run. The systematic errors in ω_p are given in Table 5. The total systematic uncertainty in ω_p was 0.24 ppm [117].

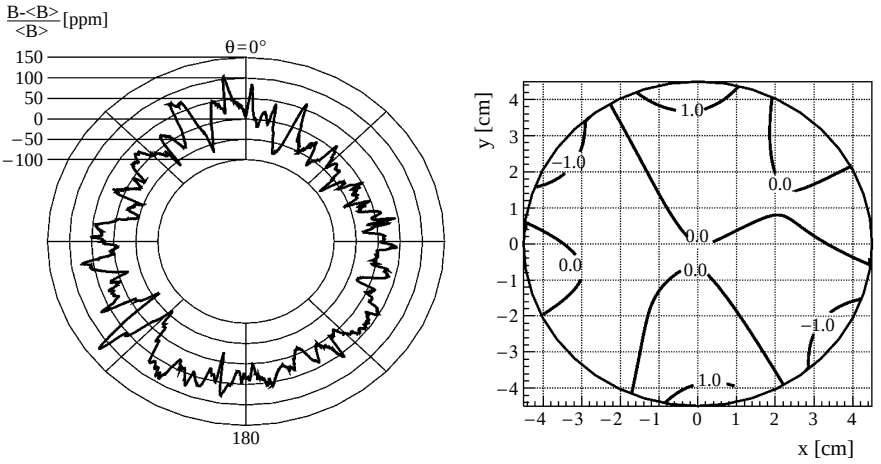

Fig. 34. Left: variation of field around the ring. Right: field contours across the aperture after integrating in azimuth.

8.9. Beam dynamics

8.9.1. Radial distribution of stored muons

The injected muon beam had a width of order 30 ns (standard deviation) and it debunched, due to momentum dispersion, with a lifetime of ≈25 μs. The time spectrum of the positrons detected by a single detector shortly after injection is shown in Fig. 35 where the $g-2$ oscillation along with the slowly decaying fast rotation structure is seen. The rotation frequency of the stored muons depends on their radius. Therefore their radial distribution can be found by Fourier analysis of the counting record. The momentum acceptance of the ring was narrow (0.6% total) and a special Fourier analysis technique was required to avoid introducing artificial effects into the width of the Fourier analyzed data. The muon radial distribution so obtained is shown in Fig. 36.

First the time distribution is divided by the ideal five parameter function which removes the muon lifetime and $(g-2)$ precession. The remaining structure in the data is the ∼149 ns revolution frequency ("fast rotation"). For a specific detector the signal in the time domain starts abruptly at $t = t_0$ and has a maximum at this time. At any other time the phases are mixed resulting in a lower amplitude signal. The true frequency distribution is obtained by using only the cosine term of the Fourier transform, obtained by multiplying the data by the cosine of each frequency and integrating from $t = t_0$ to infinity [118]. If the data are not available from the beginning then determining the correct t_0 is crucial to avoid distorting the frequency distribution. Even then the tails of the distribution will be distorted following a parabolic function. Outside the 9 cm diameter muon storage region, the tails are fitted to a parabola which is subtracted from the signal in the entire region. Analytic calculations, verified by Monte Carlo simulations, showed that this technique recovers the correct radial distribution of the muons to good accuracy [118].

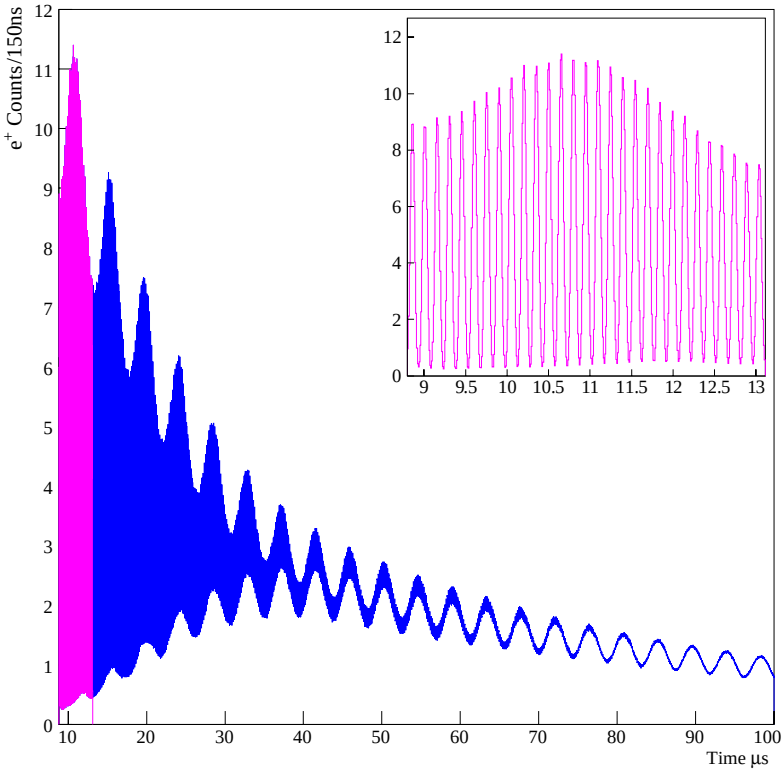

Fig. 35. The bunched structure of the muon beam, clearly evident in the inset, showing the 8.5–13 μs time range, is superimposed on the $g-2$ oscillation at early times. The fast structure decays with a lifetime of $\approx$25 μs with only the $g-2$ oscillation remaining at later times.

For fitting the $(g-2)$ frequency the fast rotation structure was eliminated by randomizing the time of the injected muon beam with the average fast rotation period of approximately 149.2 ns, the result is shown in Fig. 37. After the randomization, the Fourier spectrum showed no structure at the fast rotation frequency.

Fitting the data without the randomization showed large phase pulling in the fitted $(g-2)$ frequency, but after randomization this went away. The sensitivity to the beam rotation period used for randomization was studied and found to be very small but was included in the systematic error table.

8.9.2. Coherent betatron oscillations

The storage ring lattice is shown in Fig. 28. The muon beam was injected through the inflector (Section 8.6) [109], whose acceptance was smaller than that of the ring itself. As a result the phase space of the ring was not filled, and there were betatron oscillations of the beam as a whole, called coherent betatron oscillations (CBO). Those oscillations were

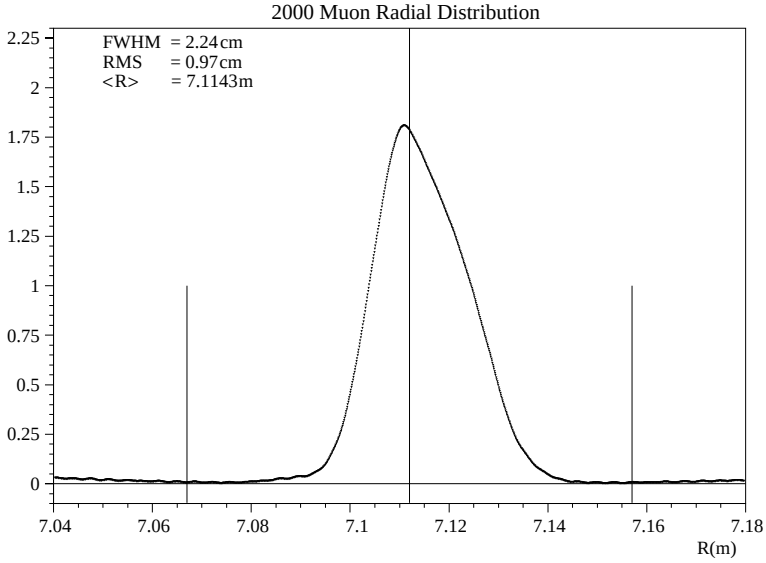

Fig. 36. The muon radial distribution obtained by Fourier analyzing the fast rotation structure of Fig. 35. The central vertical line corresponds to the centre of the muon storage region with $r_0 = 7.112$ m and the two lines on either side are the edges of the storage region at $r_0 \pm 4.5$ cm.

both horizontal and vertical and the motion is described by

$$x = x_e + x_0 \cos(\omega_x t + \theta_x), \tag{82}$$

$$y = y_0 \cos(\omega_y t + \theta_y), \tag{83}$$

Here x_e is the equilibrium radius measured from the central radius of the aperture, $r_0 = 7.112$ m, and x_0 (y_0) is the horizontal (vertical) CBO amplitude. $\omega_x \equiv 2\pi f_x$, $\omega_y \equiv 2\pi f_y$, with f_x (f_y) the horizontal (vertical) CBO frequencies given by

$$f_x = f_c(1 - \sqrt{1-n}), \tag{84}$$

and

$$f_y = f_c\sqrt{n}, \tag{85}$$

where the orbit frequency $f_c = 1/(149.2\text{ ns}) = 6.7$ MHz, and n is the field focusing index. The horizontal CBO frequency was the result of the beat between the orbit frequency $f_c = 6.7$ MHz and the horizontal betatron frequency of $f_c\sqrt{1-n}$. Small corrections were applied for the discrete nature of the quadrupole lattice. Since the acceptance of the detectors depended on the radial position of the beam, the number of the detected electrons was modulated at frequency f_x. The acceptance of detectors to the inward and outward going electrons also depended on the radial position of the beam so the $(g-2)$ asymmetry and the phase were also modulated at f_x. Since the beat frequency f_x was close to twice the $(g-2)$ frequency it was important to study the CBO and its effects very carefully (see Section 8.10).

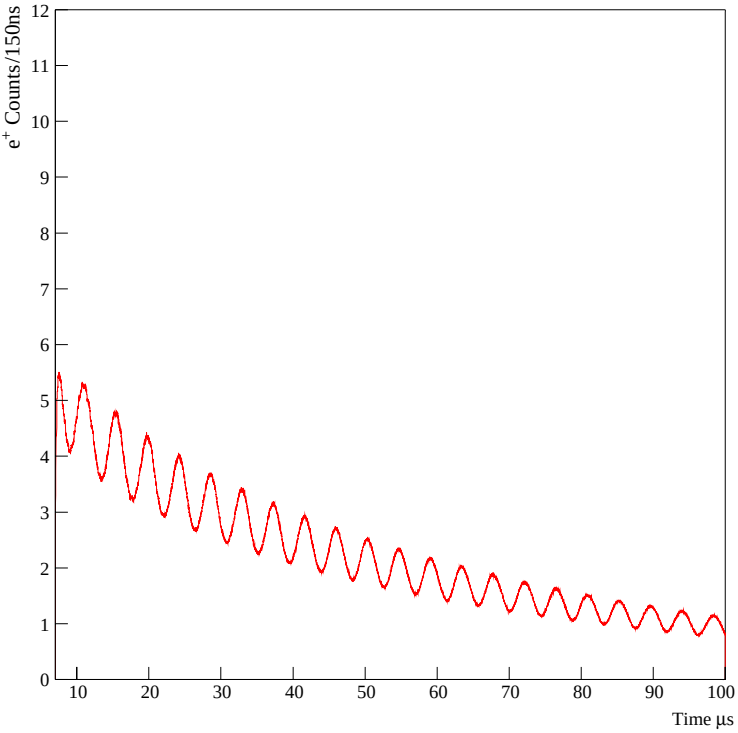

Fig. 37. The detected positron time spectrum of Fig. 35 after randomizing the muon injection time with a period of 149.2 ns; the fast rotation structure seen in Fig. 35 is eliminated.

8.9.3. Field focusing index

Fig. 38 shows the vertical $\nu_y = \sqrt{n}$ versus the horizontal $\nu_x = \sqrt{1-n}$ tune, along with the most important beam dynamics resonances of the weak focusing muon storage ring. The acceptance of a weak focusing ring has a rather wide maximum at $n = 0.137$. The n-value is proportional to the voltage applied to the quadrupole plates, Eq. (63). Due to the presence of the magnetic field, and for reasonable residual pressures in the vacuum chamber of about 10^{-7} Torr, it was difficult to work higher than $n = 0.137$ [108]. This was due to the large number of low energy trapped electrons circulating in the quadrupole region, which could accumulate and give rise to a discharge (see Section 8.5). A reasonable value of n was around 0.136–0.137, centred between two relatively strong beam dynamics resonances at $n = 0.126$ and $n = 0.148$, shown in Fig. 38. The effect of the low energy trapped electrons was studied and shown to contribute less than 0.01 ppm to the magnetic field. Their effect on the quadrupole electric field was negligible [108]. From Eq. (84) the horizontal CBO frequency corresponds to $f_x \simeq 466$ kHz which is close to twice the $(g-2)$ frequency of ≈229.1 kHz. The combination of CBO with the $(g-2)$ precession can produce a slow modulation in the counting rate on a timescale of order 100 μs. This effect is small, but shows up if the data has very high statistics.

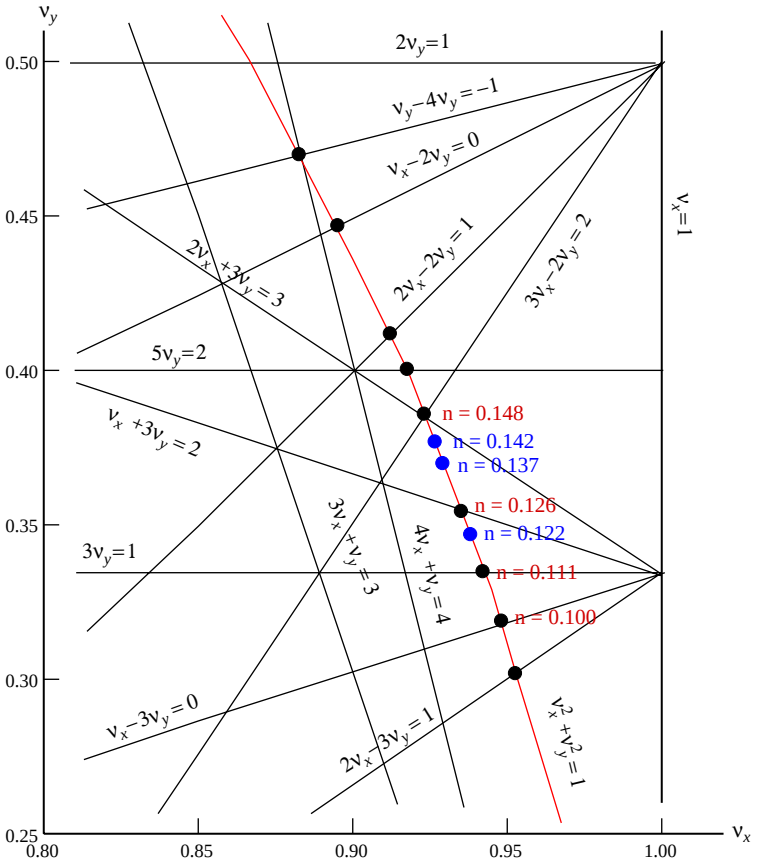

Fig. 38. The tune plane with the most important beam dynamics resonances of our weak focusing muon storage ring. The 2000 run was mostly taken at $n \simeq 0.137$, in the middle of two relatively strong resonances, at $n = 0.126$ and $n = 0.148$. The 2001 run was taken at $n = 0.142$ and $n = 0.122$.

8.10. Fitting the counting data to find ω_a

8.10.1. Signal overlap

The decay electrons have for the most part less momentum than the stored muons and under the influence of the magnetic field they spiral inwards towards the electromagnetic calorimeters [119] which give a pulse height proportional to the electron energy. The calorimeter is connected through four light guides to four photomultipliers (PMT) to reduce the counting rate per PMT. The outputs of the four PMT signals are combined into a single one which is then fed to a custom made 400 MHz waveform digitizer (WFD). The WFD consists of two WFD each of 200 MHz, interleaved so that in effect they make a single WFD with 2.5 ns channels.

Fig. 39 shows a typical digitized signal; one sees that the WFD provides information before and after the pulse over a total period of about 80 ns. To determine the time and

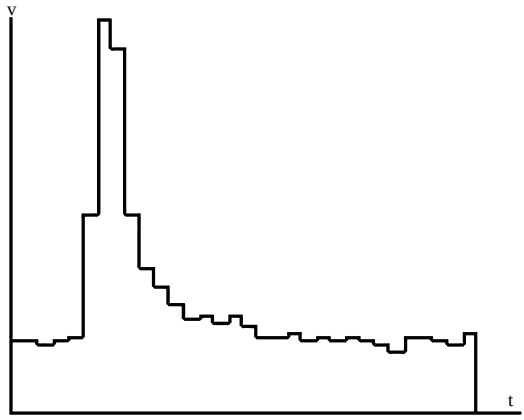

Fig. 39. The waveform digitizer record of a single pulse from the electron calorimeters. The channels are 2.5 ns wide.

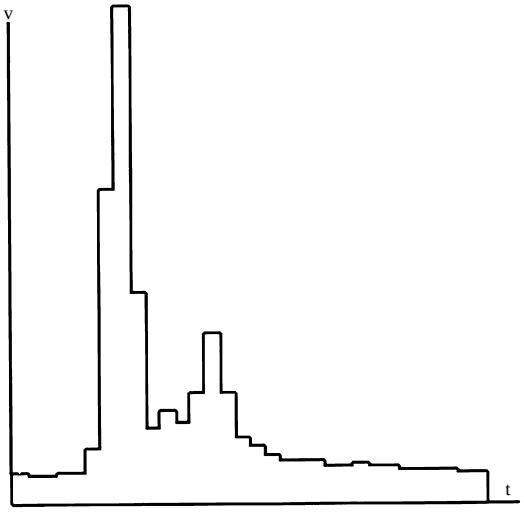

Fig. 40. The waveform digitizer record with two signals 15 ns apart. These can be fitted separately, but signals less than 5.8 ns apart are treated as one.

amplitude of the signal, each pulse is fitted with a standard shape (or template). The template was formed by averaging about 10^4 pulses recorded at late times, well after the muons were injected when there was no problem with overlap. In Fig. 40 two decay electrons are present. The first one triggered the WFD and the second one happened to arrive before the end of the digitizing period. From studies it was shown that as long as the pulses were separated by at least 5.8 ns the pulse fitting algorithm could distinguish them and recover the energy and arrival time of both. The pulses that were separated by less than 5.8 ns were treated as one, and pulses of amplitude less than 0.4 GeV were discarded.

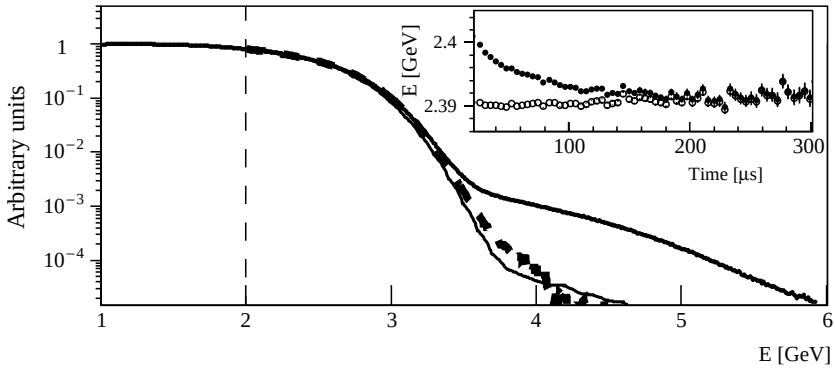

Fig. 41. The energy spectrum of the detected positrons with energy greater that 1 GeV at all times (thick line) and at only late times (thin line) when the rates are low. The dashed line shows the overlap-subtracted spectrum at early times. The inset shows the average energy of positrons before (filled circles) and after (open circles) overlap subtraction for $E > 2$ GeV (2000 data).

Due to the high counting rates, two positron pulses could overlap about 0.5% of the time. These pulses would be recorded with the wrong energy and wrong arrival time. As the overlaps occurred mainly at early times when the rates were high, this could cause a change in recorded $(g - 2)$ phase at early times leading to a shift in the fitted frequency. The following procedure was used to subtract the overlapping signals from the record.

As mentioned above, once the WFD was triggered by a signal above the energy threshold of approximately 1 GeV it was instructed to keep in its memory a digitized period of about 80 ns, more than needed to describe the trigger signal. It was thus possible for other signals above or below the energy threshold to be present during this digitized period depending on the counting rates, with a probability matching that of the unresolved overlap.

The extra recorded pulses were used to reconstruct, on a statistical basis, the time and energy spectrum of the overlap pulses which were then subtracted from the data. Given a trigger pulse, the probability of having a pulse underneath it is very close to that of a pulse 10 ns away to the right. The combination of the trigger pulse $S1$, with pulses $S2$ in a window offset to the right by $\sim$10 ns, in a time window equal to the resolution time, gives a very good account of the overlap, both in amplitude (number of random coincidences) and phase (timing of the overlapping pulses).

Two low energy pulses (singles, $S1$, $S2$) below the offline energy threshold (2.0 GeV) can combine to give one high energy pulse (double, D), above this threshold. This case constitutes a gain of an overlapping particle into the regular time spectrum. It is also possible that two single particles, both above the energy threshold, combine to make a double. This constitutes a loss of one particle from the regular time spectrum. Therefore the overlap spectrum is equal to $P = D - (S1 + S2)$ where D is the doubles spectrum and $S1$ and $S2$ are the singles.

Fig. 41 shows the electron energy spectrum [120] at early and late times and the energy spectrum at early times after overlap subtraction. The inset figure shows the average

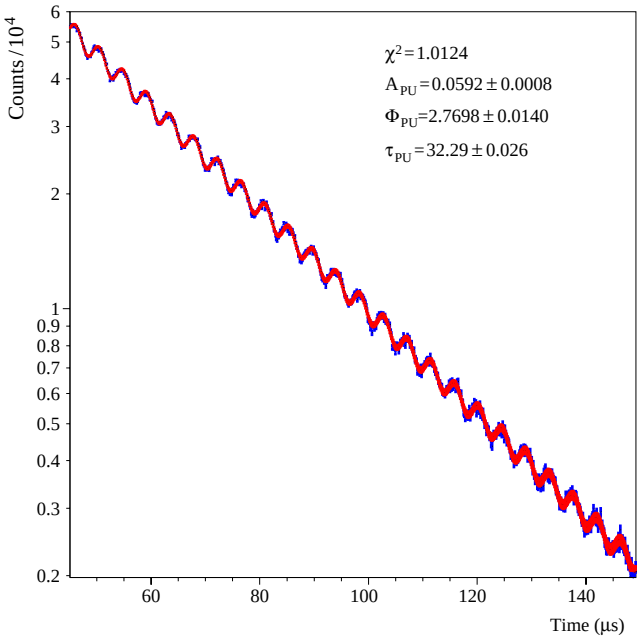

Fig. 42. The time distribution of the reconstructed overlapping signals. There is a small $(g-2)$ modulation and the lifetime is 32 μs because the overlap is proportional to rate squared. These signals have the wrong $(g-2)$ phase, so if they are not subtracted there will be a phase error at early times, leading to a wrong fitted frequency (2000 data).

electron energy before and after overlap subtraction. One sees that the overlaps are removed effectively. After overlap subtraction the average energy is essentially independent of time as expected. All this was achieved without having to resort to any fudge factors multiplying the reconstructed overlap spectrum. The only input parameter was the resolution time, determined beforehand by independent studies.

Fig. 42 shows the time spectrum of the reconstructed overlapping signals and the fit parameters. In this fit ω_a was fixed to the value obtained in the final analysis. The lifetime is equal to half the regular dilated muon lifetime as expected. The shift in ω_a due to overlap subtraction was 0.3 ppm and its systematic error due to uncertainties in the overlap phase and complications arising due to the offline energy threshold of 0.4 GeV were estimated to be 0.12 ppm [117].

8.10.2. Fitting the $(g-2)$ precession

In the year 2000, good statistics were accumulated leading to a 0.7 ppm result. Fig. 43 shows the total number of positrons detected with $E > 2$ GeV as a function of time. The $(g-2)$ precession is now seen out to 850 μs. At early times the number of positrons is of order 10 million per 149.2 ns bin. Therefore, very small effects are important and noticeable in the fits by giving a poor χ^2. The effects studied include:

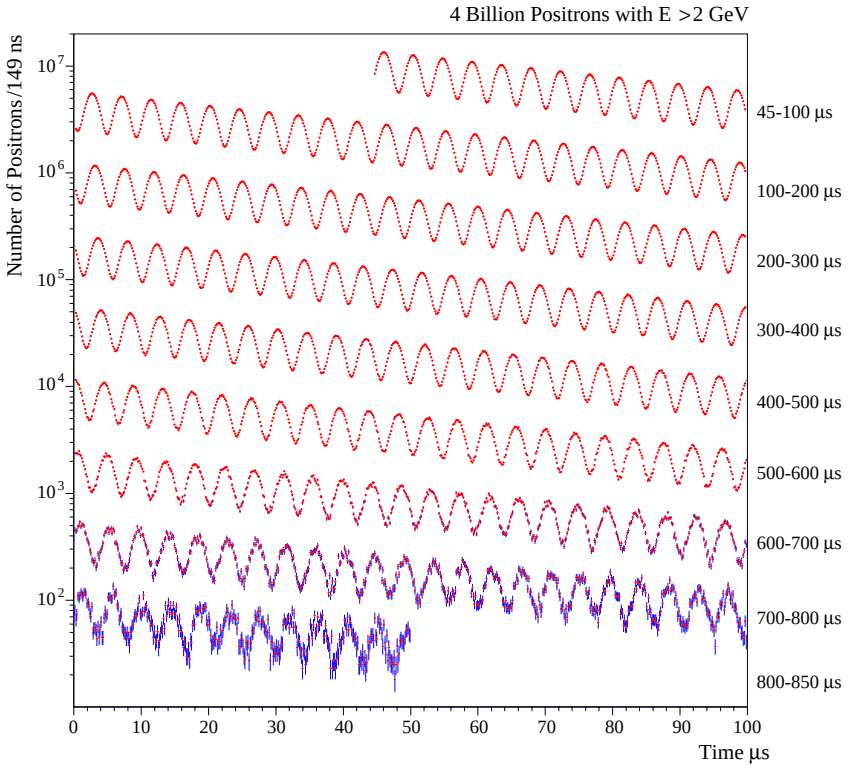

Fig. 43. The number of positrons detected with $E > 2$ GeV as a function of time (2000 data).

1. Slow varying effects as a function of time. They include detector gain changes, muon losses, early to late pulse reconstruction differences and light flash.
2. Overlapping pulses (see above).
3. Coherent betatron oscillations.
4. Unwanted particles leaking from the AGS into the muon ring (called “flashlets”).

The equation describing the ideal positron time spectrum is given by

$$N(t) = N_0(E)\mathrm{e}^{-\gamma\tau_\mu}[1 + A(E)\cos(\omega t + \phi(E))], \tag{86}$$

where $A(E)$ is the $(g-2)$ oscillation asymmetry and $\phi(E)$ the $(g-2)$ phase, both of which depend on the energy threshold E; for $E = 2$ GeV, $A = 0.4$.

After the data were fitted with Eq. (86), a Fourier analysis of the residuals gave Fig. 44. The amplitudes of the various peaks, especially that for f_{CBO}, were large relative to the white noise present in the spectrum, implying that the CBO modulation was statistically important. The two CBO sidebands were not of equal amplitude and in particular not equal to $\frac{1}{2}AA_{\mathrm{N}}$, where A_{N} is the amplitude at f_{CBO}. This precludes the possibility that N_0 was the only CBO modulated parameter. To get a good fit to the data and to be sure of finding the correct $(g-2)$ frequency, it was essential to include parameters describing the effect

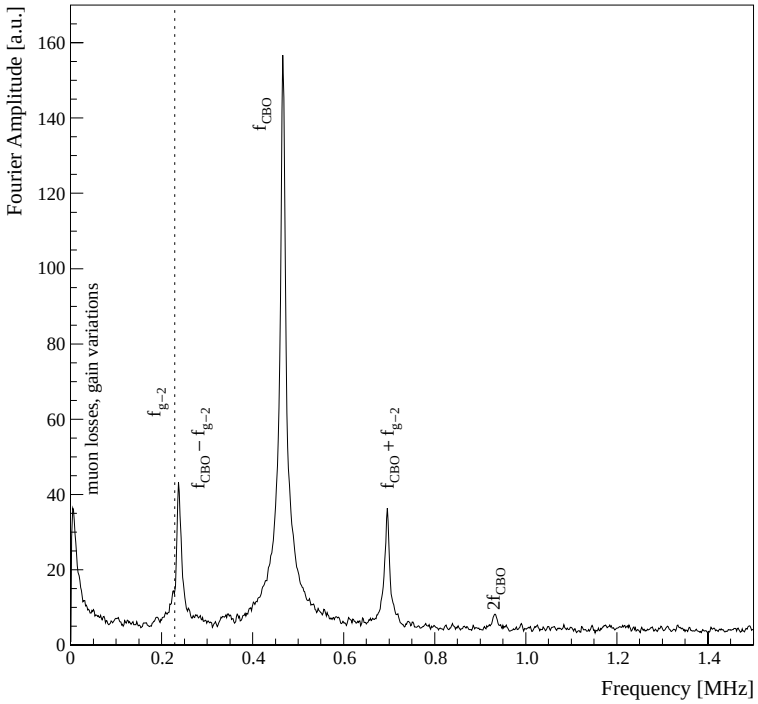

Fig. 44. Fourier analysis of the residuals to the fits to the data of Fig. 43 using Eq. (86). $f_{\mathrm{CBO}} \equiv f_x$ has a large amplitude implying that the CBO modulation is important (2000 data).

of the CBO in the fit function. Various approaches to this problem were used by different analyzers, but they came to a unanimous conclusion.

The overlapping pulses were mostly dealt with by subtracting the reconstructed overlap as described above. In a separate study the overlap spectrum was fitted keeping the overlap phase constant to a value obtained by fitting the reconstructed overlap (see above Fig. 42).

The flashlets were the result of intermittent perturbations in the AGS. They were largely eliminated by installing a pulsed dipole magnet in the pion beam line, turned on after the muons were injected into the ring. The data taken up to 1999 were checked for the flashlet background by folding the time of the pulses modulo 2.975 μs, the AGS period. Starting in 2000, once every 25 fills the electrostatic quadrupoles were not turned on, so no beam was stored. Those fills were analyzed for background effects, the most important being the flashlets; periods with problems were rejected.

Since the acceptance of the detectors depended on the position of the muon beam relative to the detectors, the time and energy spectra of the detected positrons were modulated with the CBO frequency. As a result, the $g - 2$ phase, asymmetry and the normalization N_0 were all modulated with the CBO frequency, and all became time dependent. Since the CBO frequency was close to twice the $g - 2$ frequency [117], the asymmetry and $g-2$ phase modulation were important effects that needed special attention.

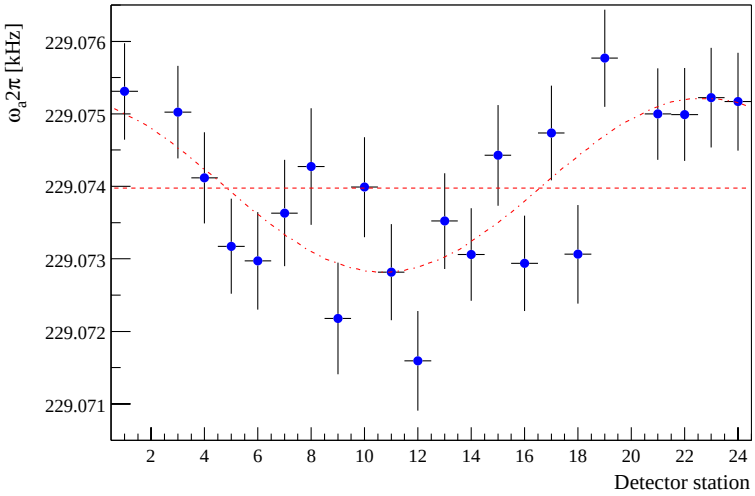

Fig. 45. A straight line fit to $\omega/2\pi$ versus detector number when only the ideal five parameter function is used to fit the positron time spectrum. The χ^2 for the straight line fit is $\chi^2 = 58.7/21$, and the average $f = 229\,073.98 \pm 0.14$ Hz. A sine wave fit (see the text) gives a good χ^2 and a central $f = 229\,074.02 \pm 0.14$ Hz, very close to the average (2000 data).

These effects generated a slow beat with an oscillation period of $\approx$130 μs. The CBO modulation affected the energy spectrum of the detected positrons and hence their average energy. However, it was difficult to distinguish it from other slow effects such as change of gain, muon losses and signal overlap. In 2001, the data were taken at different n-values, $n = 0.142$ and $n = 0.122$ corresponding to horizontal CBO frequencies of 491 kHz and 421 kHz; so the beating with the $(g-2)$ frequency of 229 kHz was more rapid and less of a problem.

The pulling of the $(g-2)$ frequency by the CBO is illustrated in Fig. 45 in which a straight line fit to $f \equiv \omega/2\pi$ versus detector gives $f = 229\,073.98 \pm 0.14$ Hz and a $\chi^2 = 58.7/21$, indicating that there is a consistency problem. A fit of a sine wave plus constant, $f + P_1 * \sin(\frac{2\pi}{24} \times \text{det.\#} + P_2)$, to the same data gave a mean value of $f = 229\,074.02 \pm 0.14$ Hz with a sine wave amplitude of (1.20 ± 0.20) Hz. When the CBO modulation is included for the parameters $N_0(t)$, $A(t)$ and $\phi(t)$, the χ^2 for a straight line fit of f versus detector, Fig. 46, is $\chi^2 = 23.9$ versus 21 expected, and the average $f = 229\,073.92 \pm 0.14$ Hz. To be acceptable, every analysis had to give a $(g-2)$ frequency that was the same for all detectors and independent of the start time of the fit. Various methods of fitting the CBO modulation and other slow effects were used and are described in references [117, 120]. All gave consistent results within the expected statistical uncertainties due to the slightly different choice of data.

The pitch correction, Eq. (44), was 0.28 ppm, determined by simulating the stored muons to find the average pitch angle. The electric field correction of 0.48 ppm, Eq. (67), was calculated from the radial distribution of muons; see Fig. 36.

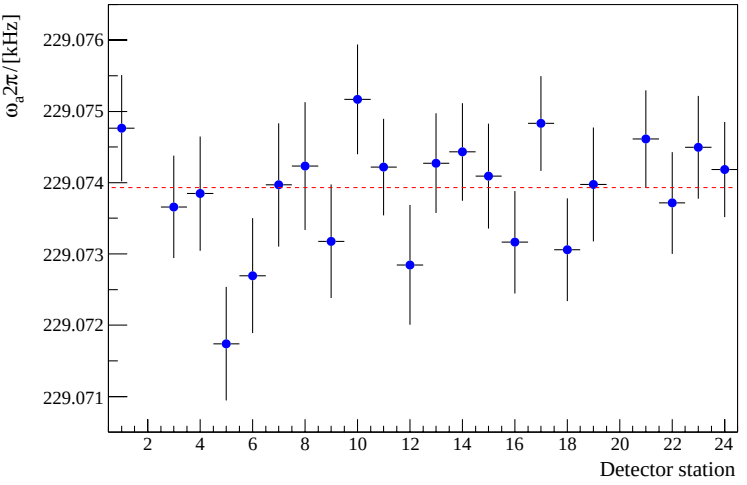

Fig. 46. A straight line fit to $\omega/2\pi$ versus detector number when the ideal five parameter function including the CBO modulations of $N_0(t)$, $A(t)$, and $\phi(t)$, is used to fit the positron time spectrum. The χ^2 for the straight line fit is $\chi^2 = 23.9$ versus 21 expected, and the average $f = 229\,073.92 \pm 0.14$ Hz (2000 data).

8.10.3. Blind analysis

To avoid subconscious bias in the analysis, arising from the theoretical value or other prejudice, the collaberation used separate teams to determine ω_a and ω_p for all reported measurements. Each team had a secret frequency offset, which was unknown to the other. The offsets were removed only after a firm value of each frequency had been assured, with all corrections applied. They then calculated the ratio ω_a/ω_p and found the value of $(g-2)$.

8.11. Results and discussion

The results of all the CERN $(g-2)$ measurements and a series of runs with the Brookhaven storage ring are shown together in Table 6. When the Brookhaven result for the 1999 data was published, the hadronic light-by-light scattering contribution to a was $-85\ (25) \times 10^{-11}$, see Section 2.4, and the experiment disagreed with theory by 3.7 ± 1.4 ppm (2.7 standard deviations), causing much fluttering in the dovecotes. Was this a "harbinger of new physics" [18] and the first clear sign of supersymmetry? Or merely a statistical fluctuation? There were many opinions. Taking the discrepancy seriously, the theorists in Marseille (Knecht, Nyffeler, Perrottet and de Rafael) resolved to re-examine the hadronic light-by-light diagrams using a new approach; and they found a positive contribution [32] to a instead of the negative value favored by the experts. Vigorous discussion ensued, but the positive value of Eq. (15) is now agreed, bringing the theory closer to experiment.

The Brookhaven result for the data of year 2000 confirmed the previous μ^+ value, but with a higher accuracy, and the result for the 2001 data on μ^- is slightly higher but agrees within one standard deviation. The average combined value, given in Table 6, is to be compared with the current theoretical number given in Table 3. The difference

Table 6
Experimental results for a

CERN cyclotron	1961	[66]	μ^+	0.001 145	(22)	
CERN cyclotron	1962	[67]	μ^+	0.001 165	(5)	
First muon storage ring at CERN	1966	[76]	μ^-	0.001 165	(3)	
First muon storage ring at CERN	1968	[77, 78]	$\mu^\pm$	0.001 166 16	(31)	
Second muon storage ring at CERN	1975–77	[92]	$\mu^\pm$	0.001 165 923	(8)	7 ppm
BNL, 1998 data	2000	[122]	μ^+	0.001 165 919 1	(59)	5 ppm
BNL, 1999 data	2001	[121]	μ^+	0.001 165 920 2	(15)	1.3 ppm
BNL, 2000 data	2002	[118]	μ^+	0.001 165 920 39	(84)	0.72 ppm
BNL, 2001 data	2004	[129]	μ^-	0.001 165 921 43	(83)	0.71 ppm
Combined weighted average		[129]	$\mu^\pm$	0.001 165 920 82	(55)	0.47 ppm

is $(28 \pm 9.6) \times 10^{-10}$, (2.9 standard deviations). It will be recalled (see Section 2.3) that the theoretical prediction is based on the cross section for hadron production in e^+e^- collisions. Revised e^+e^- data, expected from Novosibirsk, may reduce the discrepancy.

The consistency of the three recent Brookhaven results, based on independent data, is striking, and suggests that all operations were carried out correctly. We must ask whether there is any element, common to all the experiments, which could be wrong. The muon decay counts leading to ω_a are clearly independent. The magnetic field for the 2000 and 2001 data was based on new surveys with the mapping trolley and the trolley probes were recalibrated against the standard probe, so these errors are uncorrelated.

The standard probe itself was common to both runs, and was also used in the muonium hyperfine measurement which gives the value of λ, Eq. (19), used in Eq. (28). Also common to all experiments is the diamagnetic shielding for protons in water (25.6 ppm). (The NMR probe for measuring the magnetic field uses protons in water, while the value needed for the ratio λ corresponds to protons in vacuum.) The shielding correction taken from Phillips et al. [98] is another common factor, but there is no reason to doubt this value.

Some confirmation comes indeed from the muonium measurements themselves [37]. The value of λ (quoted to 31 ppb) was obtained from resonance frequencies in two different ways, only one of which involved the value of the magnetic field. The fact that they agreed implies that the magnetic field (including the diamagnetic shielding correction) was determined correctly.

Thus it is hard to explain the disagreement with theory on experimental grounds. We must hope that further progress in understanding the hadronic corrections will resolve the issue . . . or it will eventually be seen to be a consequence of some “new physics”.

9. Outlook for the future

No further runs with the present Brookhaven Storage Ring are currently programmed but there are plans to upgrade the experiment in several important respects and thus obtain more accurate data. Meanwhile the theory is being steadily refined, and further results from the e^+e^--colliding beams at Novosibirsk and Beijing can be expected to modify the calculated value.

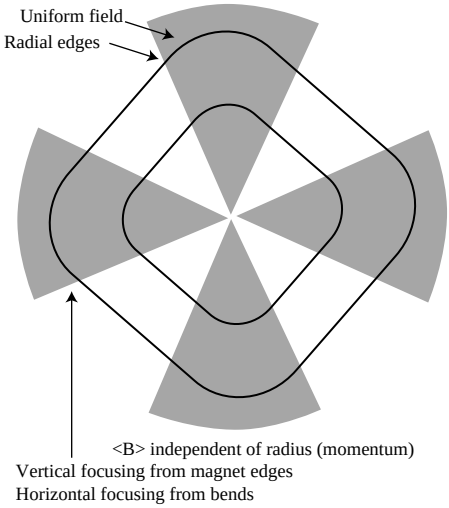

Fig. 47. A storage ring with edge focusing. The field in the magnets is uniform and the edges are radial to the centre of the ring. The mean field is independent of the orbit radius.

9.1. New ring structure

To improve the experiment further it would be desirable to increase the energy of the stored muons. This would increase the lifetime so more $(g-2)$ cycles could be measured, giving a proportional increase in accuracy for the same number of stored particles; see Eq. (56). But this would mean abandoning electric focusing, which can only be used at the magic energy of 3.1 GeV. In general, especially in strong focusing machines, magnetic focusing is associated with a field that varies with particle momentum. But for a $(g-2)$ measurement, the average magnetic field should be independent of orbit radius, as in the Brookhaven and final CERN experiments, so the muon trajectory need not be located precisely.

A new ring structure has been proposed [122] to satisfy these requirements using alternating gradient focusing. The principle, illustrated in Fig. 47, is to use several magnets with uniform field, separated by straight sections. The magnets are wedge shaped, with the edges inclined along lines which are radial to the centre of the ring. With four sectors, as shown for example in Fig. 47, this gives a quasi-square orbit with rounded corners. If the track is scaled to a different size, the proportion of time spent inside the field is invariant; so the average magnetic field is independent of the radius. On the other hand, the particles cross the magnet edges at an angle, and this gives vertical focusing.

Using standard formulae [123] the horizontal and vertical tunes, Q_h and Q_v, can be calculated as a function of the wedge angle. With only two sectors, the orbit is unstable in the horizontal plane, but with three or more sectors there are many options. By changing the wedge angle one can choose suitable combinations of Q_h and Q_v. The highest average field for a given amount of focusing is obtained with only three sectors.

Calibration of the field cannot be done with standard NMR probes carried around the ring, because they will not function in the large gradients at the magnet edges. Instead one should observe the precession of polarized protons in flight, which would automatically average the field over the orbit. If the protons have the same momentum as the muons they must follow exactly the same track. Orbit diameters can be compared to sub-millimeter accuracy by measuring the rotation frequency; see for example Fig. 36. (The small correction for the lower proton velocity can be applied with negligible error.)

Horizontally polarized protons are routinely used in the Relativistic Heavy Ion Collider at Brookhaven [124] and give an asymmetry in up/down scattering on carbon. In this case they would precess at the proton $(g-2)$ frequency, for example 126 MHz in a field of 4.5 T. As the proton lives for ever and the field would be the same for all particles, the spins will remain synchronized for over one million turns (8 ms). The frequency could rather easily be measured to parts per billion.

The proton beam has a much smaller emittance than the muons, so it can be placed at various radii, and the field (averaged in azimuth) can be mapped as a function of radius. The proton orbit could also be moved vertically by slightly tilting the magnets to add a radial magnetic field, and the protons could be injected with a range of vertical angles, to check the field as a function of vertical betatron amplitude. Locating the protons in the field is easier than locating the muons.

Calibrated in this way, the experiment would measure the ratio of muon to proton $(g-2)$ frequencies ω_a^μ/ω_a^p. To calculate the anomalous moment a_μ of the muon using Eq. (28) one needs to convert the proton $(g-2)$ frequency to the corresponding proton precession frequency at rest, that is one needs the ratio $Q = \omega_a^p/\omega_s^p = (g^p-2)/g^p$. The gyromagnetic ratio of the proton is $2 \times 2.792\,847\,39\,(6)$ [125], known to 21 ppb, so the error in Q is only 7 ppb: the conversion is no problem.

A possible structure for 15 GeV muons uses three 4.5 T magnets with bend radius of 12 m separated by straight sections 4.3 m long. The vertical tune would be $Q_v = 0.4$, slightly higher than in the storage rings used at CERN and Brookhaven, and $Q_h = 1.025$. The average field would be ≈ 3.6 T and the accuracy for the same number of stored muons would be ten times better than at present.

One of the straight sections would be used for the proton polarimeter. Another would have a conventional ferrite kicker for injecting the particles. The residual field should drop to low values after 10 μs but in any case it could be tracked with the polarized protons. As the incoming particles would not have to pass through a magnet, there would be no need for an inflector (Section 8.6).

The advantages of this new ring structure are as follows:

1. no electric quadrupoles;
2. no NMR trolley, which has to be calibrated, with corrections for the diamagnetism of water, etc;
3. no superconducting inflector;
4. injection with a simple kicker;
5. higher muon energy, giving longer lifetime, more accuracy with lower counting rates, less signal overlap and less problem with flash and detector transients;

6. higher magnetic field giving more $(g-2)$ cycles per lifetime and more accuracy—not possible with electric focusing as the electric field must be increased pro rata and is limited by breakdown.

If a higher energy muon beam is available, a new experiment might be rather simple and elegant. But as long as the theory is in doubt, the need for a more accurate measurement is debatable. When the time is ripe, this could be the path to follow.

10. Summary and concluding remarks

Since 1961 the $(g-2)$ value of the muon has been a restraint on the fantasy of theorists, a reference point against which new speculations could be compared, a landmark, a lighthouse in troubled waters; and many brilliant ideas have foundered on these rocks. The first experiments established the muon as a "heavy electron". The first muon storage ring revealed the effect of light-by-light scattering by electron loops [77, 81]; see Eq. (58). The second muon storage ring showed that virtual hadrons also contribute.

The Brookhaven experiment has stimulated the theorists to further effort, notably in the case of the hadronic light-by-light scattering diagrams [32]; see Eq. (15). On the other hand advances in the theory pushed the experimenters to find successively better ways of testing the predictions. At the time of writing the correspondence of theory with experiment is still open to doubt.

A striking feature of the results tabulated in Table 6 is that the new measurements have always fallen inside the error limits of the old. So, irrespective of the theory, the older measurements were consistently proved correct by later work! The task of the experimentalist is to create new equipment, to understand it in every detail, and to get the right result. It seems that the many teams involved in this long effort did an excellent job.

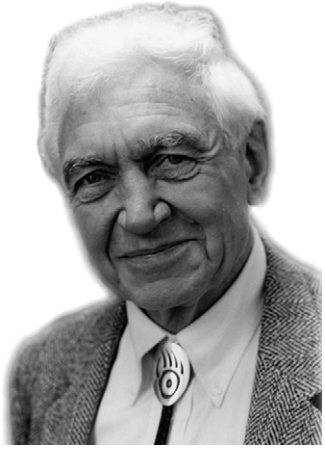

Vernon Hughes

Parts of this article are based on the review by Farley and Picasso [51] and we thank the authors and publishers for permission to reproduce.

This work was supported in part by the US Department of Energy. Finally we dedicate this article to the memory of Vernon W. Hughes. Without his vision, inspiration and determination, the Brookhaven experiment would never have been started or completed.

References

[1] S. Goudschmit, G. Uhlenbeck, Z. Phys. 35 (1926) 618.
[2] P.A.M. Dirac, Proc. Roy. Soc. 117 (1928) 610.
P.A.M. Dirac, Proc. Roy. Soc. 118 (1928) 341.
[3] H.A. Kramers, Physica 1 (1934) 825. Verh. Zeeman Jubilee (1935) 403.
[4] P. Kush, H.M. Foley, Phys. Rev. 72 (1947) 1256. Phys. Rev. 74 (1948) 250.
[5] J.S. Schwinger, Phys. Rev. 73 (1948) 416. Phys. Rev. 76 (1949) 790.
[6] T. Kinoshita, in: T. Kinoshita (Ed.), Quantum Electrodynamics, World Scientific, 1990, pp. 218–321.
[7] W.H. Louisell, R.W. Pidd, H.R. Crane, Phys. Rev. 91 (1953) 475.
A.A. Schupp, R.W. Pidd, H.R. Crane, Phys. Rev. 121 (1961) 1.
[8] V.B. Berestetskii, O.N. Krokhin, A.X. Klebnikov, Zh. Eksp. Teor. Fiz. 30 (1956) 788 [Transl. Sov. Phys. JETP 3 (1956) 791].
W.S. Cowland, Nucl. Phys. 8 (1958) 397.
[9] R.L. Garwin, L. Lederman, M. Weinrich, Phys. Rev. 105 (1957) 1415.
J.I. Friedman, V.L. Telegdi, Phys. Rev. 105 (1957) 1681.
[10] W.K.H. Panofsky, in: B. Ferretti (Ed.), Proc. 8th Int. Conf. on High Energy Physics, CERN, Geneva, 1958, p. 3.
[11] J.D. Jackson, Report CERN 77-17 (1977).
[12] P.A.M. Dirac, Proc. Roy. Soc. Al33 (1931) 60. Phys. Rev. 74 (1948) 817.
[13] K. Melnikov, Int. J. Mod. Phys. A 16 (2001) 4591.
W.J. Marciano, B.L. Roberts, (2001). Available from hep-ph/0105056.
S. Eidelman, Nucl. Phys. Proc. Suppl. B 98 (2001) 281.
E. de Rafael, Proc. XVI Rencontres de Physique de la Val D'Aoste (2002). Available from hep-ph/0208251.
S.I. Eidelman, S.G. Karshenboim, V.A. Shelyuto, Can. J. Phys. 80 (2002) 1297.
J.R. Ellis, S. Heinemeyer, K.A. Olive, G. Weiglein, J. High. Energy Phys. 301 (2003) 6.
A. Czarnecki, W.J. Marciano, A. Vainshtein, Phys. Rev. D 67 (2003) 073006.
P. Langacker, J. Phys. G. 29 (2003) 1.
L. Chatterjee, A. Sirlin, W.J. Marciano (eds.), 50 Years of Electroweak Physics: A Symposium in Honor of Professor Alberto Sirlin's 70th Birthday, J. Phys. G. 29 (2003) 1–234.
[14] T. Kinoshita, B. Nižić, Y. Okamoto, Phys. Rev. Lett. 52 (1984) 717.
T. Kinoshita, IEEE Trans. Instrum. Meas. IM-36 2 (1987) 201.
[15] T. Kinoshita, W.J. Marciano, in: T. Kinoshita (Ed.), Quantum Electrodynamics, World Scientific, 1990, pp. 419–478.
[16] T. Kinoshita, Rep. Progr. Phys. 59 (1996) 1459.
[17] V.W. Hughes, T. Kinoshita, Rev. Mod. Phys. 71 (1999) S133.
[18] A. Czarnecki, W.J. Marciano, Phys. Rev. D 64 (2001) 013014.
[19] S.J. Brodsky, J.D. Sullivan, Phys. Rev. 156 (1967) 1644.
T. Burnett, M.J. Levine, Phys. Lett. B 24 (1967) 467.
R. Jackiw, S. Weinberg, Phys. Rev. D 5 (1972) 2473.
K. Fujikawa, B.W. Lee, A.I. Sanda, Phys. Rev. D 6 (1972) 2923.
I. Bars, Y. Yoshimura, Phys. Rev. D 6 (1972) 374.
G. Altarelli, N. Cabibbo, L. Maiani, Phys. Lett. B 40 (1972) 415.
W.A. Bardeen, R. Gastmans, B.E. Lautrup, NPB 46 (1972) 315.
[20] A. Czarnecki, B. Krause, W. Marciano, Phys. Rev. Lett. 76 (1996) 3267.
A. Czarnecki, B. Krause, W. Marciano, Phys. Rev. D 52 (1995) R2619.
S. Peris, M. Perrottet, E. de Rafael, Phys. Lett. B 355 (1995) 523.
[21] T. Blum, Available from hep-lat/0212018 v2.

[22] R.R. Akhmetshin et al., Phys. Lett. B 475 (2000) 190.
R.R. Akhmetshin et al. Available from hep-ex/9904027.
R.R. Akhmetshin et al., Nucl. Phys. A 675 (2000) 424. and references therein.
[23] BES Collaboration (J.Z. Bai et al.), Phys. Lett.84 (2000) 594.
[24] KLOE Collaboration, Available from hep-ex/0307051 v2.
G. Rodrigo, H. Czyz, J.H. Kuhn, Available from hep-ph/0210287.
G. Venanzoni et al. Available from hep-ex/0210013.
[25] E.B. Dally et al., Phys. Rev. D 24 (1981) 1718.
[26] R.P. Feynman, M. Gellman, Phys. Rev. 109 (1958) 193.
[27] M. Davier, S. Eidelman, A. Hocker, Z. Zhang, Eur. Phys. J. C 27 (2003) 497.
[28] F. Jegerlehner, J. Phys. G. 29 (2003) 279.
[29] K. Hagiwara, A.D. Martin, D. Nomura, T. Teubner, Phys. Lett. B 557 (2003) 69.
[30] T. Kinoshita, B. Nižić, Y. Okamoto, Phys. Rev. D 31 (1985) 2108.
[31] B. Krause, Phys. Lett. B 390 (1997) 392.
[32] M. Knecht, A. Nyffeler, Phys. Rev. D 65 (2002) 073034.
M. Knecht, A. Nyffeler, M. Perrottet, E. de Rafael, Phys. Rev. Lett. 88 (2002) 071802.
J. High. Energy Phys. 0211 (2002) 003.
[33] M. Hayakawa, T. Kinoshita, Available from hep-ph/0112102.
[34] J.S. Schwinger, Ann. Phys. (NY) 2 (1957) 407.
[35] I.Yu. Kobzarev, L.P. Okun, Zh. Eksp. Teor. Fiz. 41 (1961) 1205 [Transl. Sov. Phys. JETP 14 (1962) 859].
[36] J. Ellis, K.A. Olive, Y. Santoso, V.C. Spanos, Available from hep-ph/0303043.
[37] W. Liu et al., Phys. Rev. Lett. 82 (1999) 711.
D.E. Groom et al., Eur. Phys. J. C15 (2000) 1.
[38] J.F. Lathrop, R.A. Lundy, V.L. Telegdi, R. Winston, D.D. Yovanovitch, Nuovo Cimento 17 (1960) 114.
S. Devons, G. Gidal, L.M. Lederman, G. Shapiro, Phys. Rev. Lett. 5 (1960) 330.
[39] L.H. Thomas, Phil. Mag. 3 (1927) 1.
[40] F.J.M. Farley, in: M. Levy (Ed.), Cargèse Lectures in Physics, Gordon and Breach 2, New York, 1968, p. 55.
F.J.M. Farley, Contemp. Phys. 16 (1975) 413.
[41] A. Sommerfeld, RC Convegno di Fisica Nucleare, Atti Reale Accad. Italia IX (1931) 137.
[42] H. Mendlowitz, K.M. Case, Phys. Rev. 97 (1955) 33.
M. Carrassi, Nuovo Cimento 7 (1958) 524.
[43] V. Bargmann, L. Michel, V.L. Telegdi, Phys. Rev. Lett. 2 (1959) 435.
[44] D.T. Wilkinson, H.R. Crane, Phys. Rev. 130 (1963) 852.
[45] J. Bailey, F.J.M. Farley, H. Jöstlein, G. Petrucci, E. Picasso, F. Wickens, Proposal for a measurement of the anomalous magnetic moment of the muon at the level of 10–20 ppm, CERN PH I/COM 69/20 (1969).
[46] G.R. Henry, J.E. Silver, Phys. Rev. 180 (1969) 1262.
[47] M. Fierz, V.L. Telegdi, in: P.G.O. Freund et al. (Eds.), Quanta, University Press, Chicago, 1970, p. 196.
[48] S. Granger, G.W. Ford, Phys. Rev. Lett. 28 (1972) 1479. Phys. Rev. D 13 (1976) 1879.
[49] F.J.M. Farley, Phys. Lett. B 42 (1972) 66.
[50] J.H. Field, G. Fiorentini, Nuovo Cimento A 21 (1974) 297.
[51] F.J.M. Farley, E. Picasso, in: T. Kinoshita (Ed.), Quantum Electrodynamics, World Scientific, 1990, pp. 479–559.
[52] P.A. Franken, S. Liebes Jr., Phys. Rev. 104 (1956) 1197.
[53] R. Karplus, N. Kroll, Phys. Rev. 77 (1950) 536.
[54] A. Petermann, Helv. Phys. Acta 30 (1957) 407. Phys. Rev. 105 (1957) 1931.
[55] C.M. Sommerfield, Phys. Rev. 107 (1957) 328.
[56] H. Suura, K. Wichmann, Phys. Rev. 105 (1957) 1930.
[57] J. Mathews, Phys. Rev. 102 (1956) 270.
A.N. Mitra, Nucl. Phys. 3 (1958) 362.
S. Hirokawa, H. Komori, Nuovo Cimento 7 (1958) 114.
[58] J. de Pagter, R.D. Sard, Phys. Rev. 118 (1960) 1353.
[59] R.P. Feynman, Proc. 12th Solvay Conf., Brussels, 1961, Interscience, New York, 1962.
[60] T.D. Lee, C.N. Yang, Phys. Rev. 104 (1956) 254.
C.S. Wu, E. Ambler, R.W. Hayward, D.D. Hoppes, R.P. Hudson, Phys. Rev. 105 (1957) 1413.

[61] C. Bouchiat, L. Michel, Phys. Rev. 106 (1957) 170.
[62] L.M. Brown, V.L. Telegdi, Nuovo Cimento 7 (1958) 698.
[63] For reviews see G. Feinberg, L. Lederman, Ann. Rev. Nucl. Sci. 13 (1963) 431.
F.J.M. Farley, Prog. Nucl. Phys. 9 (1964) 259.
[64] A.A. Schupp, R.W. Pidd, H.R. Crane, Phys. Rev. 121 (1961) 1.
[65] G.R. Henry, G. Schrank, R.A. Swanson, Nuovo Cimento A 63 (1969) 995.
[66] G. Charpak, F.J.M. Farley, R.L. Garwin, T. Muller, J.C. Sens, V.L. Telegdi, A. Zichichi, Phys. Rev. Lett. 6 (1961) 128.
G. Charpak, F.J.M. Farley, R.L. Garwin, T. Muller, J.C. Sens, A. Zichichi, Nuovo Cimento 22 (1961) 1043.
G. Charpak, F.J.M. Farley, R.L. Garwin, T. MulIer, J.C. Sens, A. Zichichi, Phys. Lett. 1 (1962) 16.
[67] G. Charpak, F.J.M. Farley, R.L. Garwin, T. Muller, J.C. Sens, A. Zichichi, Nuovo Cimento 37 (1965) 1241.
[68] G. Danby, J.M. Gaillard, K. Goulianos, L.M. Lederman, N. Mistry, M. Schwartz, J. Steinberger, Phys. Rev. Lett. 9 (1962) 36.
[69] A. Alberigi-Quaranta, M. DePretis, G. Marini, A.C. Odian, G. Stoppini, L. Tau, Phys. Rev. Lett. 9 (1962) 226.
[70] G.E. Masek, L.D. Heggie, Y.B. Kim, R.W. Williams, Phys. Rev. 122 (1961) 937.
C.Y. Kim, S. Kaneko, Y.B. Kim, G.E. Masek, R.W. Williams, Phys. Rev. 122 (1961) 1641.
A. Citron, C. Delorme, D. Fries, L. Goldzahl, J. Heintze, E.G. Michaelis, C. Richard, H. Øverås, Phys. Lett. 1 (1962) 175.
G.E. Masek, T.E. Ewart, J.P. Toutonghi, R.W. Williams, Phys. Lett. 10 (1963) 35.
[71] G. Backenstoss, B.D. Hyams, G. Knop, P.C. Marin, U. Stierlin, Phys. Rev. 129 (1963) 2759.
[72] V.W. Hughes, P.W. McColm, K. Ziock, R. Prepost, Phys. Rev. Lett. 5 (1960) 63.
[73] K. Ziock, V.W. Hughes, R. Prepost, J.M. Bailey, W.E. Cleland, Phys. Rev. Lett. 8 (1962) 103.
[74] D.P. Hutchinson, J. Menes, A.M. Patlach, G. Shapiro, Phys. Rev. 131 (1963) 1351.
[75] F.J.M. Farley, Proposed high precision $(g-2)$ experiment, CERN Intern. Rep. NP/4733 (1962).
[76] F.J.M. Farley, J. Bailey, R.C.A. Brown, M. Giesch, H. Jöstlein, S. van der Meer, E. Picasso, M. Tannenbaum, Nuovo Cimento 45 (1966) 281.
[77] J. Bailey, G. von Bochmann, R.C.A. Brown, F.J.M. Farley, H. Jöstlein, E. Picasso, R.W. Williams, Phys. Lett. B 28 (1968) 287.
[78] J. Bailey, W. Bartl, G. von Bochmann, R.C.A. Brown, F.J.M. Farley, M. Giesch, H. Jöstlein, S. van der Meer, E. Picasso, R.W. Williams, Nuovo Cimento A 9 (1972) 369.
[79] L. Michel, Proc. Phys. Soc. (London) A63 (1950) 514.
C. Bouchiat, L. Michel, Phys. Rev. 160 (1957) 170.
[80] M.A. Ruderman, Phys. Rev. Lett. 17 (1966) 794.
[81] J. Aldins, T. Kinoshita, S.J. Brodsky, A.J. Dufner, Phys. Rev. Lett. 23 (1969) 441.
J. Aldins, S.J. Brodsky, A.J. Dufner, T. Kinoshita, Phys. Rev. D 1 (1970) 2378.
[82] F.J.M. Farley, J. Bailey, E. Picasso, Nature 217 (1968) 17.
[83] W.C. Barber, B. Gittelman, G.K. O' Neill, B. Richter, Phys. Rev. Lett. 16 (1966) 1127.
[84] J.E. Augustin, J.C. Bizot, J. Buon, J. Haissinski, D. Lalanne, P. Marin, H. Nguyen Ngoc, J. Perez y Jorba, F. Rumpf, E. Silva, S. Tavernier, Phys. Lett. B 28 (1969) 508.
J.E. Augustin et al., Phys. Rev. Lett. 34 (1975) 233.
V.L. Auslander, G.I. Budker, E.V. Pakhtusova, Yu.N. Pestov, V.A. Sidorov, A.N. Skrinskij, A.G. Khabakhaser, Akad. Nauk SSR, Sibirskee Otd., Novosibirsk preprint 243 (1968).
[85] J.J. Russell, R.C. Sah, M.J. Tannenbaum, W.E. Cleland, D.G. Ryan, D.G. Stairs, Phys. Rev. Lett. 26 (1971) 46.
[86] S.J. Brodsky, S.D. Drell, Ann. Rev. Nucl. Sci. 20 (1970) 147.
E. Picasso, High Energy Physics and Nuclear Structure, Plenum, New York, 1970.
L.M. Lederman, M.J. Tannenbaum, Adv. Part. Phys. 1 (1968) 1.
F.J.M. Farley, Proc. First Int. Conf. Eur. Phys. Soc., Florence, 1969 Riv. Nuovo Cimento 1 (1969) 59.
[87] R.T. Robiscoe, Phys. Rev. 168 (1968) 4; Cargèse Lect. Phys. 2 (1968) 5.
R.T. Robiscoe, T.W. Shyn, Phys. Rev. 59 (1970) 559.
[88] T. Appelquist, S.J. Brodsky, Phys. Rev. Lett. 24 (1970) 562.
[89] A. Rich, Phys. Rev. Lett. 20 (1968) 967.
[90] J.C. Wesley, A. Rich, Phys. Rev. A 4 (1971) 1341.

[91] J. Bailey, K. Borer, F. Combley, H. Drumm, C. Eck, F.J.M. Farley, J.H. Field, W. Flegel, P.M. Hattersley, F. Krienen, F. Lange, G. Petrucci, E. Picasso, H.I. Pizer, O. Rúnolfsson, R.W. Williams, S. Wojcicki, Phys. Lett. B 55 (1975) 420.
J. Bailey, K. Borer, F. Combley, H. Drumm, C. Eck, F.J.M. Farley, J.H. Field, W. Flegel, P.M. Hattersley, F. Krienen, F. Lange, E. Picasso, W. von Rüden, Phys. Lett. B 68 (1977) 191.
[92] J. Bailey, K. Borer, F. Combley, H. Drumm, C. Eck, F.J.M. Farley, J.H. Field, W. Flegel, P.M. Hattersley, F. Krienen, F. Lange, G. Lebee, E. McMillan, G. Petrucci, E. Picasso, O. Rúnolfsson, W. von Rüden, R.W. Williams, S. Wojcicki, Nucl. Phys. B 150 (1979) 1.
[93] J. Bailey, E. Picasso, Prog. Nucl. Phys. 12 (1970) 43.
F. Combley, E. Picasso, Phys. Rep. C 14 (1974) 1.
F.J.M. Farley, Contemp. Phys. 16 (1975) 413.
J.D. Jackson, Classical Electrodynamics, Wiley, New York and London, p. 559.
[94] F. Combley, E. Picasso, Phys. Rep. C 14 (1974) 1.
[95] K. Borer, H. Drumm, C. Eck, G. Petrucci O. Rúnolfsson Proc. 5th Int. Conf. on Magnet Technology, Rome (1975) 133.
[96] H. Drumm, C. Eck, G. Petrucci, O. Rúnolfsson, Nucl. Instrum. Methods 158 (1979) 347.
[97] K. Borer, Nucl. Instrum. Methods 143 (1977) 203.
K. Borer, F. Lange, Nucl. Instrum. Methods 143 (1977) 219.
[98] W.D. Phillips et al., Metrologica 13 (1977) 179.
P.F. Winkler, D. Kleppner, T. Myint, F.G. Walther, Phys. Rev. 60 (1972) 817.
[99] W. Flegel, F. Krienen, Nucl. Instrum. Methods 143 (1973) 549.
[100] A. Einstein, Ann. der Phys. 17 (1905) 891.
[101] J.C. Hafele, R.E. Keating, Science 177 (1972) 166.
[102] M.P. Balandin, V.M. Grebenyuk, V.G. Zinov, A.D. Konin, A.N. Ponomarev, Sov. Phys. JETP 40 (1974) 811.
[103] J. Bailey, K. Borer, F. Combley, H. Drumm, F.J.M. Farley, J.H. Field, W. Flegel, P.M. Hattersley, F. Krienen, F. Lange, E. Picasso, W. von Rüden, Nature 268 (1977) 301.
[104] C. Heisey, F. Krienen, J.P. Miller, B.L. Roberts, L.R. Sulak, H.N. Brown, E.D. Courant, G.T. Danby, C.R. Gardner, J.W. Jackson, M. May, M. Month, P.A. Thompson, M.S. Lubell, W.P. Lysenko, W. Williams, J.T. Reidy, F. Combley, G. zu Putlitz, S.K. Dhawan, A.A. Disco, F.J.M. Farley, V.W. Hughes, Y. Kuang, J.K. Markey, H. Orth, H. Venkateramania, A new precision measurement of the muon $(g-2)$ value at the level of 0.35 ppm, Brookhaven AGS Proposal 821 (1985), revised (1986). Design Report for AGS 821 (1989).
[105] J.S. Carter, F.J.M. Farley, Nucl. Instrum. Methods 28 (1964) 279.
[106] E. Efstathiadis, Y.Y. Lee, J.L. Mi, C. Pai, J.M. Paley, B.L. Roberts, R.T. Sanders, Y.K. Semertzidis, D.S. Warburton, NIMA 496 (2003) 8.
[107] OPERA, Electromagnetic Fields Analysis Program, Vector Fields Ltd., 24 Bankside, Oxford OX5 1JE, England.
[108] Y.K. Semertzidis, G. Bennett, E. Efstathiadis, F. Krienen, R. Larssen, Y.Y. Lee, W.M. Morse, Y. Orlov, C.S. Ozben, B.L. Roberts, L.P. Snydstrup, D.S. Warburton, Nucl. Instrum. Methods A 503 (2003) 458.
[109] F. Krienen, D. Loomba, W. Meng, Nucl. Instrum. Methods A 283 (1989) 5.
[110] A. Yamamoto, Y. Makida, K. Tanaka, F. Krienen, B.L. Roberts, H.N. Brown, G. Bunce, G.T. Danby, M. Grosse-Perdekamp, H. Hseuh, L. Jia, Y.Y. Lee, M. Mapes, W. Meng, W. Morse, C. Pai, R. Prigl, W. Sampson, J. Sandberg, M. Suenaga, T. Tallerico, F. Toldo, K. Woodle, M.A. Green, I. Itoh, H. Otsuka, Y. Saito, T. Ozawa, Y. Tachiya, H. Tanaka, A. Grossmann, K. Jungmann, G. zu Putlitz, H. Deng, S. Dhawan, V. Hughes, D. Kawall, J. Pretz, S. Redin, E. Sichtermann, A. Steinmetz, Nucl. Instrum. Methods A 491 (2002) 23.
[111] G.T. Danby, L. Addessi, Z. Armoza, J. Benante, H.N. Brown, G. Bunce, J.C. Cottingham, J. Cullen, J. Geller, H. Hseuh, J.W. Jackson, L. Jia, S. Kochis, D. Koniczny, R. Larsen, Y.Y. Lee, M. Mapes, R.E. Meier, W. Meng, W.M. Morse, M. O'Toole, C. Pai, I. Polk, R. Prigl, Y.K. Semertzidis, R. Shutt, L. Snydstrup, A. Soukas, T. Tallerico, F. Toldo, D. von Lintig, K. Woodle, R.M. Carey, W. Earle, E.S. Hazen, F. Krienen, J.P. Miller, J. Ouyang, B.L. Roberts, L.R. Sulak, W.A. Worstell, Y. Orlov, D. Winn, A. Grossmann, K. Jungmann, G. zu Putlitz, P. von Walter, P.T. Debevec, W.J. Deninger, D.W. Hertzog, S. Sedykh, D. Urner, M.A. Green, U. Haeberlen, P. Cushman, S. Giron, J. Kindem,

D. Miller, T. Timmermans, D. Zimmerman, V.P. Druzhinin, G.V. Fedotovich, D.N. Grigorev, B.J. Khazin, N.M. Ryskulov, S. Serednyakov, Yu.M. Shatanov, E. Solodov, K. Endo, H. Hirabayashi, Y. Mizumachi, A. Yamamoto, S.K. Dhawan, A. Disco, F.J.M. Farley, X. Fei, M. Grosse-Perdekamp, V.W. Hughes, D. Kawall, S.I. Redin, Nucl. Instrum. Methods A 457 (2001) 151.

[112] S.I. Redin, N.M. Ryskulov, G.V. Fedotovich, B.I. Khazin, G.M. Bunce, G.T. Danby, J.W. Jackson, W.M. Morse, R. Prigl, Y.K. Semertzidis, E. Efstathiadis, B.L. Roberts, A. Grossmann, K. Jungmann, G. zu Putlitz, P. von Walter, S.K. Dhawan, F.J.M. Farley, M. Grosse-Perdekamp, V.W. Hughes, D. Kawall, Nucl. Instrum. Methods A 473 (2001) 260.

[113] X. Fei, V.W. Hughes, R. Prigl, Nucl. Instrum. Methods A 394 (1997) 349.

[114] W.E. Lamp Jr., Phys. Rev. 60 (1941) 817.

[115] H. Grotch, R.A. Hegstrom, Phys. Rev. A 4 (1971) 59.

[116] B.W. Petley et al., Metrologia 20 (1984) 81.

[117] G.W. Bennett, B. Bousquet, H.N. Brown, G. Bunce, R.M. Carey, P. Cushman, G.T. Danby, P.T. Debevec, M. Deile, H. Deng, W. Deninger, S.K. Dhawan, V.P. Druzhinin, L. Duong, W. Earle, E. Efstathiadis, F.J.M. Farley, G.V. Fedotovich, S. Giron, F. Gray, D. Grigoriev, M. Grosse-Perdekamp, A. Grossmann, M.F. Hare, D.W. Hertzog, X. Huang, V.W. Hughes, M. Iwasaki, K. Jungmann, D. Kawall, B.I. Khazin, J. Kindem, F. Krienen, I. Kronkvist, A. Lam, R. Larsen, Y.Y. Lee, I. Logashenko, R. McNabb, W. Meng, J. Mi, J.P. Miller, W.M. Morse, D. Nikas, C.J.G. Onderwater, Y. Orlov, C.S. Özben, J.M. Paley, Q. Peng, C.C. Polly, J. Pretz, R. Prigl, G. zu Putlitz, T. Qian, S.I. Redin, O. Rind, B.L. Roberts, N.M. Ryskulov, P. Shagin, Y.K. Semertzidis, Yu.M. Shatanov, E.P. Sichtermann, E. Solodov, M. Sossong, A. Steinmetz, L.R. Sulak, A. Trofimov, D. Urner, P. von Walter, D. Warburton, A. Yamamoto, Phys. Rev. Lett. 89 (2002) 101804.

[118] Y. Orlov, C.S. Ozben, Y.K. Semertzidis, Nucl. Instrum. Methods A 482 (2002) 767.

[119] S.A. Sedykh, J.R. Blackburn, B.D. Bunker, P.T. Debevec, F.E. Gray, D.W. Hertzog, T.D. Jones, C.J.G. Onderwater, C.C. Polly, D.C. Urner, R.M. Carey, C. Coulsey, G. de Santi, M. Hare, J.P. Miller, J. Ouyang, O. Rind, A. Trofimov, P. Cushman, S. Giron, J. Kindem, C. Timmermans, D. Zimmerman, D. Winn, V. Druzhinin, Nucl. Instrum. Methods A 455 (2000) 346.

[120] H.N. Brown, G. Bunce, R.M. Carey, P. Cushman, G.T. Danby, P.T. Debevec, M. Deile, H. Deng, W. Deninger, S.K. Dhawan, V.P. Druzhinin, L. Duong, E. Efstathiadis, F.J.M. Farley, G.V. Fedotovich, S. Giron, F. Gray, D. Grigoriev, M. Grosse-Perdekamp, A. Grossmann, M.F. Hare, D.W. Hertzog, V.W. Hughes, M. Iwasaki, K. Jungmann, D. Kawall, M. Kawamura, B.I. Khazin, J. Kindem, F. Krienen, I. Kronkvist, R. Larsen, Y.Y. Lee, I. Logashenko, R. McNabb, W. Meng, J. Mi, J.P. Miller, W.M. Morse, D. Nikas, C.J.G. Onderwater, Y. Orlov, C.S. Özben, J.M. Paley, C. Polly, J. Pretz, R. Prigl, G. zu Putlitz, S.I. Redin, O. Rind, B.L. Roberts, N. Ryskulov, S. Sedykh, Y.K. Semertzidis, Yu.M. Shatanov, E.P. Sichtermann, E. Solodov, M. Sossong, A. Steinmetz, L.R. Sulak, T. Timmermans, A. Trofimov, D. Urner, P. von Walter, D. Warburton, D. Winn, A. Yamamoto, D. Zimmerman, Phys. Rev. Lett. 86 (2001) 2227.

[121] H.N. Brown, G. Bunce, R.M. Carey, P. Cushman, G.T. Danby, P.T. Debevec, H. Deng, W. Deninger, S.K. Dhawan, V.P. Druzhinin, L. Duong, W. Earle, E. Efstathiadis, G.V. Fedotovich, F.J.M. Farley, S. Giron, F. Gray, M. Grosse-Perdekamp, A. Grossmann, U. Haeberlen, M.F. Hare, E.S. Hazen, D.W. Hertzog, V.W. Hughes, M. Iwasaki, K. Jungmann, D. Kawall, M. Kawamura, B.I. Khazin, J. Kindem, F. Krienen, I. Kronkvist, R. Larsen, Y.Y. Lee, I. Logashenko, R. McNabb, W. Meng, J. Mi, J.P. Miller, W.M. Morse, C.J.G. Onderwater, Y. Orlov, C. Ozben, C. Polly, C. Pai, J.M. Paley, J. Pretz, R. Prigl, G. zu Putlitz, S. Sedykh, Y.K. Semertzidis, Yu.M. Shatanov, E. Solodov, M. Sossong, A. Steinmetz, L.R. Sulak, T. Timmermans, A. Trofimov, D. Urner, P. von Walter, D. Warburton, D. Winn, A. Yamamoto, D. Zimmerman, Phys. Rev. D 62 (2000) 091101(R).

[122] F.J.M. Farley, Available from hep-ex/0307024, Nucl. Instrum. Methods A, (in press).

[123] John J. Livingood, Principles of Cyclic Particle Accelerators, Van Nostrand Reinhold, 1961.

[124] G. Bunce, Int. J. Mod. Phys. A 18 (2003) 1255.

[125] K. Hagiwara et al., Phys. Rev. D 66 (2002) 010001.

[126] R.R. Akhmetshin et al. Available from hep-ex/0308008.

[127] M. Davier, S. Eidelman, A. Hocker, Z. Zhang, Phys. Lett. B. (in press); Available from hep-ph/0308213.

[128] S. Ghozzi, F. Jegerlehner, Available from hep-ph/0310181.

[129] G.W. Bennett et al., Phys. Rev. Lett. (2004) (in press).